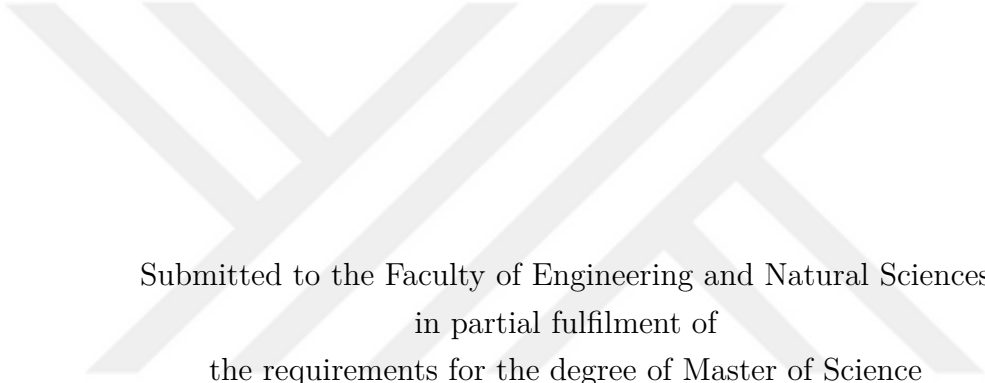


**EFFECT OF MIXED WETTABILITY SURFACES ON DROPLET
EVAPORATION AND FLOW BOILING**

by
AKAM ABOUBAKRI

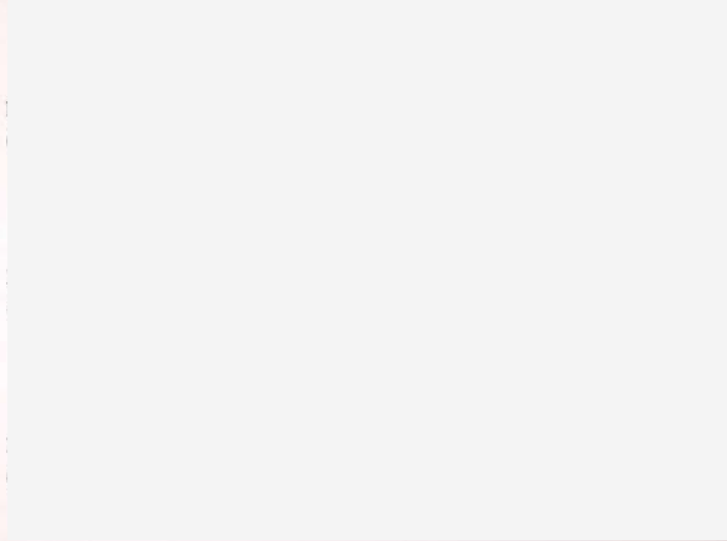


Submitted to the Faculty of Engineering and Natural Sciences
in partial fulfilment of
the requirements for the degree of Master of Science

Sabancı University
December 2021

EFFECT OF MIXED WETTABILITY SURFACES ON DROPLET
EVAPORATION AND FLOW BOILING

Approved by:



Date of Approval: December 17, 2021



AKAM ABOUBAKRI 2021 ©

All Rights Reserved

ABSTRACT

EFFECT OF MIXED WETTABILITY SURFACES ON DROPLET EVAPORATION AND FLOW BOILING

AKAM ABOUBAKRI

MECHATRONICS ENGINEERING M.Sc. THESIS, December 2021

Thesis Advisor: Prof. Dr. Ali Koşar, Dr. Abdolali Khalili Sadaghiani

Keywords: Droplet evaporation, Numerical Simulation, Adjacency Effect,
Heterogeneous Wettability, Flow boiling

Global demand on energy efficiency, along with recent concerns about greenhouse effect, has motivated researchers to conduct studies on the heat transfer performance of heat exchangers. Among the new methods proposed by the researchers, surface modifications have shown promising results in phase-change heat transfer, including flow and pool boiling, flow condensation, as well as droplet evaporation. In this thesis, the effect of surface biphilicity on flow boiling and droplet evaporation was investigated. The experimental results revealed that the biphilic surfaces are capable of enhancing the heat transfer up to 40% in droplet evaporation experiments, while up to 50% enhancement was obtained in flow boiling experiments. Moreover, using biphilic surfaces, evaporation dynamics of high aspect ratio elongated droplets was investigated. In the light of the experimental results, a fully coupled algorithm was developed which considered all the instabilities in the both liquid and gas phases. The algorithm is later used to study the effect of adjacency on evaporation dynamics of high aspect ratio water droplets.

ÖZET

KARIŞIK ISLANABİLİRLİK ÖZELLİĞİNE SAHİP YÜZEYLERİN DAMLACIK BUHARLAŞMASI VE AKIŞ KAYNAMASINA ETKİSİ

AKAM ABOUBAKRİ

MEKATRONİK MÜHENDİSLİĞİ, YÜKSEK LİSANS TEZİ, Aralık 2021

Tez Danışmanı: Prof. Dr. Prof. Ali Koşar, Dr. Abdolali Khalili Sadaghiani

Anahtar Kelimeler: Damlacık buharlaşması, Sayısal simülasyon, Bitişiklik etkisi,
Heterojen ıslanabilirlik, Akış kaynaması

Enerji verimliliğinin artması ekseninde küresel talebin artması ve sera gaz etkisi hakkında endişelerin artması, araştırmacıların ısı değiştiricilerin ısı transferi üzerinde araştırma yapmaya motive etmiştir. Araştırmacılar tarafından önerilen yeni yöntemler arasında, yüzey modifikasyonları, akış ve havuz kaynama, akış yoğunlaşması ve damlacık buharlaşması dahil olmak üzere faz değişimine dayalı ısı transferinde umut verici sonuçlar vermiştir. Tezde akış kaynama performansının artması yüzey bifilikliğinin akış kaynaması ve damlacık buharlaşması üzerindeki etki araştırılmıştır. Deneysel sonuçlar, damlacık buharlaşması deneylerinde, bifilik yüzeylerin ısı transferinde %40 oranına kadar iyileşme yapabilirken, akış kaynaması deneylerinde %50 oranına kadar iyileşme elde edildi. Ayrıca, bifilik yüzeyler kullanılarak, yüksek en-boy oranlı uzun damlacıkların buharlaşma dinamikleri araştırılmıştır. Deneysel sonuçlara ışığında, hem sıvı hem gaz fazlarındaki tüm kararsızlıkları dikkate alan Tam eşleştirme bir algoritma geliştirilmiştir. Algoritma daha sonra bitişikliğin yüksek en-boy oranlı su damlacıklarının buharlaşma dinamikleri üzerindeki etkisini incelemek için kullanılmıştır.

ACKNOWLEDGEMENTS

First and foremost, special gratitude toward my supervisor, Prof. Ali Kosar, for his interminable supports, deep knowledge, and motivations, which is impossible to be expressed in words. Undoubtedly, he is one of the most diligent persons I have ever seen. Furthermore, I would like to thank him for giving the opportunity of working in his outstanding research group.

Moreover, special thanks to Dr. Abodolali Khalili Sadaghiani, a knowledgeable, diligent, and supportive person. Indisputably, this thesis would not be preformed without his considerable recommendations.

Another special thanks to Dr. Yigit Akkus, who helped me not only with the computational part of the study, but also his great advice during my master studies. Undoubtedly, the numerical part of this study could not be performed if I did not have the privilege of his support.

Last but not least, thesis is dedicated to my dear family, who were always there for me during the hardest days of my life, especially, my beloved wife, Paria. Overcoming this academic career was impossible if I did not have the privilege of their support.



This thesis is dedicated to the science family

TABLE OF CONTENTS

LIST OF TABLES	x
LIST OF FIGURES	xi
LIST OF ABBREVIATIONS	xiv
NOMENCLATURE	xvi
1. INTRODUCTION	1
1.1. Droplet evaporation.....	2
1.2. Flow boiling.....	5
1.3. Contribution to the literature.....	7
2. EXPERIMENTAL PROCEDURE AND SAMPLE PREPARATION	8
2.1. Sample preparation	8
2.1.1. SiO ₂ and Al ₂ O ₃ samples	8
2.1.2. Si and C ₄ F ₈ samples	11
2.2. Evaporation on mixed wettability surfaces	15
2.2.1. Experimental setup	15
2.2.2. Experimental Procedure	16
2.2.3. Data reduction	17
2.3. Elongated droplet evaporation	18
2.3.1. Experimental setup	18
2.3.2. Experimental Procedure	19
2.3.3. Data reduction	20
2.4. Flow boiling.....	21
2.4.1. Experimental setup	21
2.4.2. Experimental Procedure	23
2.4.3. Data reduction	24
2.4.4. Validation of the test section.....	25

3. NUMERICAL SIMULATIONS OF DROPLET EVAPORATION	28
3.1. Governing equations	29
3.2. Boundary conditions	30
3.3. Mesh independency analysis	34
3.4. Model validation	35
4. RESULTS AND DISCUSSION	38
4.1. Droplet evaporation	38
4.1.1. Evaporation dynamics of droplets on mixed wettability samples	38
4.1.2. Evaporation dynamics of high aspect ratio elongated droplets.	42
4.1.2.1. Single cylindrical droplet	42
4.1.3. Adjacent cylindrical droplets	46
4.1.3.1. Effect of droplet diameter	46
4.1.3.2. Effect of non-dimensional pitch size and wall superheat	53
4.1.3.3. Interfacial evaporation rate	55
4.2. Flow boiling	59
4.2.1. Heat transfer results	60
4.2.2. Bubble dynamics results	63
5. CONCLUSION	66
5.1. Droplet evaporation	66
5.2. Flow boiling	68
6. FUTURE RESEARCH DIRECTION	69
BIBLIOGRAPHY	70

LIST OF TABLES

Table 2.1. Characteristics of the fabricated samples	11
Table 2.2. Characteristics of the tested samples used in flow boiling ex- periments	15
Table 2.3. Uncertainty analysis of elongated droplet evaporation	21
Table 2.4. Physical properties of FC-72 and water	23
Table 2.5. Uncertainty parameters and analysis of flow boiling tests.....	25
Table 3.1. Domain characteristics	31

LIST OF FIGURES

Figure 2.1. Sample fabrication process	9
Figure 2.2. Schematic representation of the sample with square islands ...	9
Figure 2.3. Schematic representation of the sample with rhombic islands..	10
Figure 2.4. Schematic representation of the sample with circular islands ..	10
Figure 2.5. Sample fabrication process	12
Figure 2.6. a and b) macroscopic view of the fabricated samples, c) mi- croscopic view of the samples	13
Figure 2.7. AFM pictures of the coated C_4F_8	13
Figure 2.8. a) Contact angles of hydrophobic (C_4F_8) and hydrophilic (Si) parts, b) different configuration of contact angles on biphilic surfaces..	14
Figure 2.9. Schematic representations of Sample#1 and Sample#2.....	15
Figure 2.10. Schematic of the experimental set-up	16
Figure 2.11. Schematic figure of contact angle (θ), droplet height (H), and contact radius (R)	17
Figure 2.12. Schematic representation of evaporation setup.....	19
Figure 2.13. Top and side views of the elongated droplet	20
Figure 2.14. Schematic of the closed loop setup	22
Figure 2.15. Schematic of a)test section b)thermocouple locations.....	23
Figure 2.16. Validation of the experimental setup.....	27
Figure 3.1. a) Schematic configuration of the droplets; b) Geometric de- tails of the droplets	29
Figure 3.2. Flowchart of the applied algorithm.....	34
Figure 3.3. a) Grid distribution inside and near the droplet, b) mesh in- dependency study	35
Figure 3.4. a) temperature and velocity fields, b) validation of the model: numerical results versus experimental data[107]	36
Figure 3.5. Comparison between the experimental and numerical interfa- cial temperature distributions	37
Figure 4.1. Evaporation of water droplet on SiO_2 substrate	39

Figure 4.2. Evaporation of water droplet on Al_2O_3 substrate	39
Figure 4.3. Comparison of evaporation rate on different surfaces with respect to SiO_2 sample.....	40
Figure 4.4. Evolution of TCL on mixed wettability surfaces	41
Figure 4.5. Split of water droplet on circular islands, the red lines represent the inner boundaries	41
Figure 4.6. Evaporation of group of split droplets.....	42
Figure 4.7. a) Changes in the contact angle and contact area of elongated droplets b) changes in contact angle as a function of time c) transient changes of the droplet volume	43
Figure 4.8. Velocity and temperature fields at the superheat temperatures of a) 15°C b) 50°C	44
Figure 4.9. Schematics of internal circulations at superheat temperatures of a) 15°C b) 50°C	44
Figure 4.10. Interfacial temperature distribution at the superheat temperatures of a) 15°C b) 50°C	45
Figure 4.11. Evaporative heat flux and evaporation rate as a function of substrate temperature at the superheat temperatures of a) 15°C b) 50°C	46
Figure 4.12. Evaporative heat flux and evaporation rate as a function of substrate temperature at the superheat temperatures of a) 15°C b) 50°C	48
Figure 4.13. Interfacial temperature distribution, in the presence of Marangoni effect of central and side droplets	49
Figure 4.14. Schematic representation of internal circulation and temperature distribution inside the droplets	49
Figure 4.15. The effect of droplet size at $L/D = 0.5$ and wall superheat of 50°C on temperature and velocity fields in the absence of Marangoni effect	51
Figure 4.16. The effect of droplet size at $L/D = 0.5$ and wall superheat of 50°C on interfacial temperature distribution in the absence of Marangoni effect	52
Figure 4.17. Droplet interface temperature at different non-dimensional pitch distance (L/D) and wall superheat (ΔT) for a) side droplet b) center droplet	53
Figure 4.18. Droplet velocity field at different non-dimensional pitch distance (L/D) and Rayleigh numbers (Ra).....	55
Figure 4.19. Interfacial heat flux a-b) in the presence of Marangoni flow c-d) in the absence of Marangoni flow ($L/D = 0.5$ and $T_s = 70^\circ\text{C}$)....	56

Figure 4.20. Effect of non-dimensional pitch L/D and wall superheat on the evaporation rate in the absence and presence of Marangoni flow at a) ($\Delta T = 15^\circ C$); and b) ($\Delta T = 50^\circ C$)	57
Figure 4.21. Comparison between cylindrical and spherical droplets	58
Figure 4.22. a) Velocity field in the gas phase around the SD(i) without Marangoni (ii) with Marangoni flow b) Vapor concentration field at (i). $L/D = 1$ and (ii) $L/D = 20$	59
Figure 4.23. Heat transfer coefficients (HTCs) and boiling curves corresponding to the mass flux of $90\text{kg}/\text{m}^2\text{s}$	61
Figure 4.24. Heat transfer coefficients (HTCs) and boiling curves corresponding to the mass flux of $130\text{kg}/\text{m}^2\text{s}$	62
Figure 4.25. Visualization results regarding mass flux of $90\text{kg}/\text{m}^2\text{s}$	63
Figure 4.26. Comparison of bubble dynamics on the hydrophobic surface with a biphilic surface	64
Figure 4.27. Different flow boiling patterns in a)FC-72 medium and b)water medium	65

LIST OF ABBREVIATIONS

AFM Atomic Force Microscopy	13
CCA Constant Contact Angle	2, 38, 39, 43, 69
CCR Constant Contact Radius	2, 38, 39, 69
CCW Counter Clockwise	47, 50, 53, 55
CD Central Droplet	42, 46, 47, 50, 51, 52, 53, 54, 55, 56, 57, 58, 59
CHF Critical Heat Flux	6
CW Clockwise	47, 50, 53, 55
DAQ Data Acquisition	21
DI Deionized	11, 19
HTC Heat Transfer Coefficient	1, 6, 7, 13, 22, 24, 25, 59, 62, 69
ICP Inductively Coupled Plasma	11
ICP-RIE Inductively Coupled Plasma-Reactive Ion Etching	12
LB Lattice Boltzmann	4
MD Molecular Dynamics	4
PECVD Plasma-Enhanced Chemical Vapor Deposition	9
PR Photoresist	9, 12
RCA Standard of Radio Corporation of America	8
RF Radio Frequency	11
RIE Reactive-Ion Etching	11
SD Side Droplet	42, 46, 47, 50, 51, 52, 53, 54, 55, 56, 57, 58, 59

TCL Triple Contact Line 39, 40, 41, 66, 69
UV Ultraviolet 12



NOMENCLATURE

Latin Symbols

\dot{m}''	Evaporative mass flux (kg/m ² .s)
c_p	Specific heat capacity (J/kg.K)
q''	Heat flux (W/m ²)
Δt_{eva}	Total time required time for evaporation (s)
\dot{m}	Evaporation rate - Mass flow rate (kg/s)
\dot{m}^*	Relative evaporation rate (-)
\dot{Q}	Heat (W)
\vec{n}	Normal vector (-)
\vec{t}	Tangential vector (-)
\vec{u}	Velocity vector (m/s)
A	Area (mm ²)
AR	Aspect ratio of elongated droplets (-)
Bo	Bond number (-)
C	Molar concentration (mol/m ³)
D	Contact diameter of the droplet (mm)
D_H	Hydraulic Diameter (mm)
D_{w-air}	Diffusion constant of water vapor in the air (cm ² /s)
g	Gravitational acceleration (m/s ²)
H	Height of droplet (mm)

h	Convective heat transfer coefficient (W/m ² .K)
H_{∞}	Height of simulated domain (mm)
h_{fg}	Latent heat of vaporization (J/kg)
L	Length/Distance (mm)
l	Length of elongation of the droplet (mm)
Nu	Nusselt number (-)
p	Pressure (Pa)
Pr	Prandtl number (-)
R	Contact radius of droplet (mm)
R_p	Thermal resistance of the paste (m ² .K/W)
Re	Reynolds number (-)
t	Time (s)
T	Temperature (°C)
V	Volume (m ³)
W_{∞}	Width of simulated domain (mm)

Greek Symbols

α	Thermal diffusivity (m ² /s)
δ	Thickness (mm)
γ	Polar angle of droplets (°)
κ	Thermal conductivity (W/m.K)
μ	Dynamic viscosity (Pa.s)
Φ	Viscose dissipation term (K/s)
ϕ	Relative humidity (-)
ρ	Density (kg/cm ³)
σ	Surface tension (N/m)
θ	Contact angle of the droplet (°)

Subscription

0	Initial value
∞	Ambient condition
<i>air</i>	air
<i>av</i>	Average
<i>c</i>	Cross section
<i>ch</i>	Channel
<i>con</i>	Conduction/Conductive
<i>eva</i>	Evaporation/Evaporative
<i>f</i>	Fluid
<i>g</i>	Gas
<i>i</i>	Counter
<i>in</i>	Value at inlet
<i>j</i>	Counter
<i>l</i>	Liquid
<i>loss</i>	Loss value
<i>net</i>	Net value
<i>out</i>	Value at outlet
<i>Rad</i>	Radiation/Radiative
<i>s</i>	Surface/Substrate
<i>sat</i>	Saturation
<i>v</i>	Vapor
<i>w</i>	Wall

1. INTRODUCTION

Efficiency of the heat exchangers plays an important role in the energy required in industrial applications. The energy cost along with the recent concerns about global warming has become a great motivation for the researchers to conduct studies on performance of heat exchangers. Recent studies propose that use of nano-fluids [1], vortex generators [2], magnetic fluids [3], as well as pipe alignment [4] could provide potential enhancement in heat transfer. As an example, Karimzadehkhoei et al. [5] showed that the nano-particles could enhance the average HTC (Heat Transfer Coefficient) up to 25%. In another study, Carpio and Valencia [6] numerically investigated the effect of vortex generators on heat transfer of compact heat exchangers. They reported that the vortex generators offered a potential of enhancement in HTC up to 52%. Regarding the magnetic fluids, Bezaatpour and Goharkhah [7] proved that magnetic fluids were capable of enhancing heat transfer by around 320%.

During the recent years, phase change has attracted an considerable attention in many applications, such as desalination [8], metallurgy [9], food processing [10], phase change driven pumps [11], and biological sensors [12], to name a few. Moreover, due to the considerable amount of latent heat of phase change, it has a wide range of applications in the fields of thermal management and electronic cooling [13], where the working fluid may be either water [14] or other industrial refrigerants such as R-134a [15], isobutane [16], and FC-72 [17], among others. These fluids may be selected based on the working conditions and amount of heat which should transferred. In industrial applications, depending the time and length scale, and the working conditions, phase change occurs in a quasi-steady state[18].

Surface modification techniques such as coatings [13], porous and micro/nano structured surfaces [19–21], thin film polymeric coatings [22, 23] have already shown enhancing effects on phase change heat and mass transfer by altering contact line dynamics, as well as the number of active nucleation sites [24]. For instance, Sadaghiani et al. [23, 25] investigated the effect of artificial cavities on solid/liquid/gas three-phase contact line and found that there existed an optimum diameter to pitch distance ratio, which maximized boiling heat transfer in pool boiling. Recently,

innovative designs of the biphilic surfaces have shown that biphilic surfaces could enhance heat transfer in flow boiling [13], pool boiling [26], flow condensation [27], and droplet evaporation [28].

In this study, two different types of mixed wettability surfaces were designed and fabricated in order to investigate the effect of biphilicity of the surfaces on droplet evaporation and flow boiling. First, surfaces fabricated from combination of SiO_2 and Al_2O_3 , which represent the hydrophilic and hydrophobic regions, respectively. These surfaces were utilized study the effect of mixed wettability on spherical droplets. Later on, an innovative method was implemented to fabricate surfaces made of Si and C_4F_8 , where they showed the hydrophilic and hydrophobic properties, respectively. These surfaces were used not only to study the effect of elongation on evaporation dynamics, but also in an experimental study for heat transfer enhancement in closed loop FC-72 flow boiling.

1.1 Droplet evaporation

Droplet evaporation is one of the most observed phenomena in nature and plays important roles in a wide range of applications such as electronic cooling [29–31], 3D printing [32–34], DNA sorting [35, 36], and surface patterning [37]. Many studies in the literature have analyzed the dynamics of single droplet evaporation both experimentally [38, 39] and numerically [40, 41]. For instance, in an early study, Picknett and Bexonf. [42] reported that every droplet exhibited three different types of behavior during evaporation. On real rough surfaces, the droplet evaporates while maintaining a pinned contact radius and a decreasing contact angle. This state of evaporation is referred to the CCR (Constant Contact Radius) mode. On ideally smooth surfaces, evaporation proceeds with the contact angle remaining practically constant and a decreasing in the contact radius. This is known as the CCA (Constant Contact Angle) mode. During the evaporation of droplets on real surfaces, usually, CCR mode is first observed then followed by CCR mode, and finally, during the last stage of evaporation, both contact angle and contact radius decrease simultaneously, which is known as the mixed mode. Most of the further studies [43–46] confirmed these stages and offered more insight into the dynamics of droplets during evaporation. On the other hand, some studies have introduced some mechanisms, such as the formation of bubbles due to depressurization on the contact surface [47], which hinders the contact line to shrink.

The dynamics of the triple contact line significantly affects evaporation since the evaporation rate is largest at the contact line [48, 49], which is of great importance in heat transfer applications [50], as well as colloidal residue deposition [51, 52]. For instance, an increase in the length of the triple contact line of a specific volume of droplet raises the evaporation rate. Shan et al. [53] reported that triangular and square-shaped triple contact lines resulted in an increase of evaporation rate by 14% and 8% in comparison to a circular shaped contact line, which corresponded to enhancements in heat transfer by 21% and 15%, respectively [54]. In another study, it was reported that the triangular contact line could enhance the evaporation rate by 46% and 71% relative to square and circular contact line shapes, respectively [55].

The surface modification also changes the wetting dynamics of the droplet [56], which unavoidably results in changes in the evaporation dynamics of the droplet. Dia et al. [57] showed that nano-porous coating enhanced the ability of wetting, heat and mass transfer in single droplet evaporation. Jansen et al. [28] reported that due to the tendency of elongation in droplets the striped patterned surfaces improved the evaporation rate. Recently, Khilifi et al. [58] studied evaporation of micro-droplets in the Wenzel-like regime on textured surfaces, which revealed that the evaporation rate could be enhanced by more than nine times in comparison with a smooth surface.

Ambient conditions, including temperature, pressure, relative humidity, and convection around the droplet, are the other important parameters, which affect the evaporation dynamics. Ye et al. [59] studied sessile droplet evaporation at sub-atmospheric conditions for water and ethanol droplets and reported that the ambient pressure not only changed the interface temperature distribution but also affected the internal circulation as well. Buffone [60] investigated the effect of forced convection on evaporating droplets and found that the evaporation rate strongly deviated from the previous models, due to asymmetric conditions around the droplet.

Even though the combined effect of multiple droplets should be considered in most of the application areas such as cooling, the majority of studies have focused on evaporation dynamics of a single droplet to simplify the complex nature of evaporation such as droplet breakup [61] and droplet coalescence [62]. Another parameter significantly affecting the combined effects is droplets adjacency. The number of relevant studies in the literature is rather limited. Pardhan and Panigrahi [63] numerically analyzed the dissolution of binary droplets, for both single and adjacent droplets at room temperature. They reported that the neighboring droplets influenced the evaporative heat flux of each other, and as the distance of the droplets increased, the droplets tended to show the behavior of a single droplet. Wary et

al. [64] numerically investigated the effect of natural convection in the gas phase on the evaporation rate of an array of droplets. The evaporation rate of the outermost droplet was relatively larger than the inner one. Similar trends were observed by Chong et al. [65] for an array of droplets. They concluded that the outermost droplet could exhibit an evaporation rate even larger than a single isolated droplet at higher droplet Rayleigh numbers [66].

The interactions among solid, liquid, and gas phases significantly influence heat and mass transfer in evaporation. Recently, using both MD (Molecular Dynamics) [67, 68] and LB (Lattice Boltzmann) [69, 70] simulation methods, the effects of these three phases were coupled, and the Leiden-frost effect was studied. However, these two methods have their drawbacks as well. First, MD simulation requires simulation of the droplet with smaller dimensions, while LB simulation dismisses the effect of the internal flow of evaporating droplets. Similarly, some of the previous studies on adjacent droplets only considered the effect of natural convection in the gas phase and neglected the effect of the liquid domain [64, 65, 71], while the rest of the literature examined the liquid phase domain and did not take natural convection into account, where evaporation rate was considered as only diffusion driven [63]. For single droplet evaporation, Akkus et al. [72] demonstrated that neglecting natural convection underestimated evaporation by more than 50% at high substrate temperatures, whereas excluding Marangoni convection in the liquid phase led to a 40% underestimation of evaporation rate. The liquid and gas domains are inter-related, this implies that neglecting one of the physics at either domain results in considerable deviations from empirical observations.

The literature lacks studies investigating the evaporation dynamics on mixed wettability surfaces, as well as high aspect ratio elongated droplets and adjacency effect on the evaporation performance lacks in different aspects including droplet shape, mutual coupling between gas and droplet domains, detailed temperature and velocity field analyses in the two-phase domain, and as well as in parametric analysis. Therefore, modifications in the droplet geometry and analysis approaches were important for further understanding droplet evaporation and its application. To fill these gaps, this thesis aims to investigate the effect biphilicity of surfaces on evaporation dynamics of both spherical and high aspect ratio elongated droplets. The spherical droplets are studied on surfaces fabricated from SiO_2 and Al_2O_3 . These surfaces possessed hydrophilic islands, surrounded by less hydrophilic area. The islands were circular, square, and rhombic shaped. The sizes of the islands were one, one-fourth, and one-sixteenth times of the droplet radius on the pure hydrophilic surface, for each shape. It is worth mentioning that the obtained optimum ratio of hydrophobic to the total area of the surface provided by Motezakker et al. was used

as reference, to the surface designs.

Furthermore, surfaces from combination of Si and C₄F₈ were used to study the effect elongation on evaporation dynamics of water droplets. The tested substrate had a hydrophilic stripe on which the water droplets were placed to become elongated. The hydrophilic stripe was surrounded by hydrophobic area. Later on, based on the experimental results, a numerical model was developed and validated to study the effect of droplet adjacency on hydrothermal properties of evaporating droplets. Using a non-dimensional droplet pitch distance (L/D), the velocity field inside the adjacent droplets and distributed heat flux at the interface of the adjacent cylindrical droplet were investigated. Moreover, the effect of droplet vicinity on the vapor field was revealed and discussed in detail.

1.2 Flow boiling

Flow boiling is one of the most effective heat transfer methods, especially in micro-scale and could provide a better performance relative to pool boiling as well as single phase flows [73]. Amongst working fluids, the dielectric coolant FC-72 was proposed as a candidate in flow boiling [74]. The working coolant FC-72 is a colorless, odorless and non-flammable fluid with thermal and chemical stability. It also has a low toxicity and good compatibility with metals and plastics [75]. Mudawar et al. [76] conducted subcooled flow boiling experiments with FC-72. They observed that the boiling phenomenon delayed with the flow velocity. Hiendel et al. [77, 78] conducted flow boiling experiments on FC-72 and revealed that heat transfer was enhanced with the fluid velocity for partially developed boiling. However, for fully developed boiling, the effect of velocity was not significant. According to another study with FC-72, the increase in the fluid velocity and subcooling temperature led to reduced temperature excursion and boiling hysteresis [79]. Martin-Callizo et al. [80] concluded that even though the heat transfer coefficient generally increased with the heat flux, there was not any dependency for vapor qualities lower than 50%.

Experimental studies proved that hydrophobic substrates provide higher heat transfer coefficients in flow boiling in micro- [81, 82] and minichannels [83, 84] in comparison with hydrophilic ones. Generally, low energy surfaces (hydrophobic) remarkably augment the onset of nucleate boiling and bubble departure, while high

energy surfaces (hydrophilic) enhance liquid replenishment and raises the critical heat flux [23, 26, 85]. Therefore, mixed wettability surfaces, which could be also achieved with surface modification, could enhance HTC. As an example, Wang et al. [86] investigated the effect of mixed wettability on flow boiling of water and reported that mixed wettability surfaces not only increase the nucleation site density but also ease the bubble departure. In the study of Kim et al. [87] on the effect mixed wettability surfaces in flow boiling of water, it was shown that hydrophobic stripes, regardless of their direction with respect to the flow direction, provided active nucleation sites. They also concluded that merging and confinement of the bubbles are the major mechanisms enhancing boiling heat transfer. In another study, Kim et al. [88] proved that compared to dotted patterns, parallel patterns possessed a better heat transfer performance at low water mass fluxes, while the dotted surfaces outperformed the parallel patterns at high mass fluxes. Moreover, it was reported that biphilic surfaces resulted in enhancements of pool boiling [26] and flow boiling heat transfer [13]. According to Honda and Wei [89], micro structures such as micro-roughness and micro-porous coatings significantly facilitated the incipience of boiling, while delaying the CHF (Critical Heat Flux). In another study, Honda et al [90] conducted pool boiling experiments with FC-72 on silicon substrates modified by micro-pin-fins and obtained noticeable enhancements in the nucleate boiling regime and critical heat flux.

Bubble dynamics study under reduced gravity in flow boiling experiments with FC-72 conducted by Ma and Chung [75] revealed that the departure time and size decreased with the flow rate. In another study, Yin et al. [91] performed flow boiling tests with R134a and demonstrated that the departure size and frequency decreased with liquid subcooling. Maurus et al. [92] concluded that bubble nucleation increased and decreased with the heat flux and mass flux, respectively. Also, the same trend existed for bubble growth rate.

So far, even though pool boiling heat transfer on purposefully modified surfaces has been investigated by many researchers, flow boiling on biphilic surfaces needs further studies. In this regard, this thesis offers the first study, which focuses on biphilic surfaces fabricated with a new method, on flow boiling of FC-72. Although this fluid has wide industrial applications, the information regarding flow boiling is relatively insufficient. The applied polymer, C_4F_8 , possesses hydrophobic properties, and its islands constitute the hydrophobic part of the surface, while Si is used as the hydrophilic regions of the surface. Each of the islands were circular shaped. It should be noted that the substrates possessed three different regions. The ratio of hydrophobic to total area of the surface reduced from the inlet to outlet. The heat transfer performance were investigated for different biphilic surfaces in the following

sections, in the light of flow boiling visualization. It should be noted that since compared to hydrophilic surfaces the hydrophobic surfaces typically provide higher HTC's [81–83], the HTC's obtained from the biphilic surfaces are compared with a hydrophobic surface, which acted as a better reference for comparison purposes.

1.3 Contribution to the literature

As it is mentioned before, this thesis has investigated the effect of mixed-wettability surfaces on droplet evaporation and flow boiling. This thesis firstly is concerned with the effect of mixed-wettability surfaces on dynamics of spherical droplet evaporation. For the first time, the effect of the size and the shape of mixed wettability islands on droplet evaporation is investigated. Later, the effect of mixed-wettability surfaces on the effect of elongation of droplets, and dynamics of high aspect ratio droplet evaporation is investigated. This study, for the first time, studies the evaporation dynamics of high aspect ratio droplets. Moreover, a 2D numerical simulation is also performed on cylindrical droplet evaporation. After a mesh independency analysis, the numerical simulation is validated against experimental studies. This numerical simulation is used to study the effect of adjacency on droplet evaporation. This numerical simulation is the first study on adjacent droplets which considers all the instabilities in the droplets. Finally, the effect of biphilicity of the surfaces on FC-72 flow boiling in a mini-channel is investigated.

In this thesis, first, the experimental procedures and sample preparation are discussed (2). Later on, a chapter covers the numerical analysis of the droplet evaporation, which is validated with the experimental results (3). Afterwards, the obtained results are discussed in detail (4), and a chapter is devoted to conclusions (6).

2. EXPERIMENTAL PROCEDURE AND SAMPLE PREPARATION

This chapter contains four different sections. In the first section (2.1), the sample fabrication processes of the both $\text{SiO}_2/\text{Al}_2\text{O}_3$ and $\text{Si}/\text{C}_4\text{F}_8$ samples are illustrated. Then, three experimental procedures are included the experiments of spherical droplet evaporation (2.2), elongated droplet evaporation (2.3), and flow boiling (2.4), respectively. Each of these sections includes with experimental setup, experimental process, and data reduction.

2.1 Sample preparation

In this section, the fabrication process of the $\text{SiO}_2/\text{Al}_2\text{O}_3$ samples is first presented. Later on, the size and characteristics of each of the tested samples are discussed. These samples were used in spherical droplet evaporation on mixed wettability samples. In continuation, the process flow of $\text{Si}/\text{C}_4\text{F}_8$ samples is presented. Moreover, the properties of each samples are presented in details. It is worth mentioning that these samples were used in two different studies: evaporation dynamics of elongated droplets and closed loop flow boiling of FC-72.

2.1.1 SiO_2 and Al_2O_3 samples

Figure 2.1a represents silicon wafers. First, these wafers were cleaned in three consecutive steps: 1. removal of the organic contaminants, 2. removal of thin oxide layer, and 3. removal of ionic contamination. These three steps are known as RCA (Standard of Radio Corporation of America) cleaning. After the RCA cleaning,

50nm oxide layer (for hydrophobicity) was deposited via PECVD (Plasma-Enhanced Chemical Vapor Deposition) system on 1cm×1.5cm silicon substrates, as seen in Figure 2.1b. A layer of AZ 4562 PR (Photoresist) was coated on the wafer (See Figure 2.1c). As depicted in Figure 2.1d, electron beam lithography was performed to define the hydrophilic region, and later the samples were placed into developers. The schematic of the obtained sample is shown 2.1e. In order to improve the lift-off quality, a short time (10 seconds) O₂ plasma was processed to remove any remaining resist residues after development. 100nm thick Al₂O₃ deposition by e-beam evaporation was evaporated, and the substrates were left for an over-night acetone lift-off. After the lift-off process, substrates were immersed in acetone and isopropanol, respectively, and dried with N₂ gas. The final obtained sample is shown in Figure 2.1g.

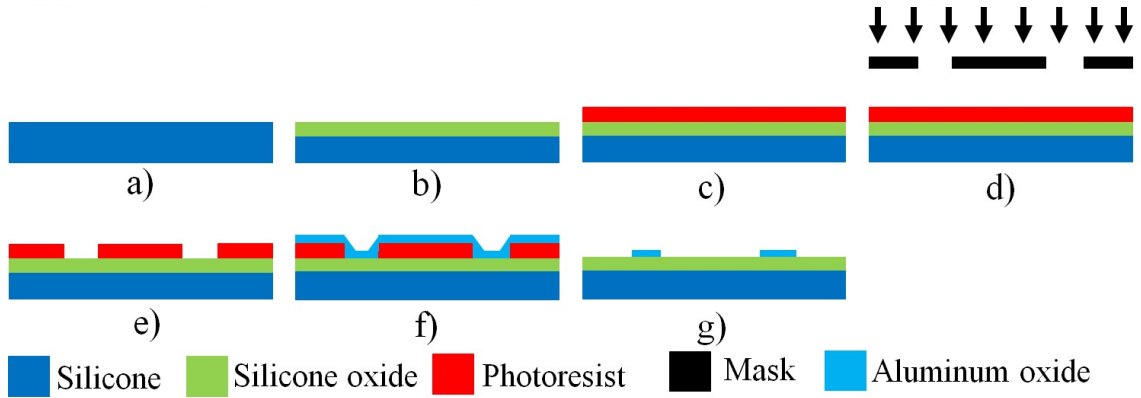


Figure 2.1 Sample fabrication process

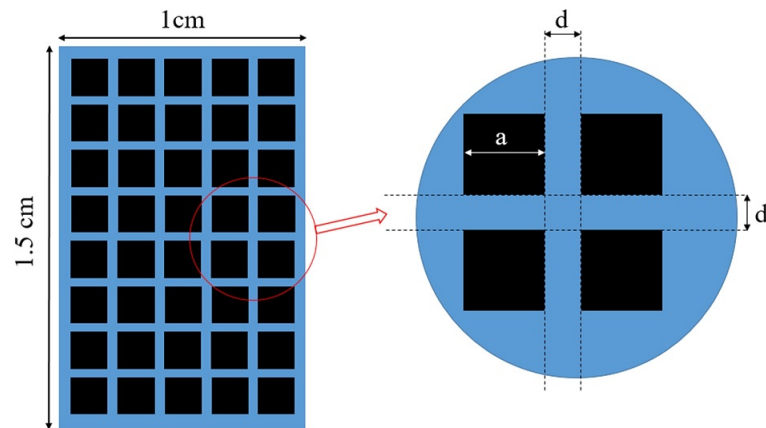


Figure 2.2 Schematic representation of the sample with square islands

Figure 2.2 shows the schematic sizes and shapes of the samples of square islands. The experiments were done on three different samples with square-shaped islands. The length of the largest square spots was 2400 μ m, and the distance between them was

600 μm . For the middle-sized squared-shaped islands, the length of the squares was 1200 μm , which were 300 μm far from the neighbor spots. In the third sample, which was composed of small size hydrophilic spots, the length and distance between the square spots were 600 μm and 150 μm , respectively. These three spot sizes represent the one times, one-fourth times, and one-sixteenth times of the water droplet on SiO_2 sample, respectively. The black islands represent the SiO_2 spots, and the blue parts on the sample represent the Al_2O_3 coated parts of the samples.

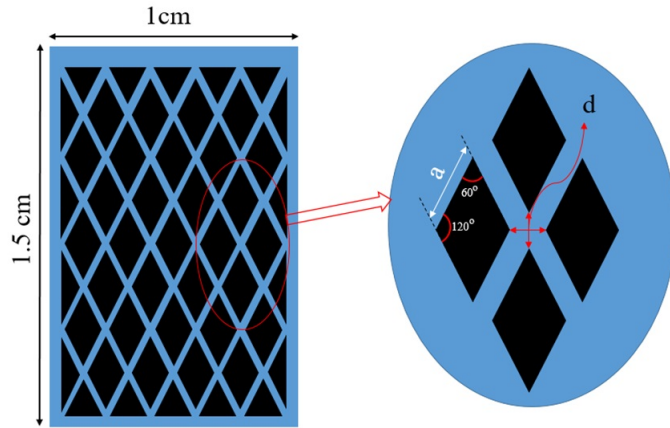


Figure 2.3 Schematic representation of the sample with rhombic islands

Figure 2.3 shows the shape of the rhombic islands on the samples. The sample with the largest island size had the islands with the edge size of 2600 μm , while they were 600 μm far apart. The middle-sized sample possessed islands with the edge size of 1300 μm and the distance between the islands was 300 μm . On the smallest sample with rhombic islands, the size of the islands was 650 μm with a 150 μm clearance in between.

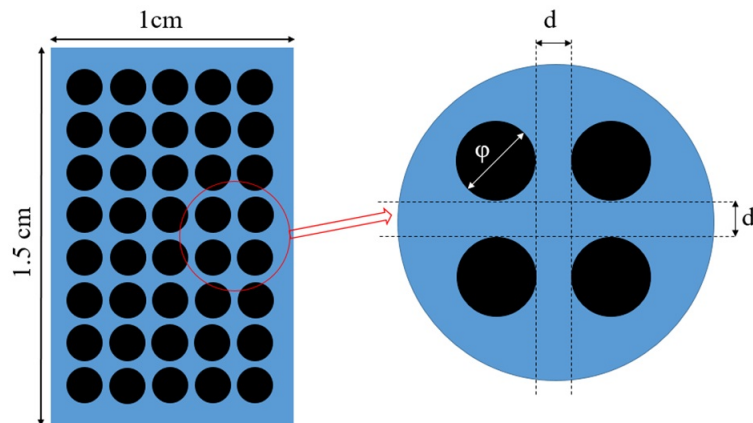


Figure 2.4 Schematic representation of the sample with circular islands

Figure 2.4 represents the configuration samples with circular islands, made of SiO_2 ,

surrounded by Al_2O_3 area. The experiments were conducted on two distinct samples. For the first case, the diameter of the circular islands was $1400\mu\text{m}$ and the minimum distance between islands was $100\mu\text{m}$. The islands on the second circular-shaped sample had the diameter and the minimum distance of $700\mu\text{m}$ and $50\mu\text{m}$, respectively. The sample with spot diameter of $1400\mu\text{m}$ represents the sample with the island size of one-fourth times of the water droplet diameter, while the sample with islands with diameter of $700\mu\text{m}$ represents the sample, on which the island size is one-sixteenth times of the water droplet on bare SiO_2 sample. Also, it is worthwhile to state that the droplet on the bare SiO_2 sample was considered to be on a large size island, with a circular contact line. Table 2.1 summarizes the characteristics of the tested samples.

Table 2.1 Characteristics of the fabricated samples

	Square islands		Rhombic islands		Circular islands	
	Size of island (μm)	Distance (μm)	Size of island (μm)	Distance (μm)	Size of island (μm)	Distance (μm)
Large-sized islands	2400	600	2600	600	-	-
Middle-sized islands	1200	300	1300	300	1400	100
Small-sized islands	600	150	650	150	700	50

2.1.2 Si and C_4F_8 samples

Plasma Polymerization has attracted much attention during the recent years, particularly due to changes in sample wettability [93–95], which can be performed at both subatmospheric and atmospheric [96] pressures. Plasma Polymerization offers methods to change the sample geometric and chemistry structures for manipulating the wettability of samples [97]. This ability has motivated many researchers in the field of two-phase heat transfer [98–100]. Similarly, as mentioned before, C_4F_8 polymer was used in the fabrication of biphilic samples.

In this innovative fabrication method, different steps were carried out. Firstly, the silicon wafers were washed with Acetone, Isopropanol and DI (Deionized) water, and then N_2 gas was blown on the substrate to get rid of any contaminations. Next, in plasma environment (Oxford PlasmaLab System 100 ICP 300 Deep RIE), the wafers were deposited with C_4F_8 polymer (Figure 2.5a). During this process, the pressure, RF power, ICP power, and deposition temperature were 30mTorr , 5Watt ,

1500Watt, and 5°C, respectively. Also, the plasma polymerization occurred under the continuous wave. It should be noted that this machine was usually used for etching of semiconductors, including both etching and deposition steps. However, the etching process was deactivated over this fabrication method. After having the fully polymer-coated substrates, a layer of AZ 4562 (PR) was coated on the silicon substrates at 4000rpm for 45 seconds and was baked for 1 minute at 110°C. Even though coating of PR on hydrophobic samples seems to be challenging, the process did not face any failure. However, a layer of SiO₂ could be used as a sacrificial layer for PR coating [101]. The next step was the UV (Ultraviolet) light exposure (115mJ/cm²) using a mask aligner UV-Lithography (Midas aligner) (Figure 2.5b). Next, by taking advantage of the designed acetate masks, the wafers were patterned using the photolithography fabrication method (Figure 2.5c). Afterwards, the AZ 726 MIF developer was used to develop the substrates for 40 seconds before putting them on the hot plate. In this step the patterning process was finished, and the areas to be hydrophobic were covered with PR, which was resistant against etching (Figure 2.5d). The silicon wafers were put in the Oxford ICP-RIE machine again to etch the polymer until reaching to the silicon areas (Figure 2.5e). Finally, the substrate shown in Figure 2.5f is obtained.

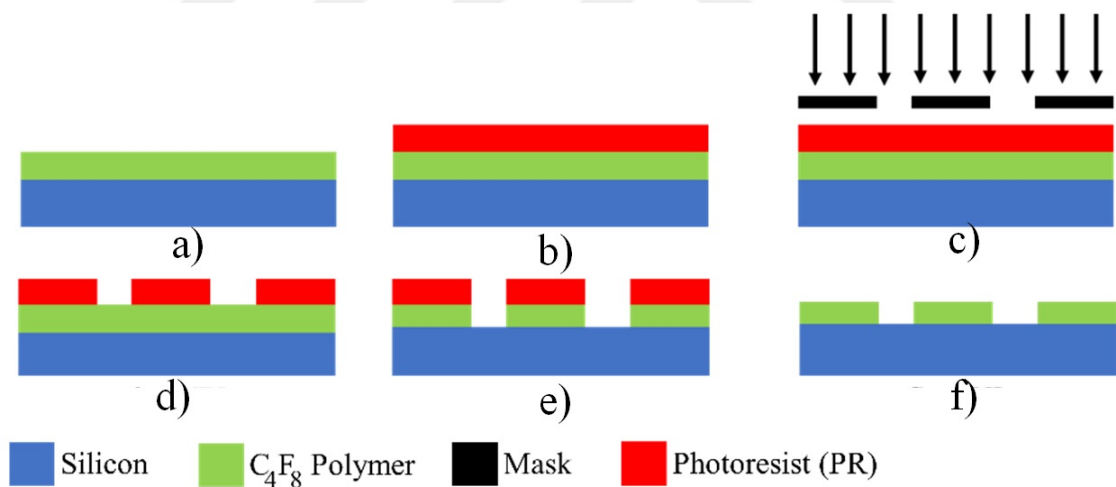


Figure 2.5 Sample fabrication process

Figure 2.6a and 2.6b show the macroscopic view of the samples, fabricated for flow boiling and elongated droplet evaporation, respectively. The bright areas of the wafer are the Si, while the darker regions are C₄F₈ polymer areas. Moreover, in order to determine the quality of the coated polymer, a microscopic analysis of the wafer is attached. As seen in Figure 2.6c, the tolerance of hydrophobic spots is smaller than 2µm.

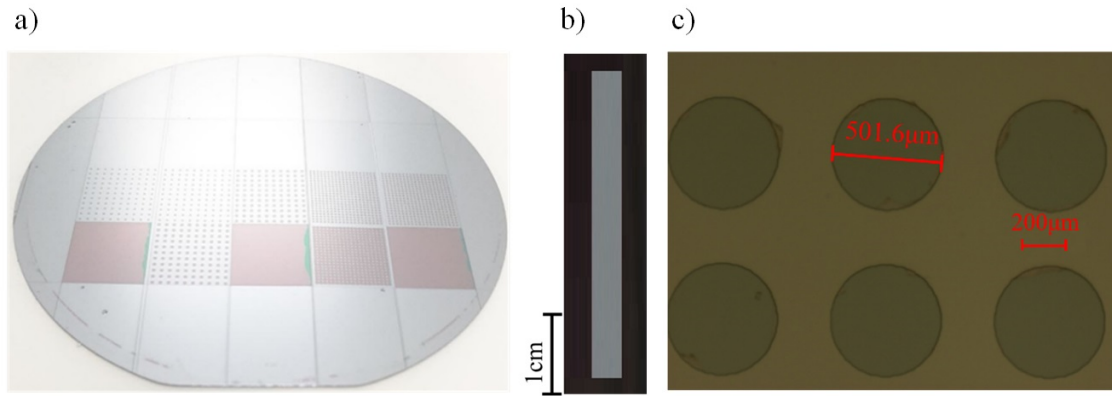


Figure 2.6 a and b) macroscopic view of the fabricated samples, c) microscopic view of the samples

In this thesis, the aim is provide nucleation sites due to wettability difference on polymer islands. Many studies in the literature suggest that the roughness of a substrate may provide significant amount of nucleation sites. Therefore, the roughness of a substrates has a potential of affecting the obtained HTC's in flow boiling experiments [19, 102]. To ensure that any possible enhancement in heat transfer does not stem from the roughness of the coated polymer, the roughness of the surfaces was measured using 2D and 3D AFM in dynamic mode (ezAFM, Nanomagnetics Instruments). The AFM images are provided in Figure 2.7. According to the obtained results, the average roughness of the surfaces was 0.87nm, while the root mean square was obtained as 1.11nm. As the AFM results suggest, the roughness of the samples is relatively small, and does not have any considerable effect on heat transfer.

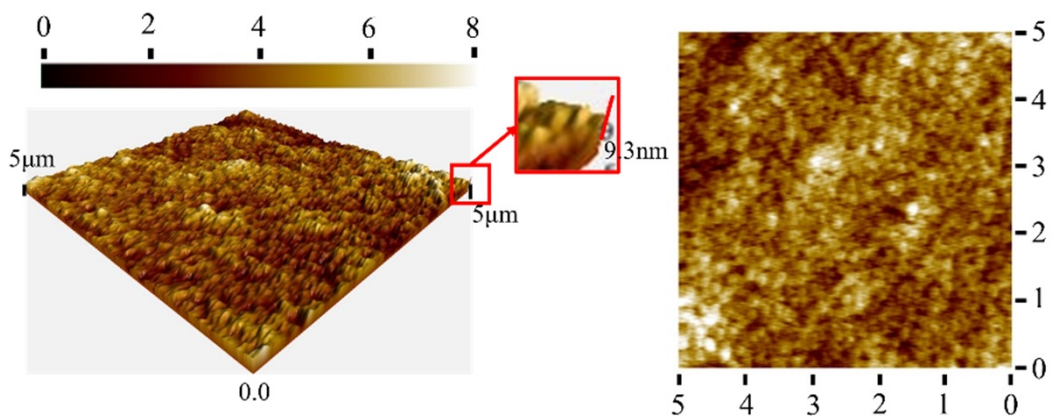


Figure 2.7 AFM pictures of the coated C_4F_8

It is noteworthy to mention that the contact angles of a 5µl water droplet on the silicon and the C_4F_8 islands were 55° and 110° , respectively, as depicted in Figure 2.8a. It should be noted that the biphilic surfaces do not necessarily change the

contact angle of the droplet but the hydrophobic spots provide potential nucleation sites. As a droplet is placed on a tested surface, different scenarios may occur. In order to have a better understanding about the shape of contact angles, a simulation in Surface **Evolver 1.30** is conducted. The results are presented in Figure 2.8c. As a droplet is placed on a totally hydrophobic or totally hydrophilic surface, the contact angles agree with the measured contact angles (Figures 2.8b-i and 2.8b-ii, respectively). However, as a droplet is placed on the biphilic regions, the shape of the triple contact line depends on the size of the droplet. A large droplet (25 μ L in Figure 2.8b-iii) can exceed the hydrophobic areas, which results in a contact angle similar to a totally hydrophilic surface. Similarly, a small droplet, which can fit inside the hydrophobic spots (5 μ L in Figure 2.8b-iv), has the same contact angle as with a totally hydrophilic sample. However, the contact lines of a droplet with a medium size (15 μ L in Figure 2.8b-v) include both hydrophilic and hydrophobic regions. In this situation, the contact line on hydrophobic areas is repulsed towards the center of the droplet.

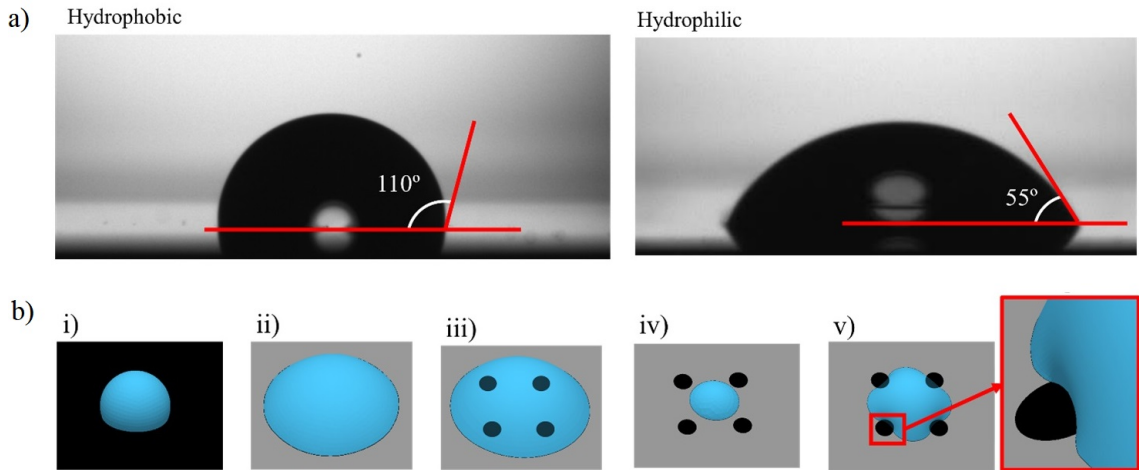


Figure 2.8 a) Contact angles of hydrophobic (C_4F_8) and hydrophilic (Si) parts, b) different configuration of contact angles on biphilic surfaces

Furthermore, Figure 2.9 shows the schematics of the tested samples. As shown in Figure 2.9, the biphilic samples are divided into three regions. The fully hydrophobic sample is totally coated with C_4F_8 . Sample#1 has a hydrophobic entrance, while the middle region possesses hydrophobic islands on hydrophilic area. Sample#2 has biphilic properties in the both entrance and middle regions. Moreover, both of biphilic samples have fully hydrophilic properties at the outlet. Table 2.2 summarizes the characteristics of the biphilic substrates.

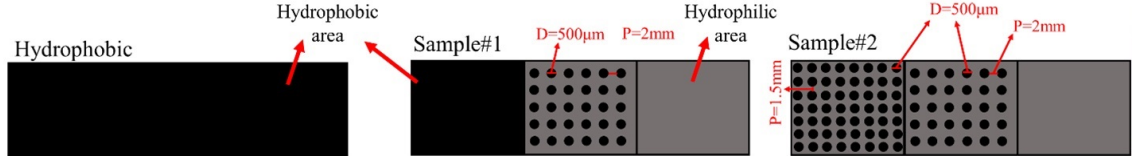


Figure 2.9 Schematic representations of Sample#1 and Sample#2

Table 2.2 Characteristics of the tested samples used in flow boiling experiments

	Region I	Region II	Region III
Sample#1	Hydrophobic	Biphilic – D=500 µm P= 2000µm	Hydrophilic
Sample#2	Biphilic – D=500 µm P= 1500µm	Biphilic – D=500 µm P= 2000 µm	Hydrophilic

2.2 Evaporation on mixed wettability surfaces

An experimental study is conducted to investigate the effect of mixed wettability surfaces on evaporation dynamics of water droplets. Ten different test specimens were fabricated as discussed previously (See 2.1.1), with different shapes and the sizes of the islands. The evaporation rates of the droplets are compared with the both SiO_2 and Al_2O_3 samples.

2.2.1 Experimental setup

Figure 2.10 shows schematic representation of the experimental setup. Two cameras, which provide top and front views of the evaporating droplets, were used in order to record the change in the contact angle and contact radius of the evaporating water droplets. The videos were recorded in a workstation for further analysis. A power supply was connected to the four cartridge heaters, with diameter of 8mm and length 5cm. In order to measure the surface temperature, three thermocouple locations were designed in the setup, which were connected to previously calibrated thermometers. Moreover, to reduce the influence of airflow from outside, the whole setup was secured by a housing.

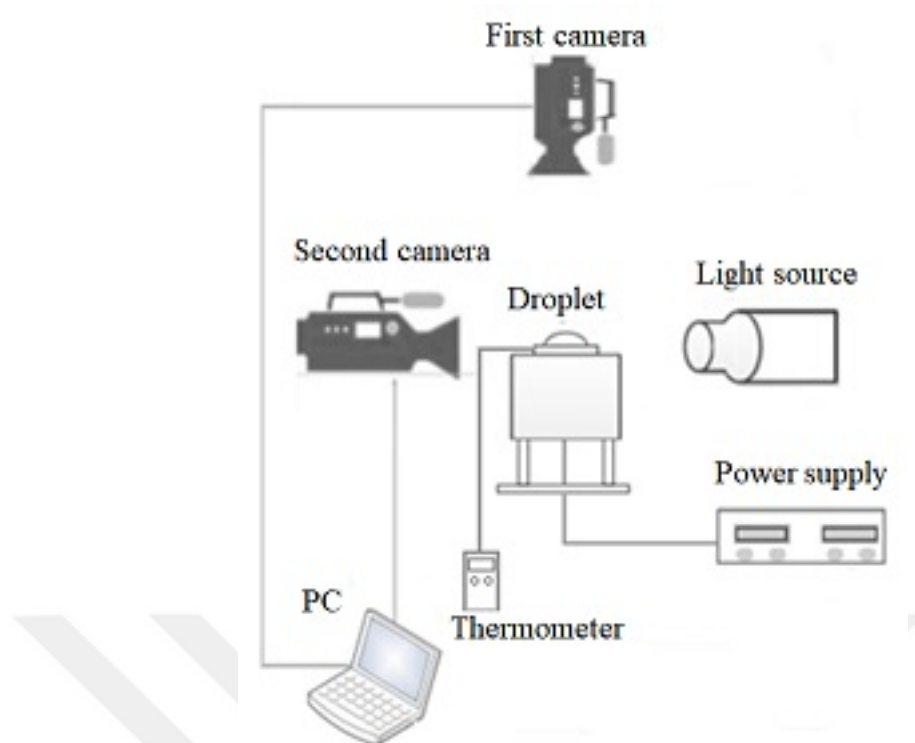


Figure 2.10 Schematic of the experimental set-up

2.2.2 Experimental Procedure

Using a standard micro-syringe, a $5\mu\text{L}$ of water droplet was placed on the test specimens. The temperature and relative humidity of the environment were maintained at $23\pm 1^\circ\text{C}$ and $60\pm 5\%$, respectively. During the evaporation, the videos of the evaporating droplets were recorded. From the recorded videos of the evaporating water droplet on all samples, the contact angle (θ), droplet height (H), and contact radius (R) were obtained using image processing techniques. Figure 2.11 shows the schematic characteristics of evaporating water droplet. Constant heat flux of ($500\pm 2\% \text{ W/m}^2$) was supplied by a power supplier. First, the setup was turned on, and we waited to reach to a steady-state. The experiments have been done under a steady-state of sample temperature ($38\pm 1^\circ\text{C}$). Since the thermal conductivities of the substrates were sufficiently high, the substrate temperature was almost constant during the experiments. Moreover, the equilibrium contact angle of the water droplet is 30° and 65° for SiO_2 and Al_2O_3 samples, respectively.

It should be noted that in order to make sure the results are repeatable, each of the experiments was repeated at least three times. Before each experiment, the surfaces were cleaned in three consecutive steps: ultrasonic baths of acetone and isopropanol,

and after these two steps, they got cleaned by distilled water. Subsequently, N₂ gas was used to dry the surfaces more rapidly.

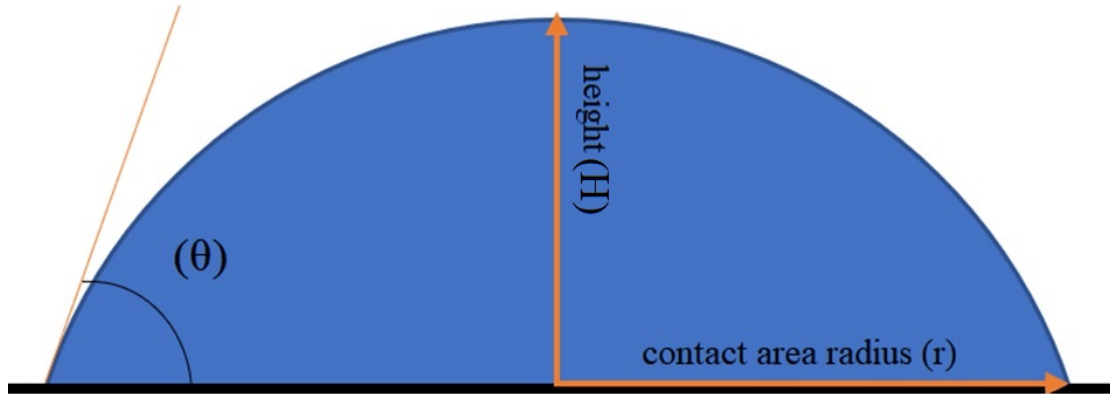


Figure 2.11 Schematic figure of contact angle (θ), droplet height (H), and contact radius (R)

2.2.3 Data reduction

As mentioned before, the changes in the contact angle (θ), height (H), and contact radius (R) were measured during the experiments. Since the contact angle on mixed wettability locally changes, calculation of instant evaporation rates requires advanced methods. However, to ease the process, the average evaporation rates are calculated as follows:

$$\dot{m}_{av} = \frac{V_0 \cdot \rho}{\Delta t_{eva}} \quad (2.1)$$

where, \dot{m}_{av} , V_0 , and Δt_{eva} are the average evaporation rate, initial volume, and total time of evaporation. Moreover, ρ represents the density of evaporating liquid. In this study, water is used as the evaporating fluid, and the density is considered to be 993kg/m³.

It should be noted that since the changes in the temperature were negligible, the uncertainty in the changes in the density is not considered. Furthermore, since the time scale (around 5 minutes) is relatively much larger than the uncertainties in of the measured time (± 1 second), the uncertainties due to time are not considered. However, the uncertainty in the initial volume of the water droplet is $\pm 4\%$. Therefore, the uncertainty of the calculated evaporation rate is around $\pm 4\%$. For further

analysis, the evaporation rate on mixed wettability samples is compared with those of the SiO₂ and Al₂O₃ samples. The relative evaporation rates are calculated as:

$$\dot{m}_{av}^* = \frac{\dot{m}_{av}^{(Mixed)}}{\dot{m}_{av}^{(Bare)}} \quad (2.2)$$

Here, $\dot{m}_{av}^{(Mixed)}$ and $\dot{m}_{av}^{(Bare)}$ are the average evaporation rates on mixed wettability and bare SiO₂ and Al₂O₃ samples. The maximum uncertainty in the \dot{m}_{av}^* is found to be $\pm 8\%$.

2.3 Elongated droplet evaporation

By performing an experimental study, the evaporation dynamics of high aspect ratio water droplets was investigated. Mixed wettability surfaces were used for elongation of water droplets. The aspect ratio of length to diameter was $l/D = 10$.

2.3.1 Experimental setup

Figure 2.12 represents the schematics of setup used in high aspect ratio elongated droplets. As seen in the figure, the experimental setup had two cameras which were used to record the changes in the droplet shape, from the both front and top views. In some experiments, the top camera was replaced with a thermal camera, which was used to obtain the interfacial temperature distribution. Moreover, a light source was used to provide brightness. Moreover, Figure 2.12 shows the actual experimental test section. As seen, the setup had a housing to minimize the effect of the surrounding airflow. This housing was much larger than the droplet size to avoid any vapor confinement inside the chamber. The experimental setup was equipped with five different cartridges, where their length and diameter were 80mm and 8mm, respectively. Moreover, the setup possessed a controller system so that the temperature remained within a specific range.

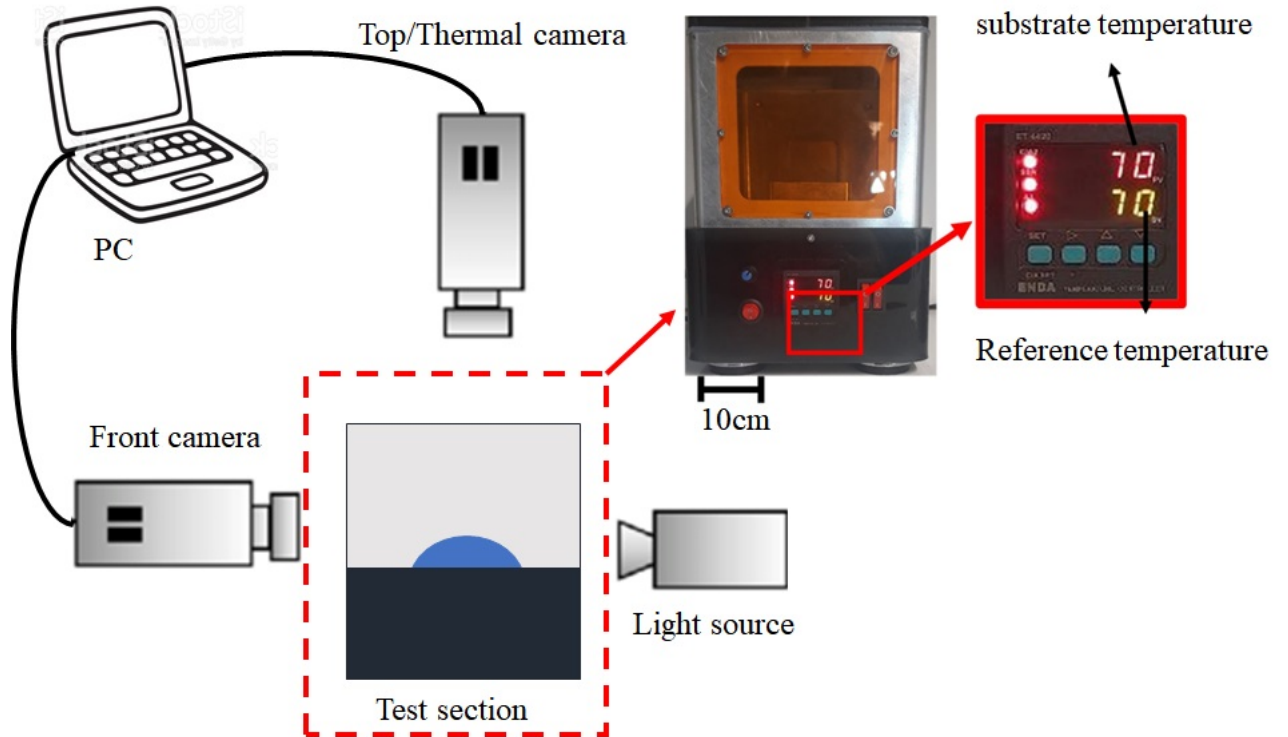


Figure 2.12 Schematic representation of evaporation setup

2.3.2 Experimental Procedure

Using a micro-pipet, 300 μ L of DI water was placed on the silicon region of the substrate which was fabricated before (See section 2.1.2). The transient changes in the dynamics of the droplet were recorded with time. The temperature and humidity of the environment were maintained at 20 $^{\circ}$ C \pm 1 $^{\circ}$ C and 60% \pm 5%, respectively. The substrate temperatures during the experiment were maintained at 35 $^{\circ}$ C \pm 1 $^{\circ}$ C and 70 $^{\circ}$ C \pm 1 $^{\circ}$ C. The initial contact angle of droplet on the elongated lines was 70.5 $^{\circ}$. Figure 2.13 shows different views of the elongated droplet on the fabricated sample.

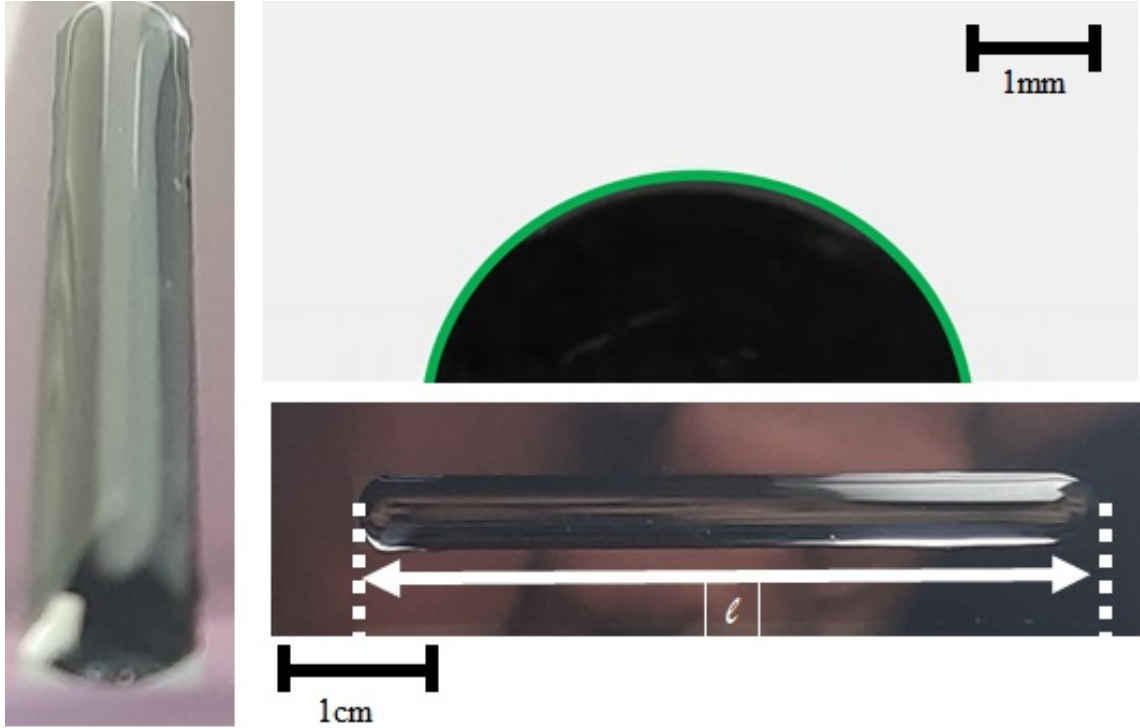


Figure 2.13 Top and side views of the elongated droplet

2.3.3 Data reduction

The changes in the contact angle are used to calculate the evaporation rate. In doing so, firstly, the volume of the remaining water droplet can be calculated as:

$$V(\theta) = \left[\frac{\pi}{4} \cdot \left(\frac{D}{2\sin(\theta)} \right)^2 - \frac{1}{8} \cdot \frac{D^2}{2\tan(\theta)} - \left(\frac{\pi}{4} - \frac{\theta}{2} \right) \cdot \left(\frac{D}{2\sin(\theta)} \right)^2 \right] \cdot l \quad (2.3)$$

where D , l , and θ are the width of the droplet, length of elongation, and contact angle, respectively. As the contact angle changes from θ_1 to θ_2 , the change in volume is given by:

$$\Delta V = V(\theta_1) - V(\theta_2) \quad (2.4)$$

The evaporated mass is calculated as:

$$m = \Delta V \cdot \rho \quad (2.5)$$

Considering the time, t , for these changes in the mass is to be known, the evaporation rate per length unit is calculated as:

$$\dot{m} = \frac{m}{t \times length} \quad (2.6)$$

Using the uncertainty analysis method proposed by Coleman and Steel [103], the maximum uncertainty in the evaporation rates was found as $\pm 8.4\%$, as summarized in Table 2.3.

Table 2.3 Uncertainty analysis of elongated droplet evaporation

Parameter	Uncertainty
Diameter	$\pm 20\mu\text{m}$
Contact angle	$\pm 1^\circ$
Length	$\pm 10\mu\text{m}$
Time	$\pm 0.1\text{s}$
Temperature	$\pm 1 \text{ (K)}$
Evaporation rate	$\pm 8.4\%$

2.4 Flow boiling

The effect of biphilicity of the samples on the flow boiling was investigated. The obtained results from the experiments were further analysed, and discussed in details.

2.4.1 Experimental setup

Figure 2.14 represents the schematic of the closed loop experimental setup used in this study. The micropump which provided the desired flow rate in the test section. Moreover, the test section is connected to the power supply. Also, a flow meter, a condenser, temperature and pressure sensors, and a reservoir are the other components of the test experimental setup. The obtained data are collected in the DAQ (Data Acquisition) device for further analysis.

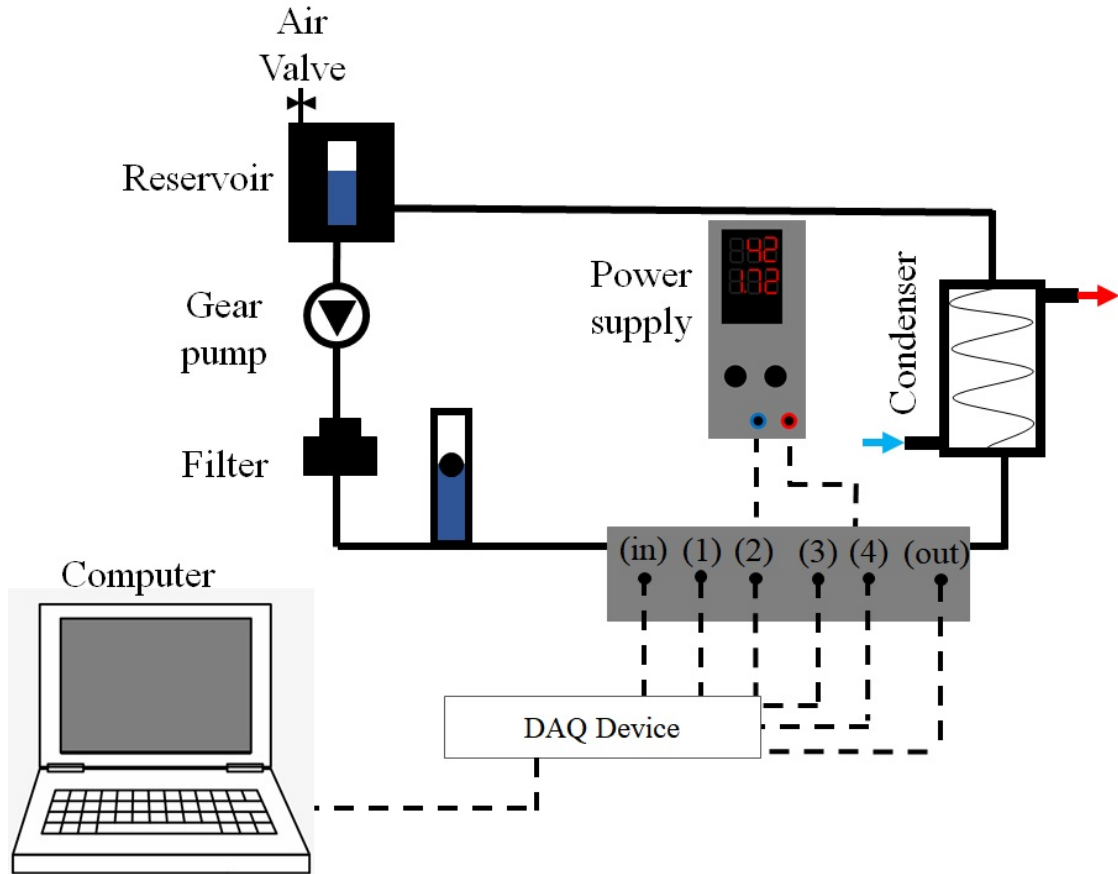


Figure 2.14 Schematic of the closed loop setup

The test section, which is shown in Figure 2.15a, consists of an aluminum block enclosed by the Teflon part to reduce heat losses during experiments. Furthermore, in order to measure the pressure and temperature at the inlet and outlet of the test section, two different small reservoirs were designed. The test specimens and a transparent cover are the other parts used in the test section. The aluminum base can house eight heating cartridges, each having a length of 65mm and a diameter of 6mm. The test samples were placed in the designed area with dimensions of 51.0mm×15mm. The depth of the channel is 1mm. Before placing the samples, the designed area was treated with a thermal paste to minimize the contact thermal resistance between the test sample and the aluminum block. The Plexiglas, sealed with a sandwich mechanism, was used for further visualization access. The local temperatures and heat fluxes were acquired under steady state conditions, which were collected by the data acquisition system. As seen in Figure 2.15b, the test section possesses four thermocouple locations, which are used for measurement of the temperatures. The first two thermocouple locations are used for calculation the HTC of the first half, while the others are used for the HTC of the second half of the channel.

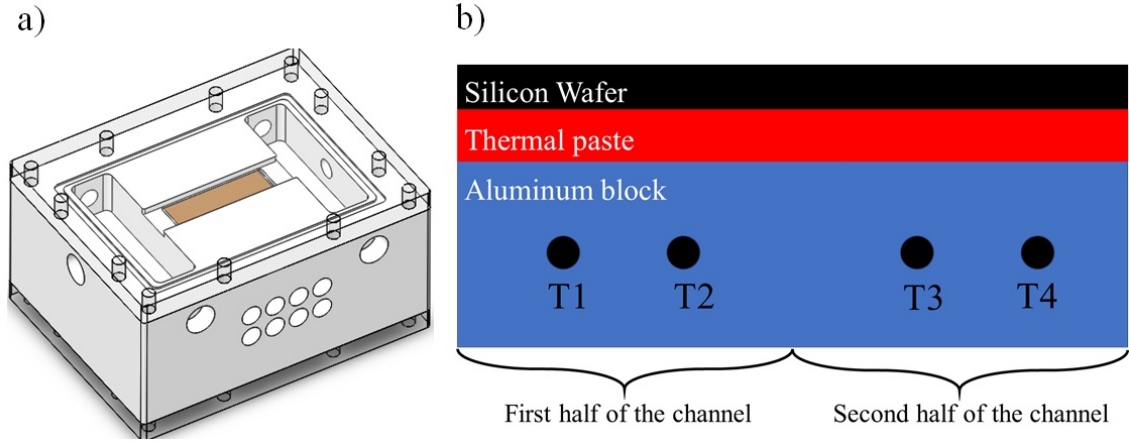


Figure 2.15 Schematic of a) test section b) thermocouple locations

2.4.2 Experimental Procedure

FC-72 was used as the working fluid in the experiments. The main physical properties of this fluid are summarized in Table 2.4. During the experiments, two different mass fluxes were provided by the gear pump. During the experiments, the inlet temperature was kept at $28 \pm 1^\circ\text{C}$. The data acquired from the experimental test section was under steady state conditions. The average values of temperatures provided by the first and second thermocouple locations were considered to calculate the average temperature of the first half of the surface (Figure 2.15b). Similarly, the third and fourth thermocouple locations were used to measure the average surface temperature at the second half of the channel. In order to ensure the repeatability of the tests, each test was repeated for at least three times. The average values of the experiments were used in the data reduction part.

Table 2.4 Physical properties of FC-72 and water

Properties	FC-72	Water
Boiling temperature (1atm)	56°C	100°C
Liquid density (25°C)	1680kg/m^3	997kg/m^3
Vapor density (boiling temperature)	13.24kg/m^3	0.59kg/m^3
Surface tension (25°C)	0.0105N/m	0.0720N/m
Liquid specific heat	1.1kJ/kg.K	4.13kJ/kg.K
Latent heat of vaporization (25°C)	88kJ/kg	2442kJ/kg
Liquid thermal conductivity (25°C)	0.057W/m.K	0.606W/m.K
Liquid viscosity (25°C)	0.64mPa.s	0.89mPa.s

2.4.3 Data reduction

During the experiments, the obtained voltage, current, and temperature data were reduced to obtain heat transfer coefficient. Moreover, the measured voltage and current values during the experiments were used to obtain the applied power as:

$$\dot{Q}_{net} = V.I \quad (2.7)$$

where \dot{Q}_{net} is the applied power(W), and V and I are the measured voltage(V) and current(A), respectively. Considering that some percentage of the applied power was lost, the heat flux applied to the surface was calculated as:

$$q'' = \frac{\dot{Q}_{net} - \dot{Q}_{loss}}{A_s} \quad (2.8)$$

Here, \dot{Q}_{loss} is the heat loss, and A_s is the area of the heated surface. \dot{Q}_{loss} was calculated from single phase flow heat transfer. In doing so, single phase FC-72 is introduced to the test section and the inlet and outlet temperatures were measured. Considering that the mass flow rate and specific heat of the working fluid were known, the heat loss was obtained as:

$$\dot{Q}_{loss} = \dot{Q}_{net} - \dot{m}c_p(T_{out} - T_{in}) \quad (2.9)$$

Using the curve fit technique, the heat losses were estimated at higher temperatures. The heat transfer coefficient HTC was found as:

$$h = \frac{q''}{T_w - T_f} \quad (2.10)$$

where T_w is the temperature of the heated surface ($^{\circ}\text{C}$), and T_f is the temperature of the working fluid ($^{\circ}\text{C}$). In order to calculate the temperature at the surface (T_w), the temperature measured at the j^{th} location of temperature measurement and the calculated heat fluxes were used as follows:

$$T_{w,j} = T_j - q'' \left(\frac{\delta_{Al}}{\kappa_{Al}} + R_p + \frac{\delta_{Si}}{\kappa_{Si}} \right) \quad (2.11)$$

Here, $T_{w,j}$ is the temperature of the substrate at the j^{th} location ($j = 1\text{to}4$), T_j is

the temperature read from the j^{th} thermocouple location. Moreover, L_{Al} and L_{Si} are the thickness of aluminum and silicon samples, respectively, while K_{Al} and K_{Si} are their thermal conductivities. Furthermore, R_p is the thermal resistance of the thermal paste.

For subcooled boiling experiments, the fluid temperature was calculated via the energy balance equation (equation 2.12). Since the pressure drop is not substantial (less than 1kPa), the saturation temperature is assumed to be constant along the channel. Considering constant heat flux applied to the system, the temperature of the fluid could be obtained as:

$$\begin{aligned} T_{f,x} &= T_i + \frac{\dot{q}'' \cdot A_x}{\dot{m} c_p} & \text{if } T_{f,x} < T_{sat} \\ T_{f,x} &= T_{sat} & \text{if } T_{f,x} \geq T_{sat} \end{aligned} \quad (2.12)$$

Here, T_i is the inlet temperature ($^{\circ}\text{C}$), and c_p is the specific heat capacity of the fluid ($\text{J}/\text{kg}\cdot^{\circ}\text{C}$). Moreover, A_x is the heated area starting from the inlet to the point of interest. Using the uncertainty analysis proposed by Coleman and Steel [103], the maximum uncertainty in the HTC was found as $\pm 7\%$ (Table 2.5).

Table 2.5 Uncertainty parameters and analysis of flow boiling tests

Parameter	Uncertainty
Voltage	$\pm 1\text{V}$
Current	$\pm 0.01\text{A}$
Temperature	$\pm 0.1\text{K}$
Mass flow rate	$\pm 5\%$
Height of the channel	$\pm 15\mu\text{m}$
Heat transfer coefficient	$\pm 7\%$

2.4.4 Validation of the test section

In order to make sure that the experimental setup works properly and the obtained results are reliable, single-phase heat transfer tests were performed to validate the setup. First, the heat flux was applied, and the temperatures were measured at the inlet and outlet of the test section. Meanwhile, the temperature at the different

locations of the surface was measured. Considering the obtained temperatures at the inlet and outlet, the heat transfer to the fluid was calculated as:

$$\dot{Q} = \dot{m}c_p(T_{out} - T_{in}) \quad (2.13)$$

later on, the average heat transfer coefficient was obtained as:

$$h = \frac{\dot{Q}}{A_s.(T_w - T_f)} \quad (2.14)$$

where T_f and T_w are the average temperatures of the fluid and substrate, respectively. Considering that the heat transfer coefficient was known, the Nusselt number was calculated as $Nu = (hD_H)/\kappa$, where D_H and κ are the hydraulic diameter of the channel and heat conductivity of the fluid, respectively. Moreover, Reynolds number was calculated as:

$$Re = \frac{\dot{m}D_H}{A_c\mu} \quad (2.15)$$

Here, μ is the viscosity of the working fluid. The obtained Nusselt numbers were compared with the correlations provided (equation 2.16) by Shah and London [104]:

$$\begin{aligned} Nu &= 1.953 \left(Re.Pr. \frac{D_H}{L_{ch}} \right)^{1/3} & \text{where} & \quad \left(Re.Pr. \frac{D_H}{L_{ch}} \right) \geq 33.3 \\ Nu &= 4.364 + 0.0722 \left(Re.Pr. \frac{D_H}{L_{ch}} \right) & \text{where} & \quad \left(Re.Pr. \frac{D_H}{L_{ch}} \right) < 33.3 \end{aligned} \quad (2.16)$$

The comparison of the results is presented in Figure 2.16. As seen in the figure, the obtained experimental results are in good agreement with the predictions of the correlation.

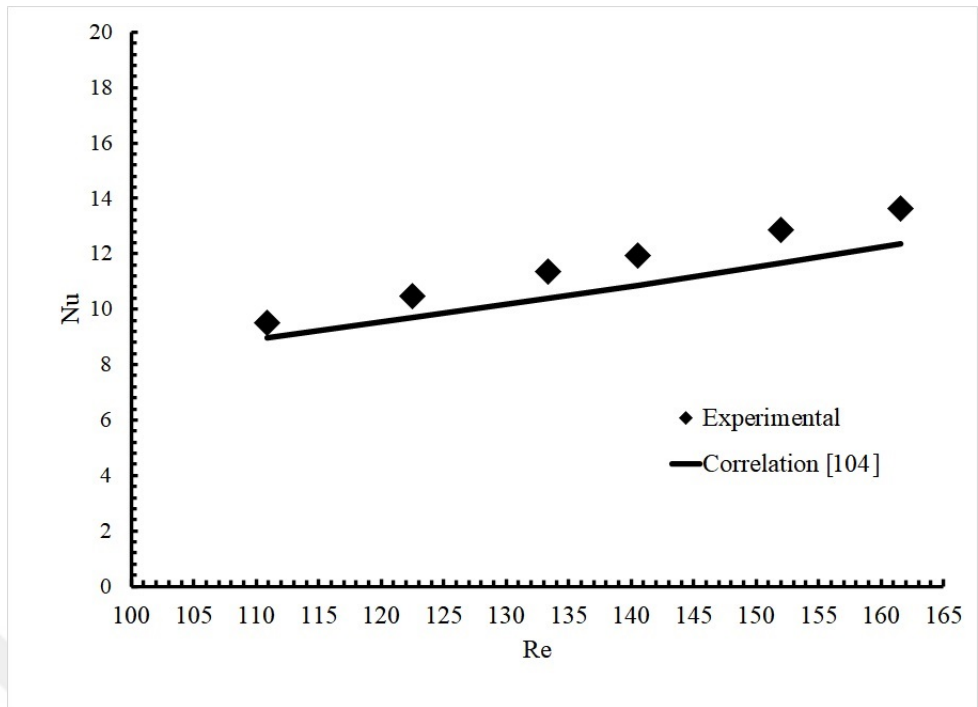


Figure 2.16 Validation of the experimental setup

3. NUMERICAL SIMULATIONS OF DROPLET EVAPORATION

The quasi-steady numerical analysis was performed for evaporating cylindrical droplets to reveal the effects in liquid and gas-phase domains via a fully coupled model, similar to the research studies performed by other researchers, such as Janocha and Tsotsas [105]. In this fashion, only the early stage of droplet evaporation is investigated. At this stage, the internal and external flow dynamics have been evolved adequately, confirming that the slight variations in the contact angle have no significant effect on the temperature and velocity fields at the initial stages. This in turn allows obtaining a snapshot of the dynamics of flow in the two-phase domain instead of full evaporation induced skewed results. Similar observations have been made by some researchers van Gaalen et al [106]. The model further reveals the effect of droplet adjacency on evaporative heat and mass transfer. Using the data obtained from experiments, as well as data provided by Mahmud and MacDonald [107], first, the quasi-steady model is validated for the single spherical droplet case. Thereafter, the effect of the distance between the droplets, droplet radius, surface temperature, and the effect of considering Marangoni flow, Stefan flow, and natural convection are investigated for single and adjacent droplets. The Bond number $Bo = \rho gh^2/\sigma$ of the droplets is smaller than unity in all the cases. This is justified by the droplets' size being smaller than the capillary length. Therefore, the effect of gravitational forces on the shape of the droplet is neglected and droplets are considered as cylindrical-shaped domains in the simulations and possess high aspect ratios ($AR = Length/D$). Regarding the high substrate temperature considered at the surface, both diffusive and convective terms of the vapor transport equation are considered. To avoid additional computational costs, the simulated domains are considered to be 2D. Figure 3.1a illustrates the schematic configuration of droplets.

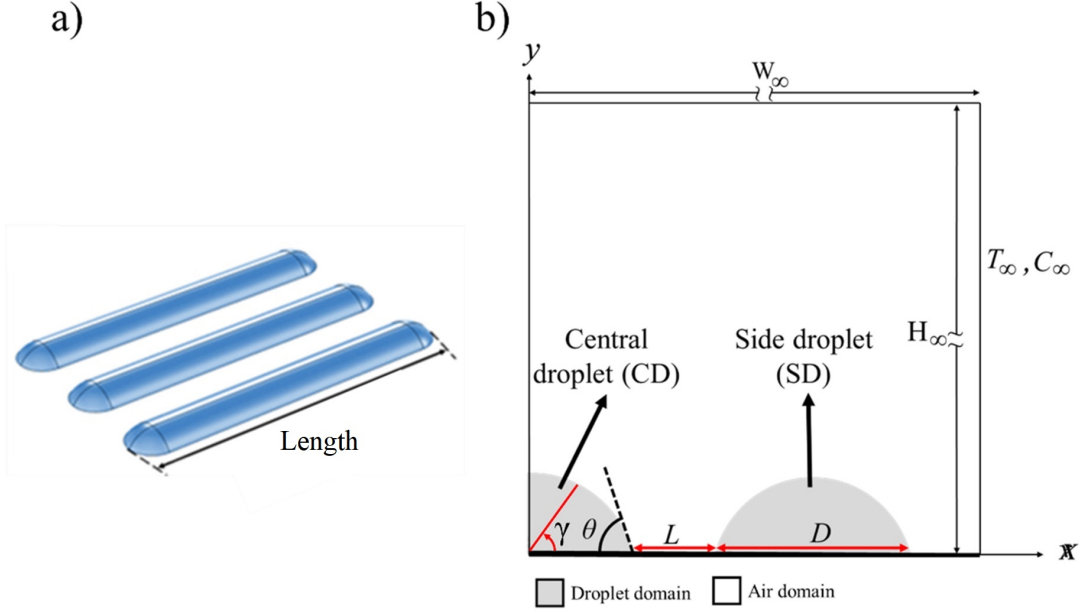


Figure 3.1 a) Schematic configuration of the droplets; b) Geometric details of the droplets

3.1 Governing equations

The governing equations include conservation of mass, momentum, and energy at both the liquid and the gas phases. Moreover, vapor transport through the gas phase is considered in the gas phase:

$$\nabla \cdot (\rho \vec{u}) = 0 \quad (3.1)$$

$$\rho(\vec{u} \cdot \nabla) \vec{u} = \rho \vec{g} - \nabla p + \mu \nabla^2 \vec{u} \quad (3.2)$$

$$\vec{u} \nabla T = \alpha (\nabla^2 T) + \Phi \quad (3.3)$$

$$-\vec{u} \cdot \nabla C_v + \nabla \cdot (D_{w-air} \nabla C_v) = 0 \quad (3.4)$$

In these equations, ρ , \vec{u} , \vec{g} , p , μ , T , and C_v are the density of the fluid, velocity vector,

gravitational acceleration, pressure field, the viscosity of the fluid, temperature, and vapor concentration, respectively. Furthermore, D_{w-air} is the temperature-dependent diffusivity coefficient of vapor in air [108]. Moreover, α is the thermal diffusivity of the fluid, and Φ is the viscous dissipation term. To simulate natural convection in the gas and liquid domains, a weakly compressible approach is applied to the model. Regarding the small magnitude of the velocity vector and relatively small dimensions of the geometry, the flow is considered to be laminar in both the droplet and gas domains.

3.2 Boundary conditions

Figure 3.1a shows the simulated domain. The liquid and gas domains are simulated separately. The boundary conditions in both domains are as follows:

- i In the y-axis, the symmetry boundary condition is considered for all the equations. This boundary condition for equations 3.1 and 3.2, 3.3, and 3.4 can respectively be written as:

$$\vec{u} \cdot \vec{n} = 0 \quad (3.5)$$

$$\vec{q} \cdot \vec{n} = 0 \quad (3.6)$$

$$\nabla C_v \cdot \vec{n} = 0 \quad (3.7)$$

- ii In the x-axis, for equations 3.1 and 3.2, a no-slip boundary condition is imposed at this boundary.

$$\vec{u} = \vec{0} \quad (3.8)$$

Moreover, the constant temperature boundary condition is applied (equation 3.3).

$$T = T_s \quad (3.9)$$

Finally, equation 3.4 requires no-vapor penetration considering the nature of the domain.

$$\nabla C_v \cdot \vec{n} = 0 \quad (3.10)$$

- iii The outer boundaries are considered as much larger than the size of the droplets to enable the simulation of natural convection around the droplet without affecting the outer boundaries. At the outer boundaries, the ambient conditions are assumed. Table 3.1 shows the dimensions of the simulated domain. The applied boundary conditions are as follows:

$$\nabla \vec{u} \cdot \vec{n} = 0 \quad (3.11)$$

$$T = T_\infty \quad (3.12)$$

$$C_v = \phi_\infty C_{v,sat} \quad (3.13)$$

Table 3.1 Domain characteristics

Parameter	Value(s)	Parameter	Value(s)
R	0.5mm to 5mm	θ	70°
T_∞	20°C	T_s	35°C to 70°C
ϕ_∞	60%	L	$0.05 \times R$ to $20 \times R$
W	$100 \times R$	H	$150 \times R$

The boundary conditions at the interface are inextricably coupled. For instance, the velocity of the air at the interface is dependent on the evaporative mass flux leaving the droplet domain. On the other hand, since the velocity magnitude at the interface changes the gradient of the vapor in the gas domain, the evaporative heat flux is also dependent on the vapor concentration gradient. Therefore, the applied boundary conditions in the air domain are interdependent. The iterative algorithm developed by Akkus et al [72] for a sessile water droplet evaporation was modified and used to solve the conservation equation at the liquid/gas boundary. The algorithm used in this study is summarized as follows:

- i The applied equations are solved in the gas domain. The solution needs initial guesses for the interfacial temperature distribution, as well as tangential and normal velocities. In this regard, the substrate temperature is applied to the interface as the initial guess, and the velocity is considered to be zero. Moreover,

saturation condition is considered at the interface.

$$\vec{u} = \vec{0} \quad (3.14)$$

$$T = T_s \quad (3.15)$$

$$C_v = C_{v,sat} \quad (3.16)$$

Using these boundary conditions, the governing equations in the gas domain are solved.

- ii After solving the governing equations in the gas domain, the evaporative mass flux at the interface is calculated as:

$$\dot{m}'' = -D_{w-air}(\nabla \cdot \vec{n})C_v + (\vec{u}_g \cdot \vec{n})C_v \quad (3.17)$$

Here, D_{w-air} is the diffusion coefficient, \dot{m}'' is the evaporative mass flux, and $\vec{u}_g \cdot \vec{n}$ is the normal component of the velocity vector in the air domain, which is calculated as:

$$D_{w-air}(\nabla \cdot \vec{n})C_{air} = (\vec{u}_g \cdot \vec{n})C_{air} \quad (3.18)$$

where C_{air} is the concentration of air molecules. This equation can be further simplified, and the magnitude of the Stefan flow can be calculated as:

$$\vec{u}_g \cdot \vec{n} = \frac{D_{w-air}}{C_{air}} \cdot \frac{\partial C_{air}}{\partial \vec{n}} \quad (3.19)$$

Subsequently, the evaporative heat flux and the shrinking normal velocity of the interface are calculated, respectively, as:

$$\dot{q}_{eva}'' = \dot{m}'' \cdot h_{fg} \quad (3.20)$$

$$\vec{u}_l \cdot \vec{n} = \frac{\dot{m}''}{\rho} \quad (3.21)$$

In these equations, \dot{q}_{eva}'' is the evaporative heat flux, h_{fg} is the latent heat of

evaporation and \vec{u}_l is the shrinking velocity vector of the droplet domain. The total heat flux from the droplet calculated is expressed as follows:

$$\dot{q}'' = \dot{q}_{eva}'' + \dot{q}_{con}'' + \dot{q}_{rad}'' \quad (3.22)$$

where the \dot{q}_{con}'' and \dot{q}_{rad}'' are the heat flux due to conduction and radiation heat transfer at the interface. It is worth mentioning that the emissivity of the surface is considered as 0.97 [109].

- iii The velocities and heat flux calculated from equations 3.21 and 3.22 are applied as the evaporative heat flux at the interface. In order to calculate the tangential velocity in the presence of Marangoni flow, neglecting the shear stress of the gas domain on the interface of the droplet, the tangential force balance can be written as:

$$\nabla\sigma.\vec{t} = -\mu(\nabla.\vec{u}_t).\vec{n} \quad (3.23)$$

Here, σ is the surface tension, and \vec{t} and \vec{n} are tangential and normal directions, respectively. The validity of this statement is proven after the simulations. The predicted shear force due to the liquid motion is at least 40 times larger than that of the gas motion.

The tangential velocity vectors and interfacial temperatures calculated from the equations 3.23 are used at the interface of the gas phase, due to the non-slip boundary condition assumption. The normal component of the velocity, on the other hand, which is also known as the Stefan flow, plays an important role in the evaporation rate, which necessarily should be considered [72]. Stefan flow is calculated in equation 3.19.

Moreover, from solutions of the liquid domain, temperature distribution is obtained before. These obtained velocities are applied as boundary conditions at the interface of the gas domain regarding the equations 3.1, 3.2, and 3.3. Moreover, for equation 3.4, the saturation conditions is considered ($\phi = 1$), as mentioned before. This boundary conditions are applied to the gas domain, and the governing equations are solved, again.

These three steps are repeated until convergence is obtained. For convergence, a maximum error of 10^{-5} is considered for the evaporative mass flux at the interface. Figure 3.2 provides the flowchart of the described algorithm.

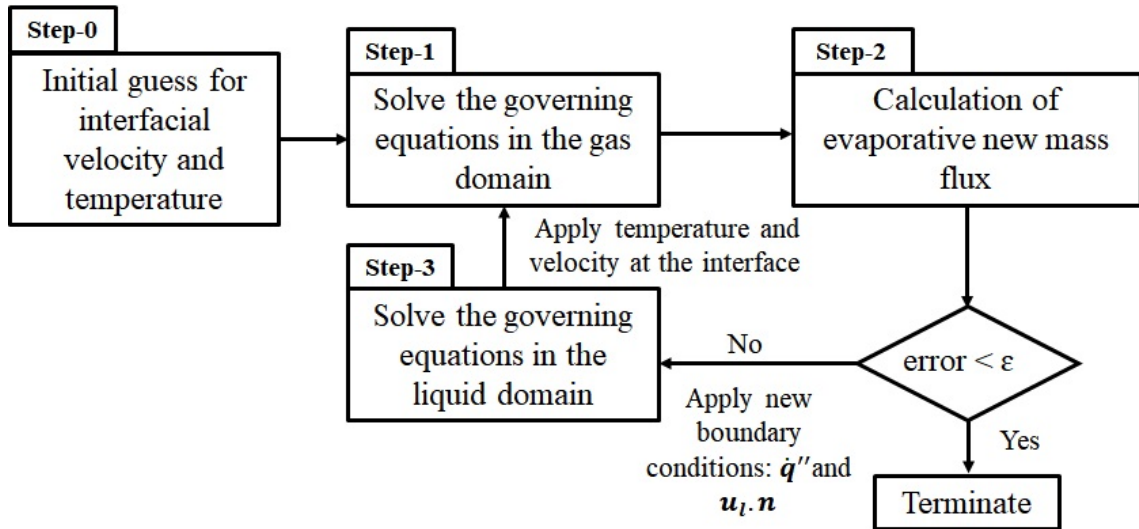


Figure 3.2 Flowchart of the applied algorithm

3.3 Mesh independency analysis

To determine the effect of the mesh size on the obtained results, several different mesh sizes with element numbers ranging from 1.12×10^4 to 1.22×10^5 are utilized. Figure 3.3a shows the numerical domain. Tetrahedral mesh elements are used for the majority of both liquid and gas domains. Since the heat and mass transfer occurs at the liquid/gas interface, more refined quad elements are used to increase the model accuracy. Figure 3.3b shows the predicted heat and mass flux as versus the mesh element number. As the mesh number grows from 7.52×10^4 to 1.22×10^5 , the heat and mass flux changes in percentage are 0.04% and 0.01%, respectively. Therefore, the mesh with the element number of 7.52×10^4 is used to reduce the computational cost.

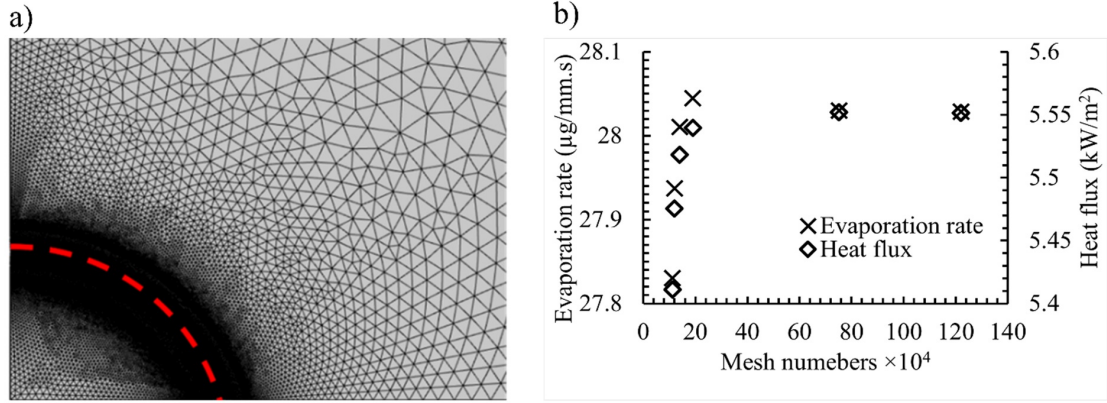


Figure 3.3 a) Grid distribution inside and near the droplet, b) mesh independency study

3.4 Model validation

The developed model is validated against the experimental results of Mahmud and MacDonald [107]. In the validated case, the droplet had the contact radius and angle of 2.5mm and 90°, respectively. The temperatures of the substrate were 39°C and 74°C. The relative humidity of the ambient was reported to be 25%, and the experiments were conducted at atmospheric pressure. At the surface temperatures of 39°C and 74°C, the reported evaporation rates were $24.5 \pm 1.7 \mu\text{g/s}$ and $165.7 \pm 11.4 \mu\text{g/s}$, respectively, while the predicted evaporation rates are $24.19 \mu\text{g/s}$ and $163.38 \mu\text{g/s}$, respectively. According to the obtained results shown in Figure 3.5a and Figure 3.5b, the developed algorithm predicts the results with a maximum error of 1.4%. It should be noted that the interface was divided into arcs in the algorithm as developed by Akkus et al. [72], where a maximum error of 18.2% compared to the experimental results of Mahmud and MacDonald [107] was reported. However, in this study, instead of dividing the interface into smaller arcs, the iterative equations are applied to each interface node, which may be the reason for improved evaporation rate predictions.

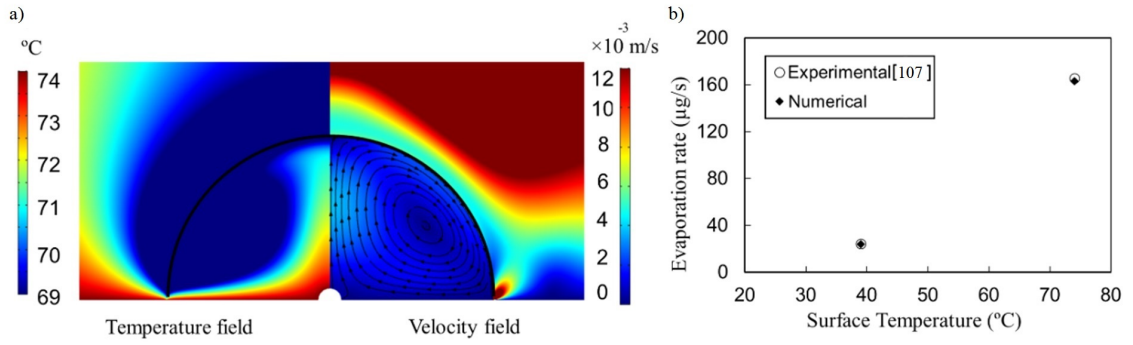


Figure 3.4 a) temperature and velocity fields, b) validation of the model: numerical results versus experimental data[107]

Moreover, the model is validated against the experimental data provided in this study. In doing so, the evaporation rate of the droplets is calculated while the contact angle changes from 70° to almost 60° . Similar to the case of Mahmud and MacDonald [107], the contact radius of the elongated droplets is 2.5mm, and the contact angle of the simulated cases was considered to be 70° . The temperatures at the substrate were set at $35^\circ \pm 1^\circ\text{C}$ and $70^\circ \pm 1^\circ\text{C}$. The experimental evaporation rates were obtained as $1.68 \pm 0.13 \mu\text{g}/\text{mm.s}$ and $18.68 \pm 1.49 \mu\text{g}/\text{mm.s}$, respectively. The evaporation rates obtained from the simulations for the surface temperatures of 35°C and 70°C are $2.01 \mu\text{g}/\text{mm.s}$ and $28.03 \mu\text{g}/\text{mm.s}$ in the presence of Marangoni effect and $1.78 \mu\text{g}/\text{mm.s}$ and $18.69 \mu\text{g}/\text{mm.s}$ in the absence of Marangoni effect, respectively. Since Marangoni flow can be easily suppressed due to the presence of contaminants in the environment [110], along with the results obtained from the simulations, it can be concluded that the Marangoni effect was absent in the experiments. Therefore, the developed model predicts the evaporation rates at the surface temperatures of 35°C and 70°C with errors of 3.18% and 0.1%, respectively. Furthermore, Figure 3.5 shows the comparison in the obtained interfacial temperature distributions between the experimental and simulation results. As seen in the figure, the numerical and experimental results are in good agreement.

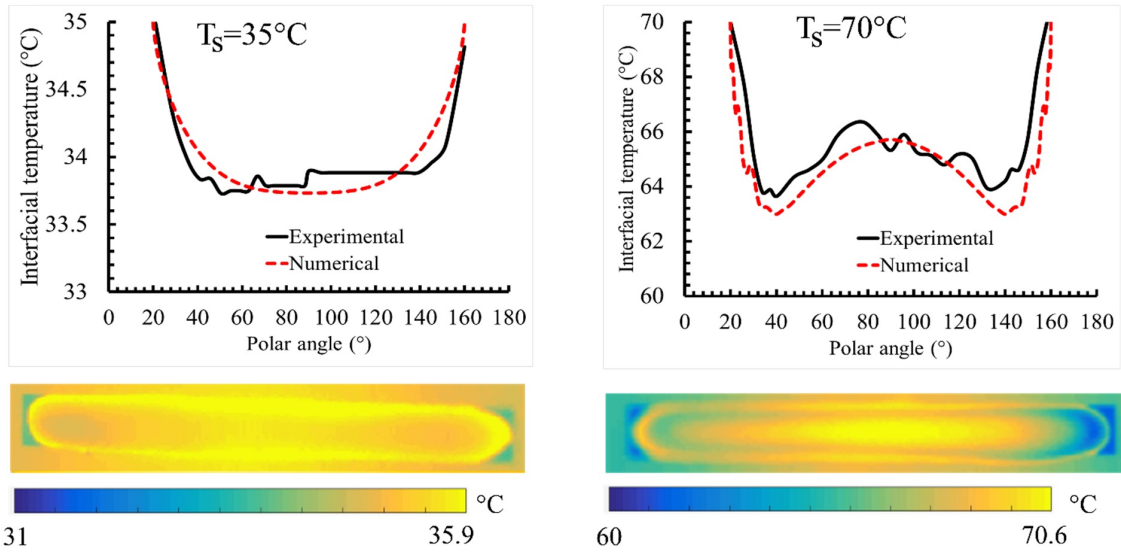


Figure 3.5 Comparison between the experimental and numerical interfacial temperature distributions

4. RESULTS AND DISCUSSION

This chapter includes results and discussion of the numerical and experimental results. Firstly, the results of the both spherical and high aspect ratio elongated droplets evaporation are presented. Later on, the results regarding the results of flow boiling experiments are presented and discussed.

4.1 Droplet evaporation

In this section the results regarding the evaporation of water droplets are discussed. In doing so, first the experimental results obtained for the spherical water droplets on mixed wettability samples are provided (4.1.1). Later on, both experimental and numerical results of the high aspect ratio elongated droplets are presented (4.1.2)

4.1.1 Evaporation dynamics of droplets on mixed wettability samples

As a reference to mixed wettability samples, it is worthwhile to first investigate the evaporation dynamics on simple SiO_2 and Al_2O_3 substrates. The initial water contact angle on the silicon SiO_2 was 30° . The lifetime of an evaporating droplet on SiO_2 can be categorized into three stages. First, the droplet starts to evaporate at CCR mode for the first 61% of its evaporation time. At the second stage, which corresponds to 22% of its lifetime, the droplet evaporates in a CCA mode. For the rest (of 17% evaporation lifetime), a mixed-mode was observed. The total evaporation time was 531 seconds. Figure 4.1 the droplet evaporation on the SiO_2 substrate.



Figure 4.1 Evaporation of water droplet on SiO₂ substrate

On the other hand, the initial water contact angle on the aluminum oxide sample was 65°. Similarly, the Al₂O₃ sample shows three different stages of evaporation lifetime. The droplet starts to evaporate at a CCR mode for more than 80% of its evaporation time. At the second stage, a transient CCA mode was observed which almost lasted for 2% of the evaporation lifetime. The rest of the evaporation took place in a mixed-mode. The total evaporation time for the droplet on aluminum oxide sample was 544 seconds, which is shown in Figure 4.2

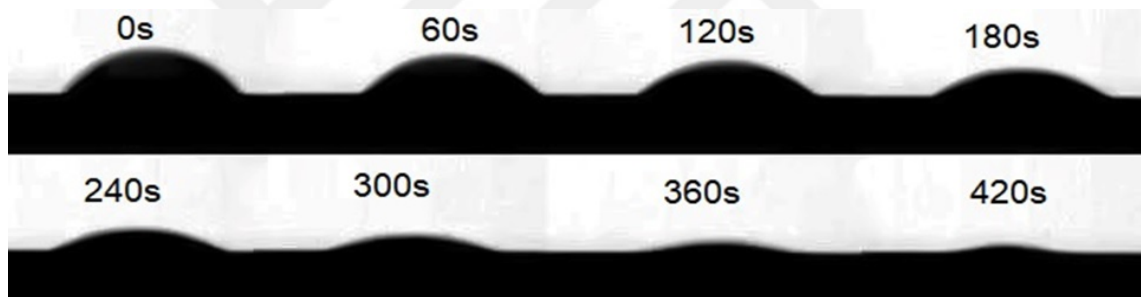


Figure 4.2 Evaporation of water droplet on Al₂O₃ substrate

Even though the initial contact angle of the droplet on the SiO₂ is smaller than that of Al₂O₃ sample, their evaporation time is almost the same. The result arises from the fact that the droplet on Al₂O₃ has a tendency to evaporate at a CCR mode, and the triple line of the droplet remains almost the same for more than 80% of its evaporation time. However, on the SiO₂ sample, the radius of the droplet starts to shrink much sooner, which ends up lowering the evaporation rate at the CCA state.

As mentioned before, more than 80% of the evaporation on the Al₂O₃ takes place in a CCR mode. It means that during this time the droplet maintains the maximum possible TCL. Also, conduction through the droplet becomes more dominant as evaporation proceeds. Based on these two reasons, even though the droplet on the Al₂O₃ has a larger initial contact angle, since the TCL is maintained for the most time of evaporation, the smaller evaporation rate at the early stage of the water droplet on Al₂O₃ sample is compensated.

Even though the evaporation rate of the water droplet on the SiO_2 is almost equal with that of Al_2O_3 counterpart, mixed wettability surfaces show different evaporation rates. The experiments show that the evaporation rate of the droplet on mixed wettability surfaces is a function of the shape and the size of the islands. Figure 4.3 shows a comparison of the evaporation rate on different surfaces with respect to evaporation rate on the SiO_2 sample. As mentioned before, the experiments are done on three different shapes of islands: the rhombus (R), square (S), and circle (C). The sizes of the islands are one time (L), one-fourth times (M), and one-sixteenth times (S) of the droplet radius. As can be inferred from Figure 4.3, the square-shaped islands are not promising for heat transfer enhancement. However, the rhombic and circular shaped islands enhance the evaporation rate. Besides, it can be concluded that the circular shape islands enhance the evaporation rate much better than the rhombic islands.

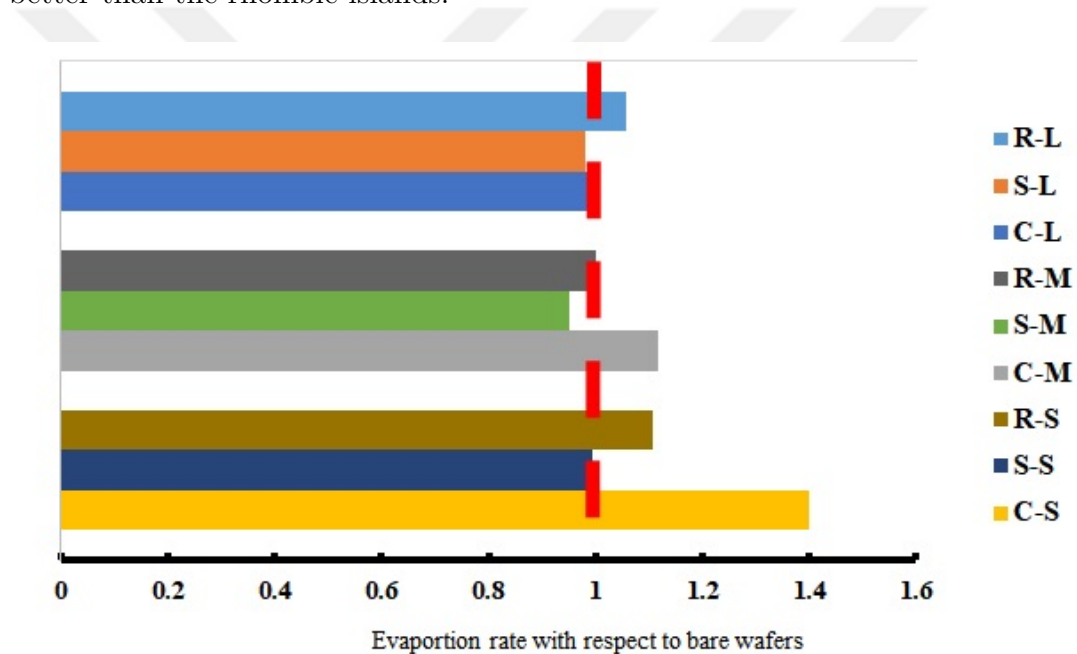


Figure 4.3 Comparison of evaporation rate on different surfaces with respect to SiO_2 sample

Another parameter, which affects the evaporation rate, is the sizes of the islands. As can be seen in Figure 4.3, smaller sizes of the islands generally show better enhancement of the evaporation rate in comparison with larger counterparts. This reason arises from the fact that the smaller islands can modify the shape of the TCL much easier. Figure 4.4 the evolution of the TCL on a surface with circular-shaped islands. It should be noted that evaporation rate on surface with small size circular islands was enhanced by more than 1.4 times in comparison with SiO_2 sample.



Figure 4.4 Evolution of TCL on mixed wettability surfaces

Moreover, it is worthwhile to claim that during the evaporation split of the droplets could be seen on the circular-shaped islands. Figure 4.5 shows the split droplets on medium-size and small-size circular-shaped surfaces, respectively. After the split of the droplet on circular islands, the evaporation rate suddenly increased.

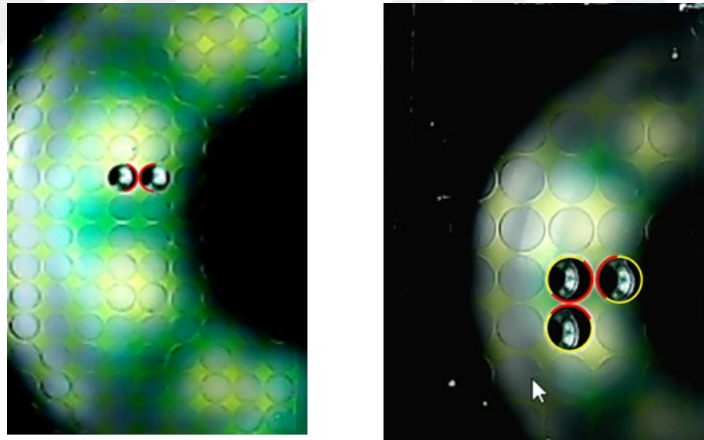


Figure 4.5 Split of water droplet on circular islands, the red lines represent the inner boundaries

The considerable point is that in all experiments, after split of the droplet, evaporation of group droplets is dominant at the outer boundary of the group droplets. The reason for this can be explained by the numerical analysis, in section 4.1.2. As can be expected from the velocity field of the air domain, at the inner boundary the natural convection does not provide unsaturated air from the outside. Therefore, the TCL is in contact with more vapor concentration in respect to the outer boundaries, and as a matter of fact, the evaporation due to less concentration of vapor tends to be larger at the outer boundaries. Figure 4.6 shows a snapshot of

evaporation of a group of split droplets. As seen, the outer boundaries are totally dried out, while a the inner boundaries water is still remained.

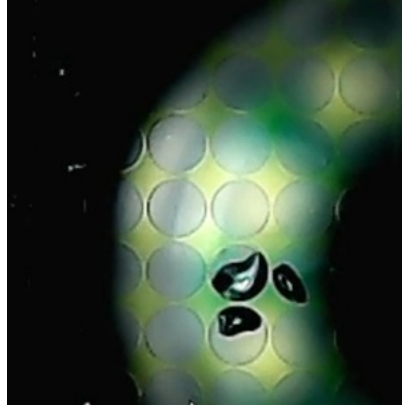


Figure 4.6 Evaporation of group of split droplets

4.1.2 Evaporation dynamics of high aspect ratio elongated droplets

In this section, first, the obtained results for a single elongated droplet are discussed. Using the developed model, evaporation dynamics of high aspect ratio droplets, including both CD (central droplet) and SD (side droplet), is presented. Moreover, the effects of droplet size D on velocity and temperature fields in the gas and liquid phases are included. Next, the effects of dimensionless pitch distance L/D and wall superheat ΔT on the flow and temperature fields around and inside the droplet are covered. Finally, the effect of the temperature field on the vapor phase and mass transfer is analyzed.

4.1.2.1 Single cylindrical droplet

Figure 4.7a shows the variation in contact angle and contact lines of an elongated droplet at $T_s=35^\circ\text{C}$. Similar to a spherical droplet [42], initially the elongated droplet evaporates while the contact line is fixed, and a decrease in the contact angle is observed. This stage accounts for most of the evaporation time. As seen in Figure 4.7b, from $t^* = 0.00$ to $t^* = 0.80$, the contact angle decreases from 70° to a receding contact angle, which is relatively close to 0° . During this stage (stage I), the volume changes almost linearly with respect to time (Figure 4.7c). As the contact angle reaches the

receding contact angle, the evaporation dynamics of the droplet change (stage II), where a very thin liquid film evaporates. However, the contact area decreases during this stage of evaporation. Generally, in a spherical droplet, the contact radius changes almost homogeneously in the CCA stage. However, the experimental results show that the contact area of the elongated droplet decreases from one end (curved side) and ends up to the other side. At stage II, the evaporation rate shows a linear trend, considerably lower than that of stage I.

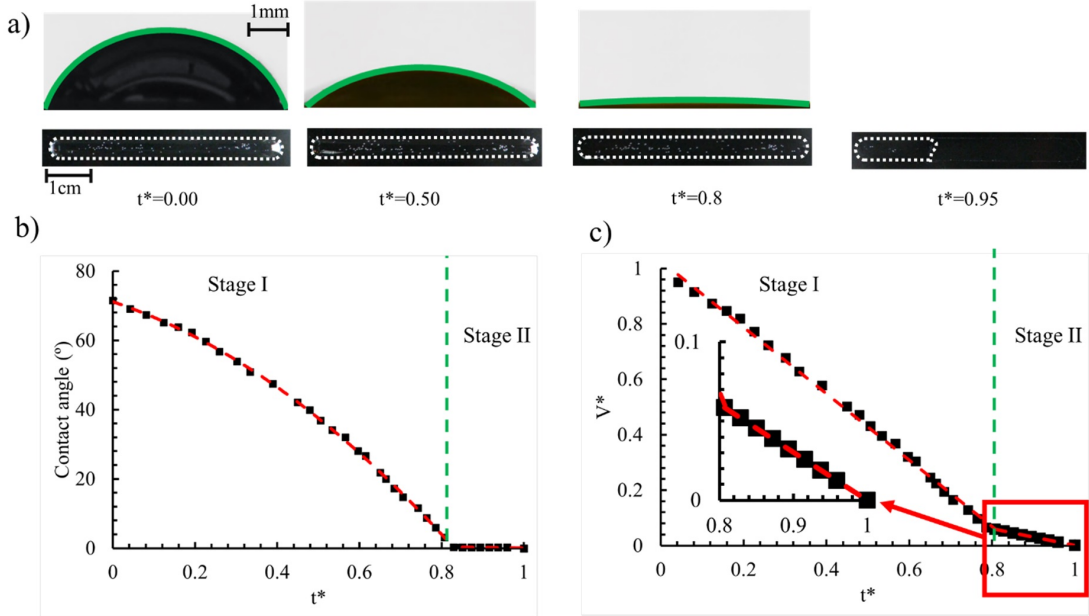


Figure 4.7 a) Changes in the contact angle and contact area of elongated droplets b) changes in contact angle as a function of time c) transient changes of the droplet volume

Having validated the numerical model (See Section 3.4), the velocity and temperature distributions inside the droplet are investigated. Figure 4.8a and b show the temperature and velocity distributions inside an elongated droplet in the absence of Marangoni flow at surface temperatures of 35°C and 70°C , respectively. In the absence of Marangoni flow, the buoyancy driven flow inside the elongated droplet is from the apex to the substrate. Similar buoyant flows were previously reported for spherical droplets [72, 111]. At the superheat temperature of 15°C ($\Delta T = T_s - T_\infty = 15^\circ\text{C}$), the buoyant flow is not strong enough to change the uniformity of temperature distribution inside the droplet. However, as the superheat temperature increases to 50°C , the buoyant flow results in distortion in isotherms inside the droplet.

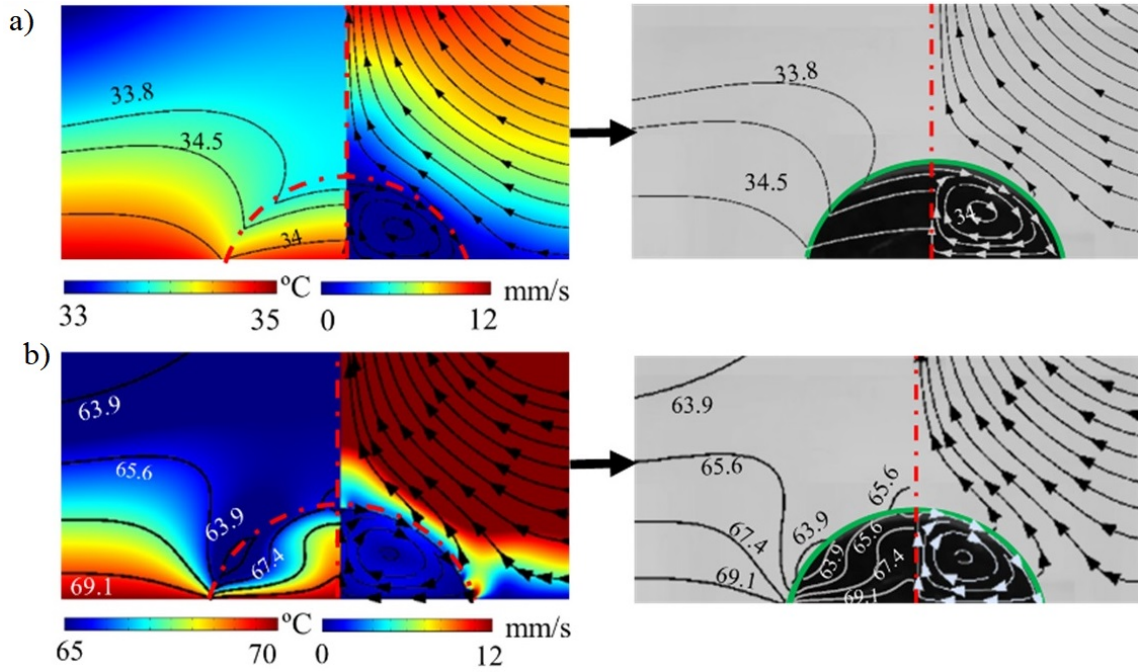


Figure 4.8 Velocity and temperature fields at the superheat temperatures of a) 15°C b) 50°C

As depicted in Figures 4.9, the flow inside each half of the droplet can be divided into four different flow regions at both temperatures. First, the flow is from the apex to the contact line which is known as the capillary flow and plays an important role in the coffee ring effect. Parallel to the substrate, another flow is predicted, which is from the contact line to the center of the droplet at the vicinity of the substrate. Another flow is predicted to be from the substrate towards the apex of the droplet. Furthermore, circulation is found inside the droplet.

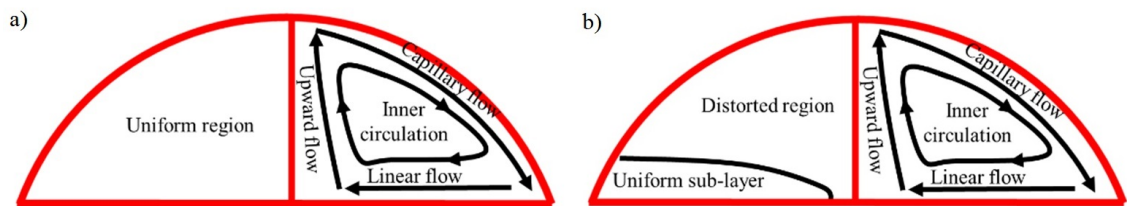


Figure 4.9 Schematics of internal circulations at superheat temperatures of a) 15°C b) 50°C

In contrast to the velocity profile, its temperature counterpart shows more variations with superheat temperature. At superheat temperature of 15°C, as seen in Figure 4.10a, the interfacial temperature uniformly decreases from the contact line to the apex. However, at superheat temperature of 50°C, the temperature profile has two different regions. First, a uniformly distributed sub-layer is found near the substrate, as depicted in Figures 4.9b and 4.10b. Regarding the flow direction,

the iso-terms are squeezed near the contact line, while at the center of the droplet the upward flow stretches the iso-terms (see Figure 4.8). At the upper part of the uniformly distributed sub-layer, the temperature profile is affected by buoyant flow, which results in changes in the temperature distribution inside the droplet, as well as the interfacial temperature distribution as two temperature deep-points are found in Figure 4.10b, as encircled with black. In this case, the interfacial temperature decreases with polar angle, as it increases from 20° to about 40° . Moreover, as the polar angle increases from 40° to 90° , the interfacial temperature increases accordingly.

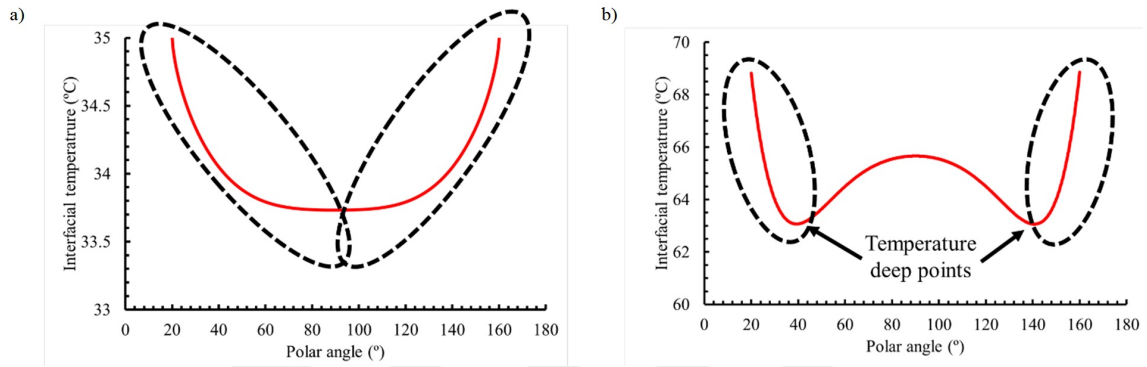


Figure 4.10 Interfacial temperature distribution at the superheat temperatures of a) 15°C b) 50°C

Figure 4.11 shows the evaporative heat and mass flux for superheat temperatures of 15°C and 50°C . As seen, regardless of superheat temperature, in the absence of Marangoni flow, the superheat temperature strongly affects the evaporative heat and mass fluxes. As seen, higher evaporation rate is obtained near the contact line, due to strong Stefan flow. Similar evaporation rates has been also found for spherical droplets [72, 112].

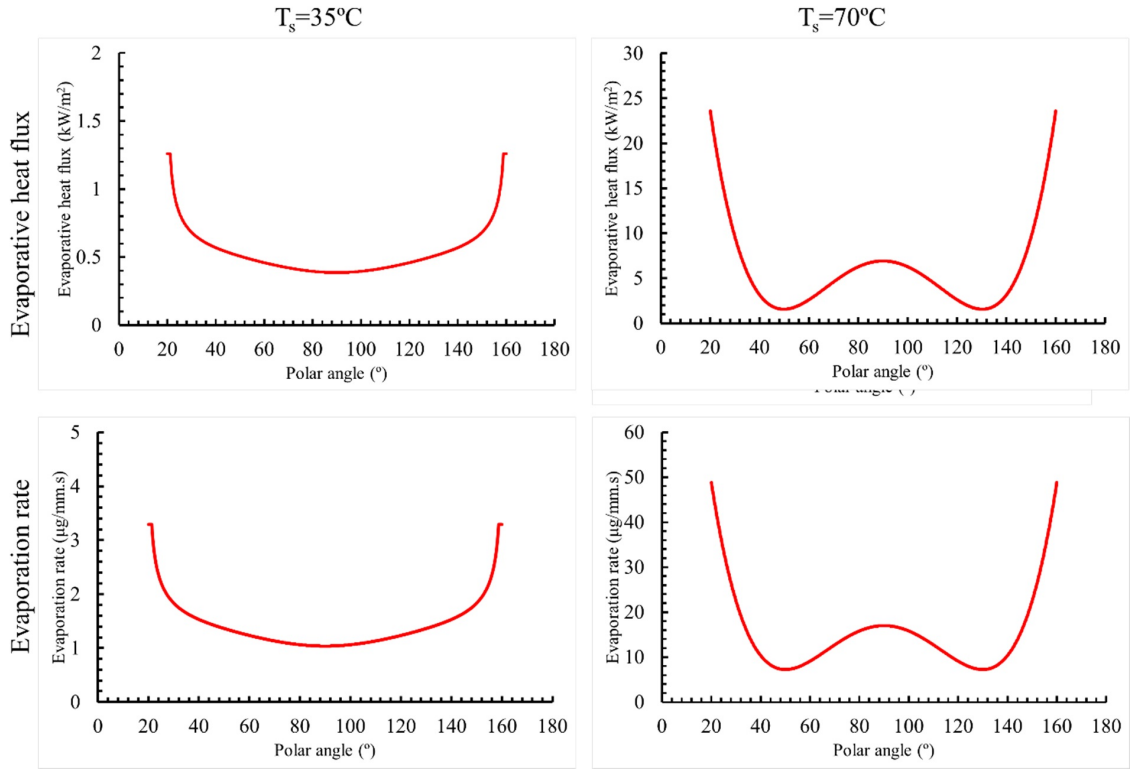


Figure 4.11 Evaporative heat flux and evaporation rate as a function of substrate temperature at the superheat temperatures of a) 15°C b) 50°C

4.1.3 Adjacent cylindrical droplets

As mentioned before, the numerical model, which is validated against the experimental results, is used to perform a study on effect of adjacency on evaporating water droplets. Here, first the effect of diameter on velocity and temperature fields is discussed. Later on, the effect of non-dimensional pitch distance, L/D , is considered. Finally, the effect of droplet diameter and L/D on evaporation rate is covered.

4.1.3.1 Effect of droplet diameter

The velocity and temperature fields within droplets are investigated in the presence and absence of Marangoni flow for different droplet diameters. In the presence of Marangoni flow, regardless of the droplet diameter, strong flow vortices inside the droplets (CD and SD) are observed. As indicated in Figure 4.12, while the

thermocapillary flow is present, the flow direction in the CD is from the contact line to the apex, which is consistent with what has been reported for single spherical droplets [106, 113–116] (see Arrows I in Figure 4.12). Here, it can be seen that unlike two symmetric flow cells in single elongated droplets the internal flow of the SD exhibits two asymmetric circular vortices due to asymmetric natural convection around the droplet (arrows II and III in Figure 4.12). On the neighboring side of the SD, where the CD is present, a large circulation pattern is seen (arrow II in Figure 4.12), while the vacant side possesses a relatively smaller circulation pattern (arrow III in Figure 4.12). It is worthwhile to mention that the interactions between the CW and CCW take place at the polar angles (in Figure 3.1) in the range of 120° to 130° . The obtained results indicate a slight increase in the polar angle of CW and CCW vortices interaction, as the droplet diameter increases. As seen, the minimum temperature point is found at the apex of the CD (in Figure 4.12 arrow IV). This is consistent with the reported results for spherical droplets [72]. However, for the SDs, the minimum temperature is found to happen on the vacant side of the SD, where the glsCW and glsCCW flows interact (arrow V in Figure 4.12 arrow IV). Droplet diameter raises the thermal resistance, which in turn increases the temperature difference between the interface and surface.

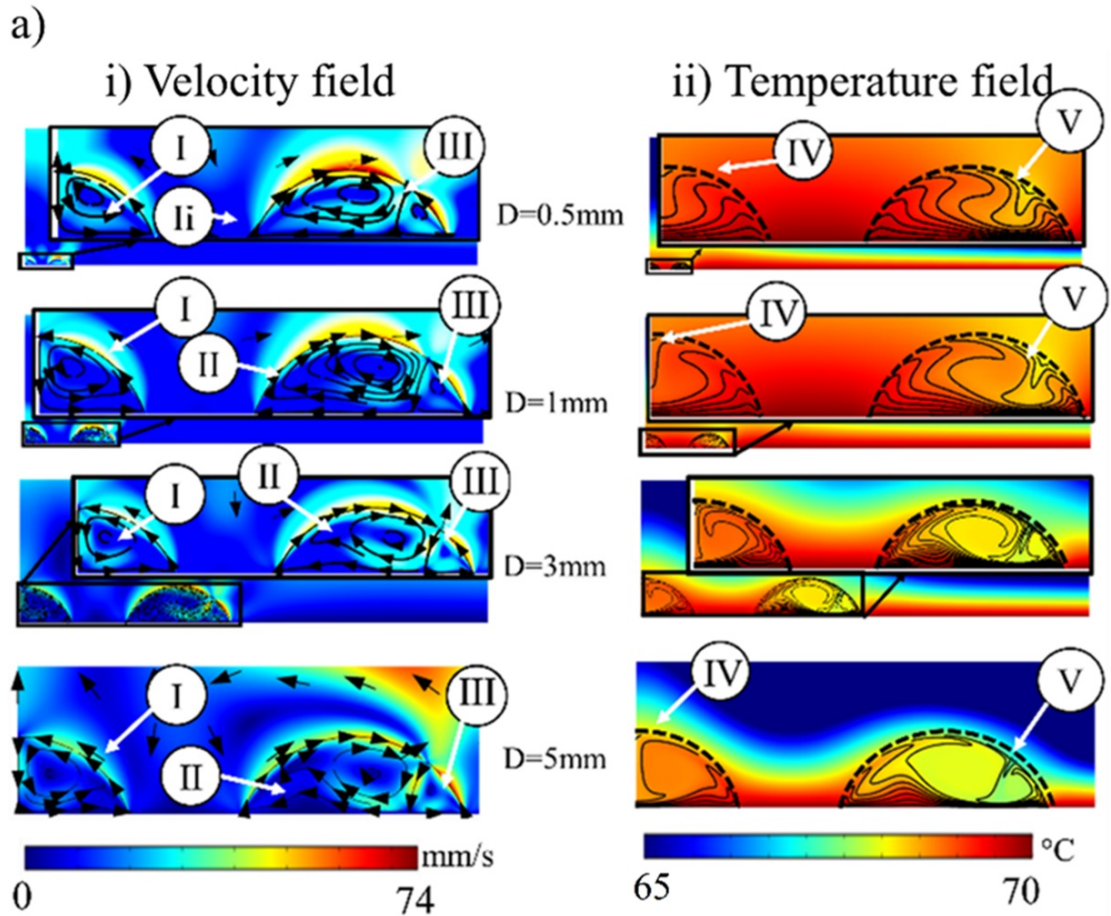


Figure 4.12 Evaporative heat flux and evaporation rate as a function of substrate temperature at the superheat temperatures of a) 15°C b) 50°C

Figure 4.13 shows interfacial temperature distribution in the presence of thermocapillary effect. Generally, the interfacial temperature of both CDs and SDs decreases with an increase in the droplet diameter, which stems from the increase in thermal resistance due to larger footprint. It is worthwhile to state that a sudden decrease in interfacial temperature is observed at the polar angles of interactions between the CW and CCW. This interaction happens at the polar angles of 90° in the CDs, and 120° to 130° in the SDs, where a slight decrease in the polar angle of interaction is observed as the SD diameter increases. Regarding their higher evaporation rate, the SDs have relatively lower interfacial temperature in comparison with their CD counterpart.

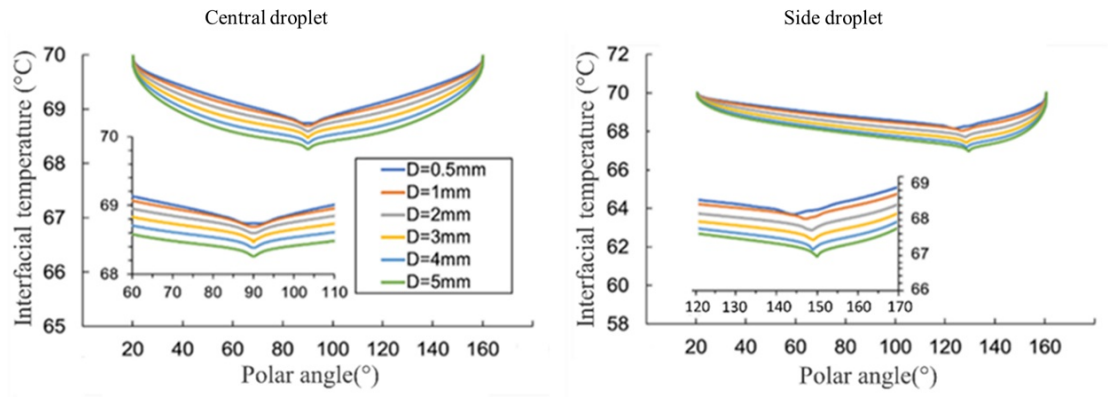


Figure 4.13 Interfacial temperature distribution, in the presence of Marangoni effect of central and side droplets

Figure 4.14 shows the general form of the velocity and temperature fields at the evaporating liquid domain. As seen, inside the CDs, a uniform thermal sub-layer is obtained (shown as region (i), placed under the non-uniformly distributed region). The uniform thermal sub-layer in the SD droplet, possesses a larger uniform sublayer at the neighboring side, since the smaller evaporation rate at the neighboring side results in smaller thermal gradient and velocity magnitude. Moreover, the flows inside the droplet can be divided into four different categories. The upward flow (vector (ii)) flows from the contact line towards the apex of the droplet. This flow is expected to be longer at the neighboring side of SD than the vacant side. Furthermore, from the point of interaction towards the substrate, a flow is obtained (vector (iii)). Moreover, capillary flow is observed, which is near the substrate towards the contact lines (vector (iv)). Moreover, a circulation can be seen inside the mentioned flows (vector (v)).

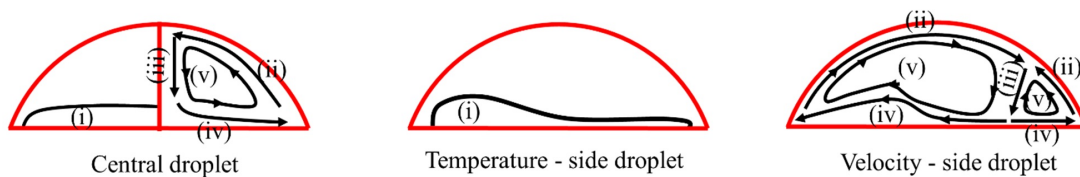


Figure 4.14 Schematic representation of internal circulation and temperature distribution inside the droplets

In the absence of the Marangoni effect, the buoyancy driven flow vortices are greatly dependent on the diameter of the droplet. To characterize the effect of buoyancy driven flow in the liquid domain, the droplet Rayleigh number is defined as follows [117]:

$$Ra = \frac{\beta \rho g \Delta T D^3}{\alpha \mu} \quad (4.1)$$

Here, β , ρ , g , ΔT , D , α , and μ are the thermal expansion coefficient, the density, gravitational acceleration, wall superheat temperature, the droplet diameter, the thermal diffusivity, and the dynamic viscosity, respectively. As can be seen in Figure 4.15, a parabolic streamline from the interface to the contact line (Capillary flow) is obtained (arrow I) for the half-shown CD with $Ra=2 \times 10^2$ ($D = 0.5mm$). More specifically, CDs with $2 \times 10^2 < Ra < 1.3 \times 10^4$ ($0.5mm < D < 2mm$) demonstrate one CW vortex at the inner part of the half of the shown CD droplet (arrow II). This implies that in the absence of the thermocapillary effect, Capillary flow at the interface outweighs the buoyant flow of the CDs at lower droplet Rayleigh numbers ($Ra < 1.3 \times 10^4$). For the CDs having Buoyancy numbers of $Ra \geq 4.3 \times 10^4$ ($D \geq 3mm$) and all four flows introduced for a single droplet, a CCW circulation is visible in the liquid domain (arrow III). Similarly, the available studies in the literature reported a circulation, from the apex to the contact line, for a single spherical droplet, at the absence of thermocapillary effect [72, 111]

In contrast to CDs, the number and direction of flow vortices show more variations with the diameter of SDs. Similar to its CD counterpart, for the SD with a $Ra=2 \times 10^2$ ($D = 0.5mm$), the streamlines are from the interface to the contact line (arrow I). On the other hand, a single circulation (arrow IV) is found for SDs with $1.6 \times 10^3 \leq Ra \leq 1.2 \times 10^4$ ($1mm \leq D \leq 2mm$), which was also reported in previous studies for two spherical droplets placed at close vicinities [63]. However, two vortices with opposite direction (CW and CCW as indicated by arrow V) are evident in the SDs with $Ra \geq 4.3 \times 10^4$ ($D \geq 3mm$). Unlike the CDs, in which two symmetrical circular vortices are located, a larger vortex is evident on the vacant interface of the SD, where a larger evaporation rate is expected (arrow V).

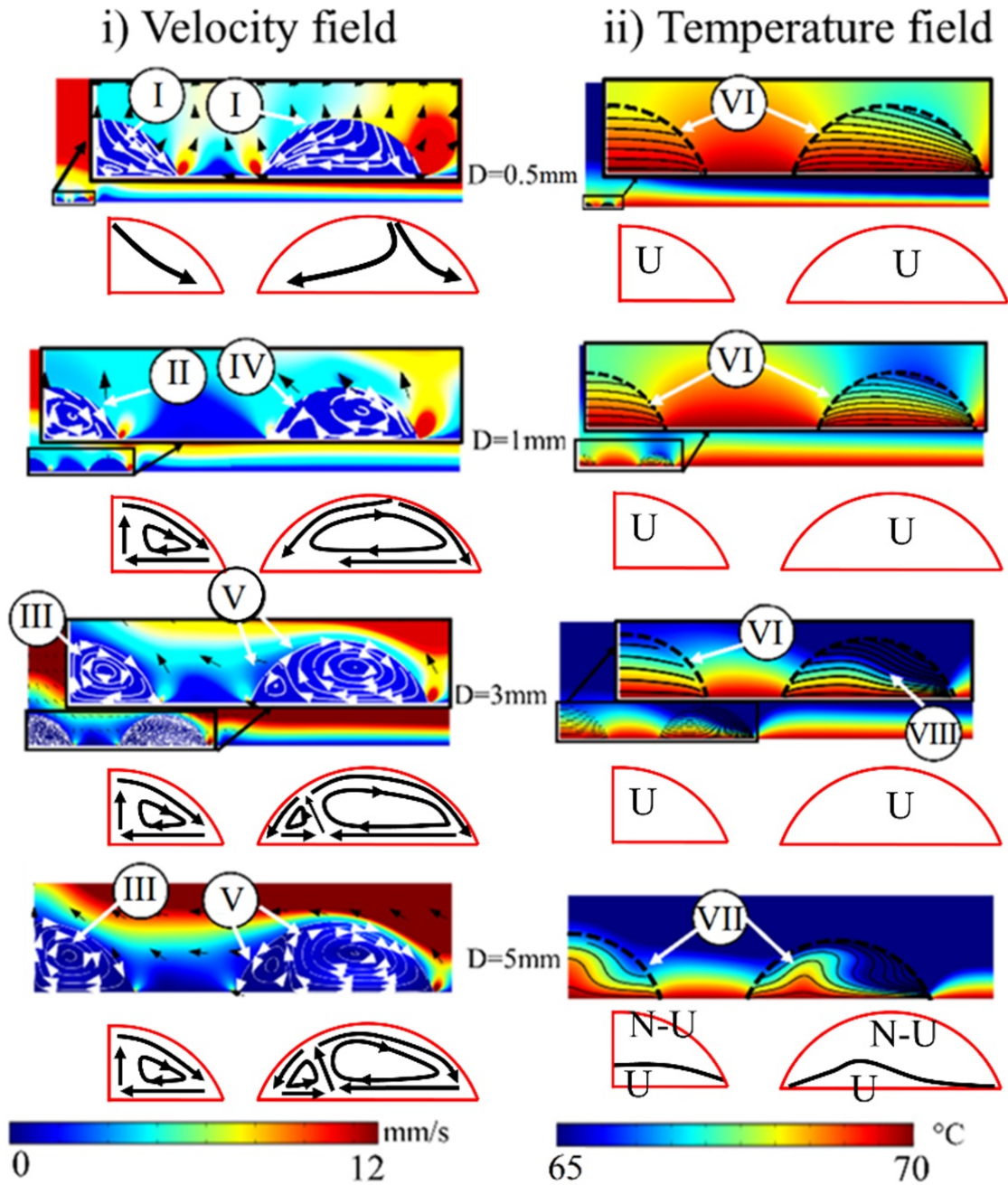


Figure 4.15 The effect of droplet size at $L/D = 0.5$ and wall superheat of 50°C on temperature and velocity fields in the absence of Marangoni effect

The buoyancy driven circulations for the CDs with the Rayleigh of $2 \times 10^2 < Ra \leq 4.3 \times 10^4$ ($0.5\text{mm} < D \leq 3\text{mm}$) are not strong enough to significantly change the internal temperature distribution as shown by parallel isotherms in Figure 4.15 (arrow VI). However, the buoyant flow starts to affect the temperature distribution of CD at a diameter of $D = 4\text{mm}$, from uniform isotherms to non-uniform ones. The non-uniform isotherms indicate that the internal temperature field inside the droplets with $Ra > 1 \times 10^5$ of ($D > 4\text{mm}$) is strongly affected by the buoyant flow (arrow VII in Figure 4.15). The SDs have an asymmetric evaporation rate, and

the temperature counterlines are tilted toward the outer boundaries for the droplets with $Ra \leq 1.2 \times 10^4$ ($D \leq 2mm$) (arrow VI). Here, the buoyant flow is not strong enough to change the temperature field. For the case of $Ra = 4.3 \times 10^4$ ($D = 3mm$), the isotherms in SD begins to distort, which suggests that the buoyancy driven flow starts to affect the uniformity of the temperature field of SD (arrow VIII). For the largest droplet with $Ra = 2 \times 10^5$ (corresponding to $D = 5mm$), the both non-uniform region and uniform thermal sub-layer are found. (arrow VII).

Figure 4.16 shows the effect of droplet diameter on interfacial temperature for CDs and SDs in the absence of thermocapillary effect. As can be seen, the interface temperature drops with droplet diameter, which is due to an increase in the conduction thermal resistance between the surface and the apex, while the buoyant flow is not strong enough to change the uniformity temperature distribution. To elucidate, the interfacial temperature of the CDs with diameters of $D < 4mm$ uniformly decreases from the surface to the apex. At the diameter of $D = 4mm$, a small curvature at the interfacial temperature (indicated by red arrow) implies that buoyancy flow starts to change the temperature distribution at this diameter. While the diameter of the droplet is $D \geq 5mm$, the interfacial temperature is affected by the buoyancy flow, as two dip-points are evident for the interfacial temperature profile. For the case of the SDs, as expected, the non-uniform natural convection results in an asymmetric temperature distribution. The temperature at the interface is relatively smaller than its counterpart droplets. This shows that the heat transfer mechanism is stronger for the SDs. The interfacial temperature distribution in the SDs with diameters of $D \leq 3mm$ is not affected by buoyancy flow, similar to their CD counterparts. Even though its counterpart stays intact, the droplet having the diameter of $D = 4mm$ is significantly influenced by buoyancy driven flow. Finally, temperature distribution on the interface of both CD and SD possessing a diameter of $D = 5mm$ is highly affected.

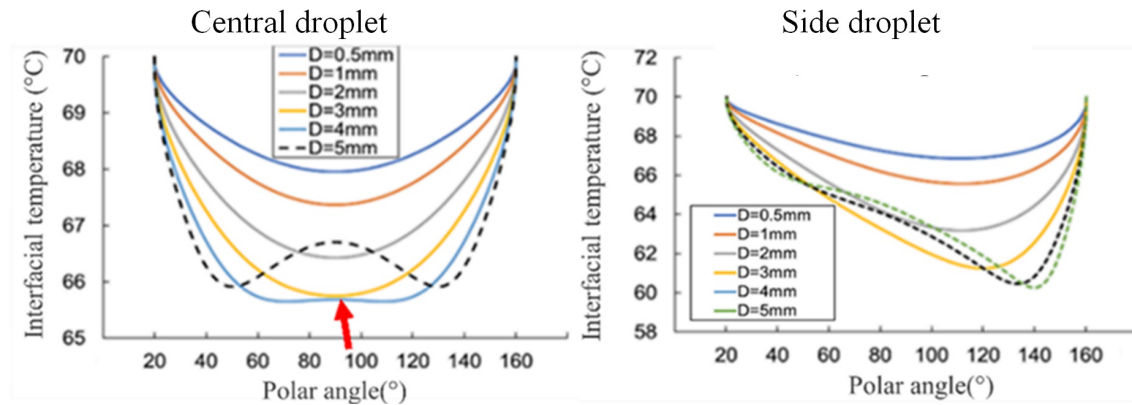


Figure 4.16 The effect of droplet size at $L/D = 0.5$ and wall superheat of 50°C on interfacial temperature distribution in the absence of Marangoni effect

4.1.3.2 Effect of non-dimensional pitch size and wall superheat

Droplet pitch size is a critical parameter that changes the velocity field and resulting temperature distribution. In the presence of thermocapillary flow, similar to what was mentioned previously (Figures 4.12 and 4.13), regardless of the droplet pitch size, two separate circulations are noticed. It should be noted as the pitch size increases, the polar angle of interactions between the CW and CCW circulations decreases. This implies that as the distance between the droplets increases, both CD and SD tend to show a behavior closer to a single droplet. As the distance between droplets increases, the evaporation rate increases and results in a decrease in interfacial temperatures.

Figure 4.17 shows the effect of non-dimensional pitch distance (L/D) on interface temperature for different wall superheat values. Generally, as the distance between the droplets increases, enhancement of evaporation rate results in temperature reduction at the interface of center and side droplets. At low wall superheat values ($\Delta T = 15^\circ C$), which corresponds to low droplet Rayleigh numbers ($Ra \leq 10^5$), buoyant flow does not affect the monotonically changing pattern of interfacial temperature [118]. Moreover, while the interfacial temperature is always symmetrical with respect to the apex in the CD, it becomes asymmetric in the SD by manifesting minimum temperatures at the polar angles ranging from 105° to 110° .

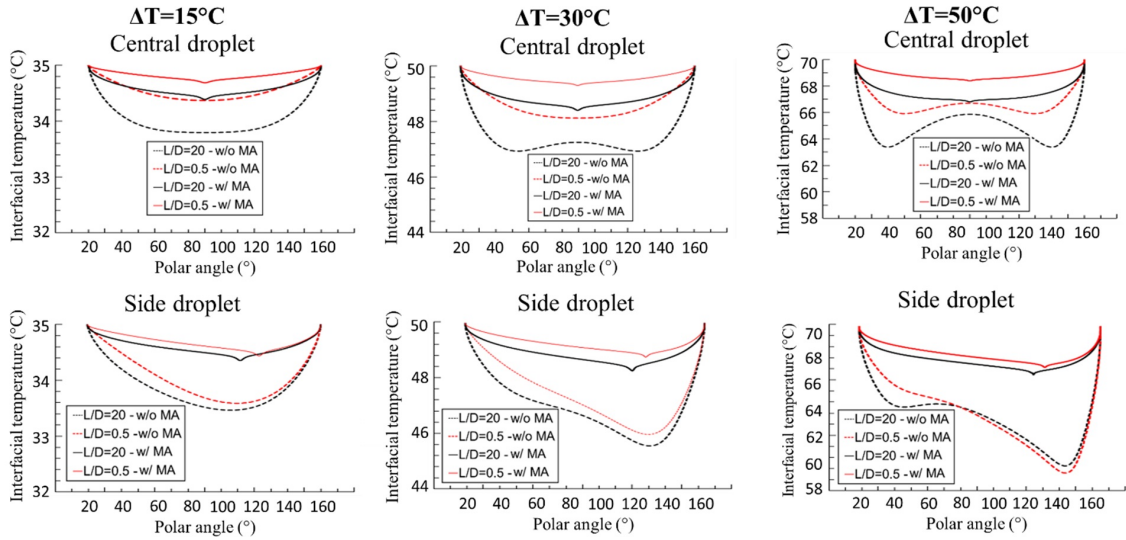


Figure 4.17 Droplet interface temperature at different non-dimensional pitch distance (L/D) and wall superheat (ΔT) for a) side droplet b) center droplet

At a wall superheat value of ($\Delta T = 30^\circ C$) corresponding to ($1 \times 10^5 \leq Ra \leq 2 \times 10^5$), the buoyant flow makes the interfacial temperature exhibit a non-monotonic pattern.

Figure 4.17 indicates that when droplets are close i.e. $L/D = 0.5$, the buoyancy driven flow results in a uniform temperature distribution at the interface CD. As the distance between the droplets increases, due to the higher evaporation rate at the CD, the interface temperature of the CD decreases, and two temperature dips are visible. It can be seen that the SD with a diameter of $D = 5mm$ is affected by the buoyant flow, regardless of the non-dimensional pitch size. The minimum temperature at the SD is located at the polar angle of $\sim 125^\circ$. This implies that even though two vortices exist inside the droplets at $Ra=1.2 \times 10^5$, the neighboring side vortex is not strong enough to cause non-uniformity of temperature distribution (see Figure 4.18).

For wall superheat values ($\Delta T = 50^\circ C$), which correspond to ($Ra \leq 2 \times 10^5$), regardless of the distance between the droplets, the interface temperatures of CD and SD are affected by the buoyant flow. As the distance between the droplets increases, the interface temperature at the left side of the droplet has one dip due to a stronger vortex. The minimum interface temperature at the SD happens at the polar angle of around 140° .

In the absence of thermocapillary flow, the variations in the velocity field are more complicated. Figure 4.18 shows the velocity fields inside the adjacent cylindrical droplets, in the absence of Marangoni effect. As seen, when the distance of the adjacent droplets is small (i.e., $L/D \leq 0.75$), a reduction in evaporation rate on the left side of the SD compared to the vacant side is observed due to the shielding effect. By comparing Figures 4.15 and 4.18 it can be concluded that a single circular circulation is formed inside the droplets when the droplets are relatively close and fall within specific ranges of Rayleigh numbers. To elucidate more, while the dimensionless pitch size is $L/D = 0.1$, a single circulation is observed at Rayleigh numbers lower than $Ra=1.2 \times 10^5$. However, for $L/D \leq 1$, a single circulation vortex is located at Rayleigh numbers of $Ra=6 \times 10^4$. Due to stronger natural convection at the neighboring interfaces, increasing the pitch size or the wall superheat results in the generation of two separate flow vortices at the SDs. The velocity field inside the evaporating droplet as a function of L/D and droplet Rayleigh number provides new insights into the velocity distribution of elongated array of droplets, which could be especially important for a different range of applications including the deposition of colloidal particles dissolved in evaporating droplets [119, 120].

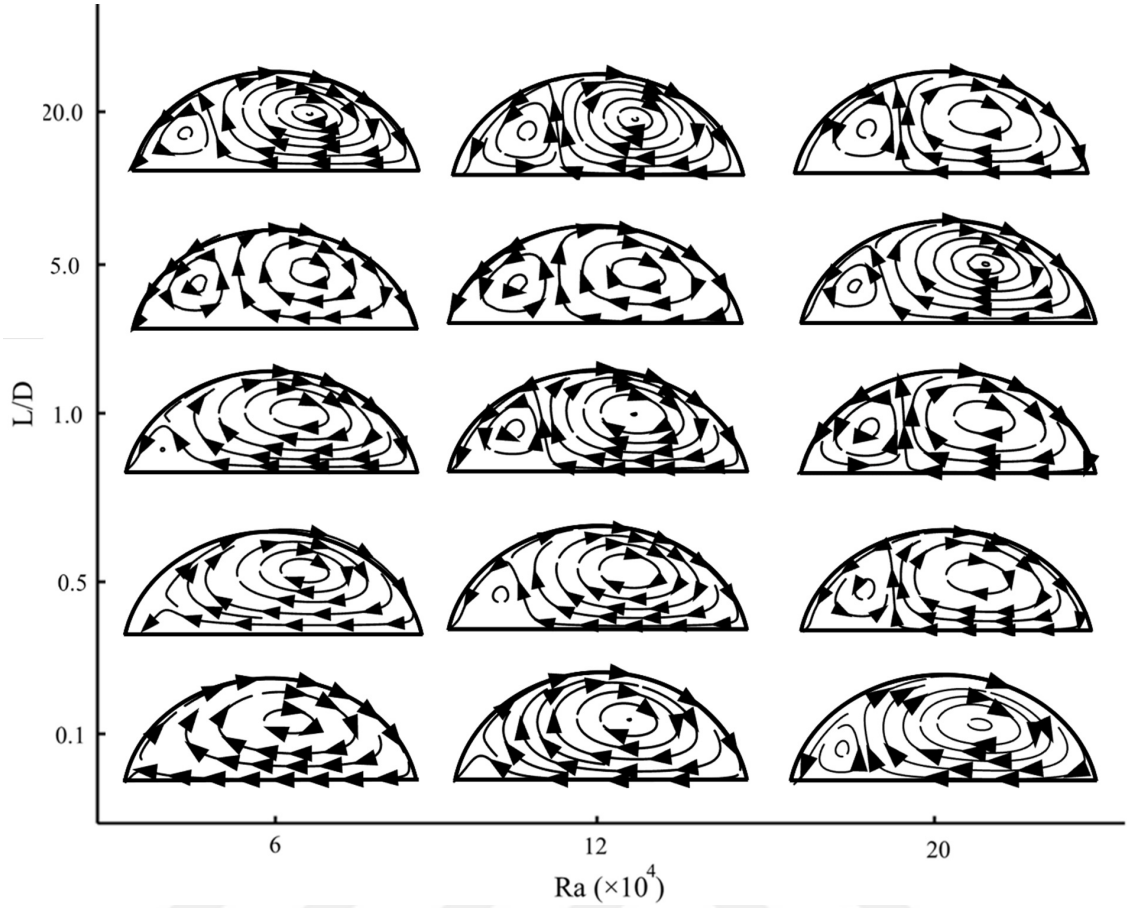


Figure 4.18 Droplet velocity field at different non-dimensional pitch distance (L/D) and Rayleigh numbers (Ra)

4.1.3.3 Interfacial evaporation rate

Vapor field significantly affects the evaporation kinetics [121], which is strongly dependent on the velocity and temperature fields. Figure 4.19 shows the predicted evaporative heat flux for the CD and SD in the presence/absence of the thermo-capillary effect. As reported in the previous studies [72, 121, 122], compared to the upper parts of the droplet, a relatively large evaporative heat flux is predicted at the contact line. As seen in Figure 4.19, a sudden decrease in the heat flux is predicted at the location of the interaction between CW and CCW flows, in both CD and SD droplets, when Marangoni flow is present. Although the general trend of the evaporative heat flux is almost the same for the droplets, the sudden heat flux reduction diminishes with droplet diameter. The obtained results show that in the presence of Marangoni effect, due to the increase in the thermal resistance, the droplet diameter has an inverse effect on the magnitude of evaporative heat flux.

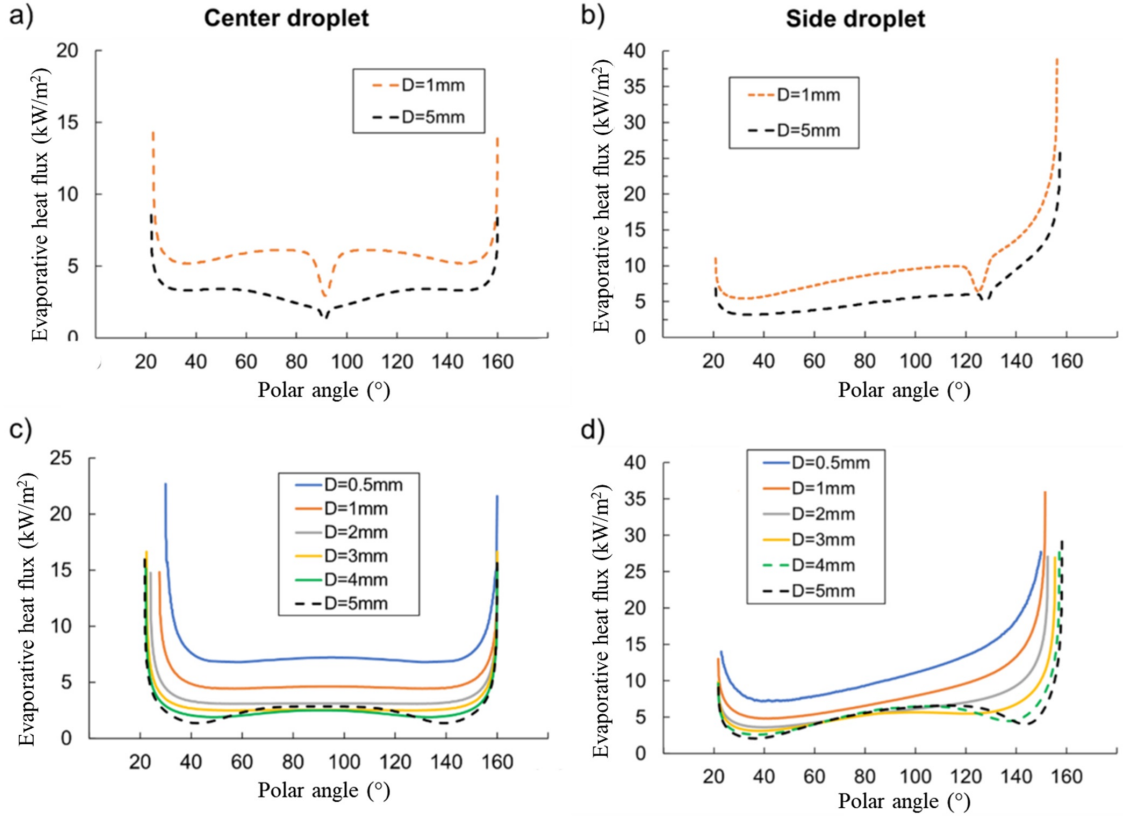


Figure 4.19 Interfacial heat flux a-b) in the presence of Marangoni flow c-d) in the absence of Marangoni flow ($L/D = 0.5$ and $T_s = 70\text{°C}$)

As mentioned before, for central droplets having $D < 4\text{mm}$ and side droplets having $D < 3\text{mm}$, the buoyant flow is not strong enough to change the temperature distribution at the interface. In these cases, due to the increase in the thermal resistance, the evaporative heat flux decreases with the droplet diameter. However, the evaporation rate of the central droplet having $D = 5\text{mm}$ exceeds the ones having diameters of $D = 3\text{mm}$ and $D = 4\text{mm}$. Similarly, for the side droplets, the evaporative heat fluxes of the droplet having $D = 4$ and $D = 5\text{mm}$ are larger than those having $D = 3\text{mm}$. It should be noted that due to the shielding effect, the evaporative heat fluxes on side droplets at the polar angle of 20° are larger than the other side of the side droplet regardless of the presence or absence of Marangoni flow. Similar results were also reported in the literature [65]. Our study for the first time demonstrates the distributed heat flux at the interface of the adjacent cylindrical droplet.

Figure 4.20 shows the effect of the wall temperature superheat (ΔT) and non-dimensional pitch size (L/D) on evaporation rates in the presence and absence of Marangoni flow. The evaporation rate of both droplets (SD and CD) increases with the droplet pitch size, which is due to a weakening of the shielding effect with distance. Furthermore, the presence of the Marangoni flow enhances the evaporation

rate compared to the buoyancy-driven flow. As indicated in Figure 4.20, at a wall superheat of ($\Delta T = 15^\circ C$), the evaporation rate of the side droplet (SD) is larger than the central droplet (CD), which is in parallel with the reported results in the literature [64, 65, 123]. It should be noted that as the pitch distance increases, the evaporative mass flux of both CD and SD tends to a single droplet. A wall superheat of ($\Delta T = 50^\circ C$), at the absence of Marangoni effect, evaporation rate of the SD is larger than the CD one. Moreover, as the L/D ratio increases to more than 5 ($L/D > 5$), the SD shows an evaporation rate larger than a single droplet, due to strong natural convection, as it has been reported for a spherical droplet before [66]. However, the presence of the Marangoni effect leads to a larger evaporation rate of the CD compared to the SD for $L/D > 5$.

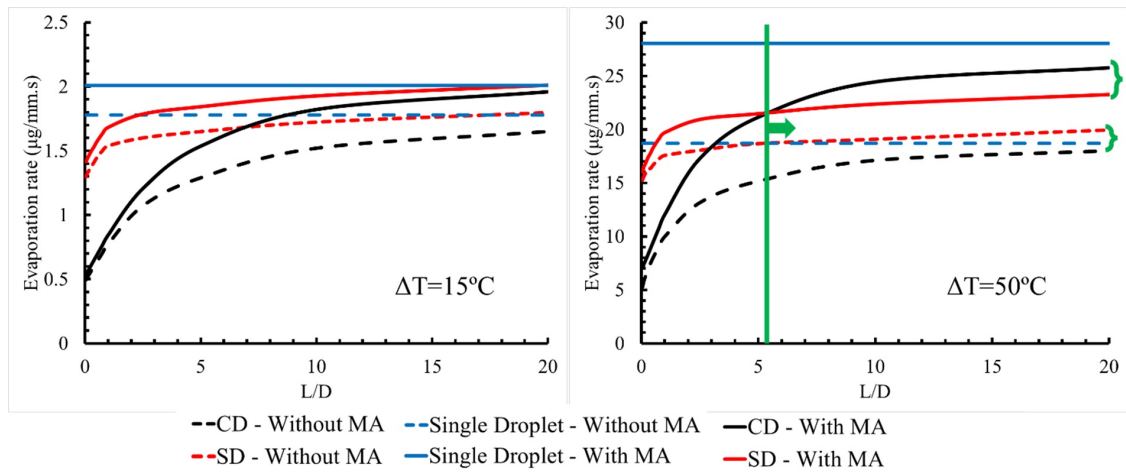


Figure 4.20 Effect of non-dimensional pitch L/D and wall superheat on the evaporation rate in the absence and presence of Marangoni flow at a) ($\Delta T = 15^\circ C$); and b) ($\Delta T = 50^\circ C$)

The lower evaporation rate at the SD may be attributed to the droplet shape. While previous studies used spherical droplets, cylindrical shaped droplets are considered in this study (as illustrated in Figure 4.21). For a spherical droplet, the fresh gas is always provided to the back surface (see the streamlines on the spherical droplet). However, the interface of the SDs in elongated cylindrical droplet is divided into two separate parts: (I) the front surface, which is directly encountered by the gas due to natural convection, and (II) the back interface. At the back interface, where the vapor is driven towards the central droplet, the concentration field is stretched, which lowers the gradient of the concentration field and consequently decreases the evaporation rate at the back interface of the SD. In other words, due to asymmetric natural convection around the SD droplet, the evaporation rate at the back surface of the SD droplet is diminished, which results in a smaller evaporation rate with respect to the central one. But due to the symmetrical geometry of the central

droplet, the evaporation rate is high enough on both interfaces.

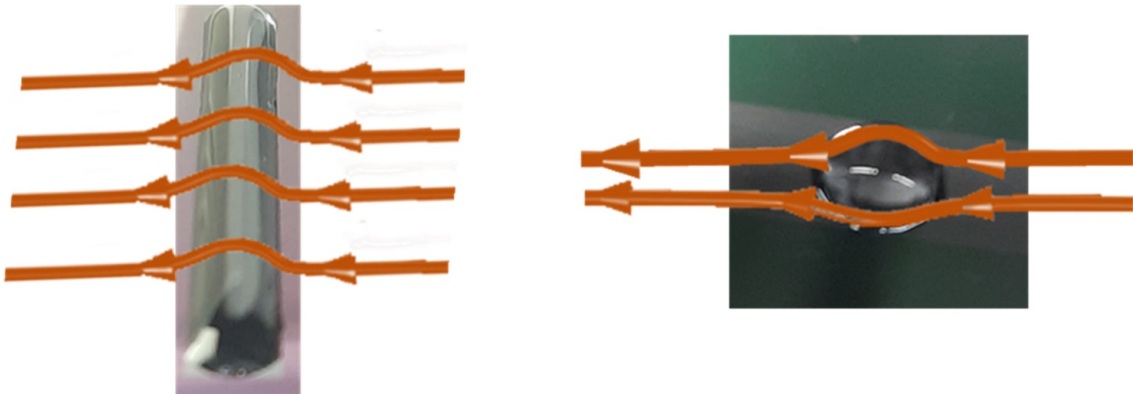


Figure 4.21 Comparison between cylindrical and spherical droplets

Three other co-existed conditions cause a larger evaporation rate in the CD compared to the SD: i) presence of the Marangoni effect, ii) high value of pitch distance, and iii) high temperature difference. In the absence of Marangoni effect, as seen in Figure 4.22a, the Stefan flow, which is normal to the interface, surpasses the tangential velocity. At the backside of the SD, the direction of the Stefan flow is in the same direction as natural convection, which prevents the generation of vortices at the back interface. However, since the direction of the Marangoni flow opposes natural convection, their interaction results in stronger vortices at the back of the SD (see Figure 4.22a). These vortices result in the accumulation of the vapor at the back of the droplet, which diminishes evaporation. Moreover, while the droplets are relatively close, the vortices not only affect the neighboring interface of the SD, but also diminish the evaporation rate at the CD. However, when the pitch distance increases, due to the viscous forces, the vortices generated by the SD are dissipated and do not affect the CD (see Figure 4.22b). Lastly, the higher superheat temperature of the surface results in a stronger natural convection around the droplet. This stronger natural convection leads to an easier vortex generation around SD.

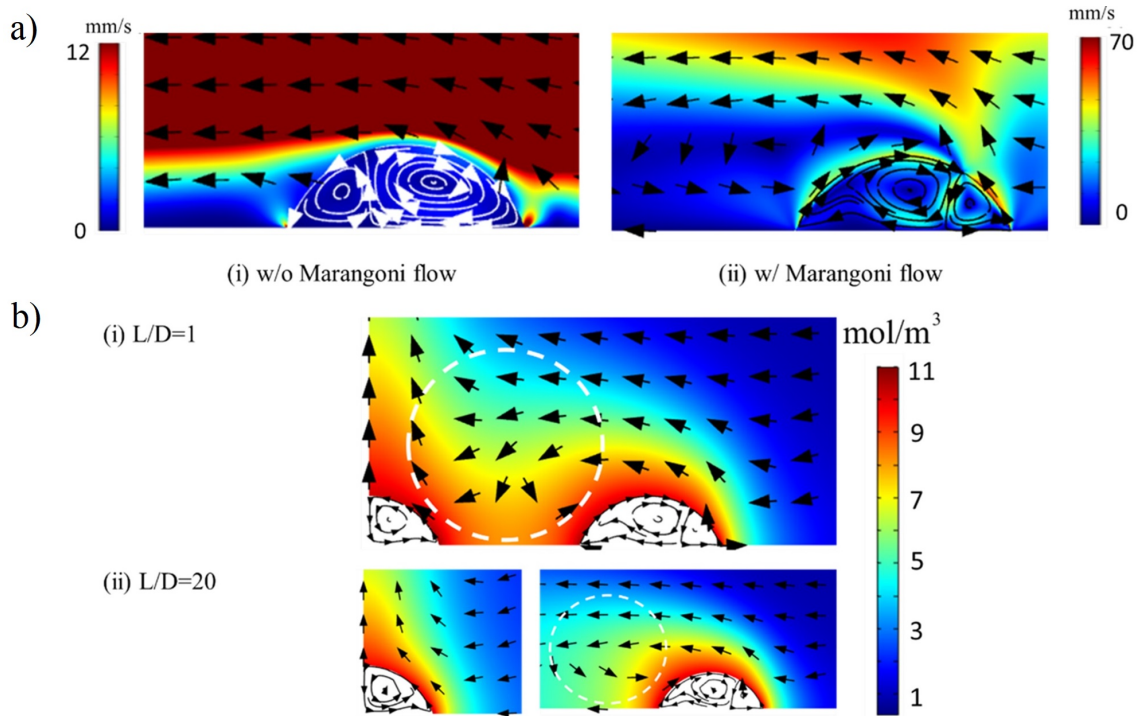


Figure 4.22 a) Velocity field in the gas phase around the SD(i) without Marangoni (ii) with Marangoni flow b) Vapor concentration field at (i). $L/D = 1$ and (ii) $L/D = 20$

The obtained results shown in Figures 4.20, 4.21, and 4.22 for the first time reveal that for $L/D > 5$ the evaporation rate of the CD becomes larger than the SD in an array of cylindrical droplets at high substrate temperatures and in the presence of Marangoni flow. This finding is especially useful for applications where droplet arrangement has a vital role on the system performance, such as uniformly cooling applications. Therefore, the non-dimensional pitch number could offer a guideline for researchers. This study provides fundamental insight into understanding of the physics of spherical and non-spherical droplet evaporation.

4.2 Flow boiling

In this section, the obtained results from the flow boiling experiments, which cover both heat transfer and visualization results, are presented. In the experiments, the applied heat flux ranged from $2\text{W}/\text{cm}^2$ and $16\text{W}/\text{cm}^2$. Moreover, two different mass fluxes of $90\text{ kg}/\text{m}^2\text{s}$ and $130\text{ kg}/\text{m}^2\text{s}$ were considered. The obtained HTC's along with the boiling curves are included. Later on, the visualization results are discussed and

compared with the obtained results from a previous study, where water was used as the working fluid [13].

4.2.1 Heat transfer results

As shown in Figure 4.23 at a mass flux of the $90\text{kg/m}^2\text{s}$, both biphilic surfaces show a better performance compared with the entirely uniform hydrophobic surface in terms of boiling HTC. At the first half of the channel, the obtained results suggest that at heat fluxes lower than 5W/cm^2 the biphilic surfaces have no significant influence compared to their hydrophobic counterpart. This result stems from the reason that at the mentioned heat fluxes boiling does not ensue. As can be inferred from the boiling curves (Figure 4.23) for heat fluxes lower than 5W/cm^2 , the wall superheats obtained for different surfaces are close to each other. However, as the heat flux increases from 5W/cm^2 to 12W/cm^2 , the biphilic surfaces yields higher HTCs compared to the hydrophobic surface. The higher HTC is due to nucleation sites provided by the hydrophobic islands. Sisman et al. [124] showed that an increase in density of nucleation sites could decrease HTC. They concluded that close nucleation sites might result in sudden coalescence of bubbles. The sudden coalescence, in turn, results in extending the thermal boundary layer of the bubble beyond the stability limit. Therefore, the corresponding nucleation site is canceled, and a temporal condensation might occur inside the bubble. The hydrophobic islands are not relatively close in this study to result in cancelations of the nucleation sites. Moreover, it should be noted that surface2, due to the biphilicity at the entrance region, exhibits a slightly better performance than surface1. At the heat fluxes higher than the 12W/cm^2 , all surfaces have HTCs close to each other. Regarding the subcooling of the working fluid at the inlet part along with the high temperature of the surfaces under this condition, all the surfaces provide almost the same numbers of nucleation sites, which result in HTCs close to each other.

Similar to the first half, biphilic surfaces have better performances compared to the hydrophobic surface at the second half of the channel (Figure 4.23). At heat fluxes lower than 9W/cm^2 , the average HTCs for the biphilic surfaces are significantly higher than the hydrophobic surface. As mentioned before, along the first half of the channel, at heat fluxes lower than 5W/cm^2 , the performances of all surfaces are similar. However, at the second half, considering that the subcooled fluid mainly reaches the saturation temperature during the first half of the channel along with the nucleation points provided by the hydrophobic islands, higher HTCs are obtained.

Moreover, as the heat flux is raised to values higher than $9\text{W}/\text{cm}^2$, due to partial dry out of the surfaces, all surfaces exhibit similar behavior. The wall superheats on surface2 is lower than surface1 at the applied heat flux of $14\text{W}/\text{cm}^2$, while they correspond to similar HTC's at lower heat fluxes. The presence of biphilic islands at the region1 of surface1 delay the dryout condition at high heat fluxes. At the mentioned mass flux, the maximum enhancement was more than 50% compared to the hydrophobic surface and was reached at the heat flux of $4\text{W}/\text{cm}^2$.

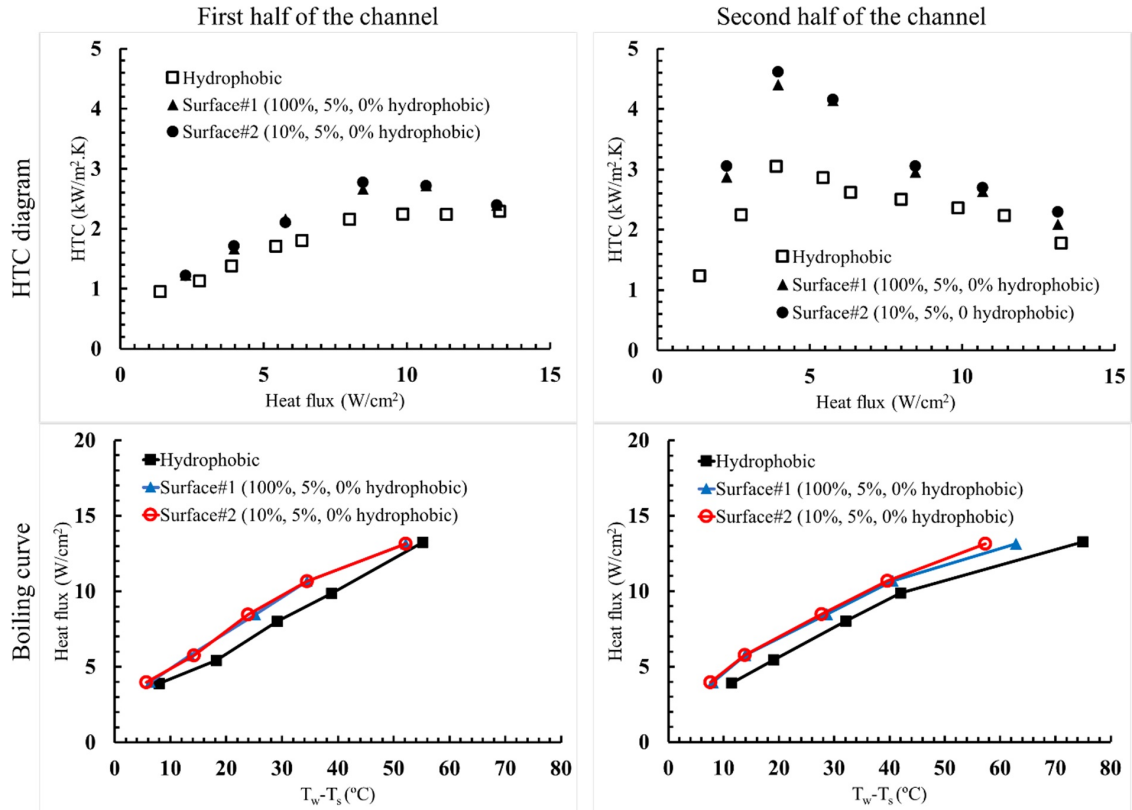


Figure 4.23 Heat transfer coefficients (HTCs) and boiling curves corresponding to the mass flux of $90\text{kg}/\text{m}^2\text{s}$

The results regarding HTCs at the mass flux of $130\text{kg}/\text{m}^2\text{s}$ are displayed in Figure 4.24. At the first half of the channel, as the boiling is not initiated at low heat fluxes, the biphilic surfaces lead to the almost same heat transfer coefficients compared to their hydrophobic counterpart, as they have almost the same wall superheats. This trend is the same for the previously mentioned mass flux for heat fluxes lower than $5\text{W}/\text{cm}^2$. Lie et al [125] reported that the required heat flux for the onset of nucleation increases with the mass flux. This phenomenon explains the delay in the transition of the dominant heat transfer mechanism from single-phase to phase-change, as the mass flux increases. At heat fluxes higher than $9\text{W}/\text{cm}^2$, since the nucleation points are visible on the hydrophobic islands, biphilic surfaces have a better performance than the wholly hydrophobic surface. As shown in boiling curves

of Figure 4.24, the wall superheats obtained for surface2 are smaller than surface1, which implies that the hydrophobic islands at the entrance region of surface2 lead to a slight difference in heat transfer.

In contrast to the mass flux of $90\text{kg/m}^2\text{s}$, where the phase-change heat transfer was dominant for all the heat fluxes at the second half of the channel, at the heat fluxes lower than 4W/cm^2 , single-phase heat transfer is the dominant heat transfer mechanism since boiling does not incept at these heat fluxes along the channel, and as depicted, the wall superheats are close to each other, and all the surfaces exhibit similar HTC at heat fluxes lower than 4W/cm^2 . However, as the heat flux increases, the HTCs of the biphilic surfaces strongly deviate from the hydrophobic surface. It should be noted that the tested surfaces have a maximum enhancement of 26% with respect to the hydrophobic surface, which happens at the heat flux of 9W/cm^2 .

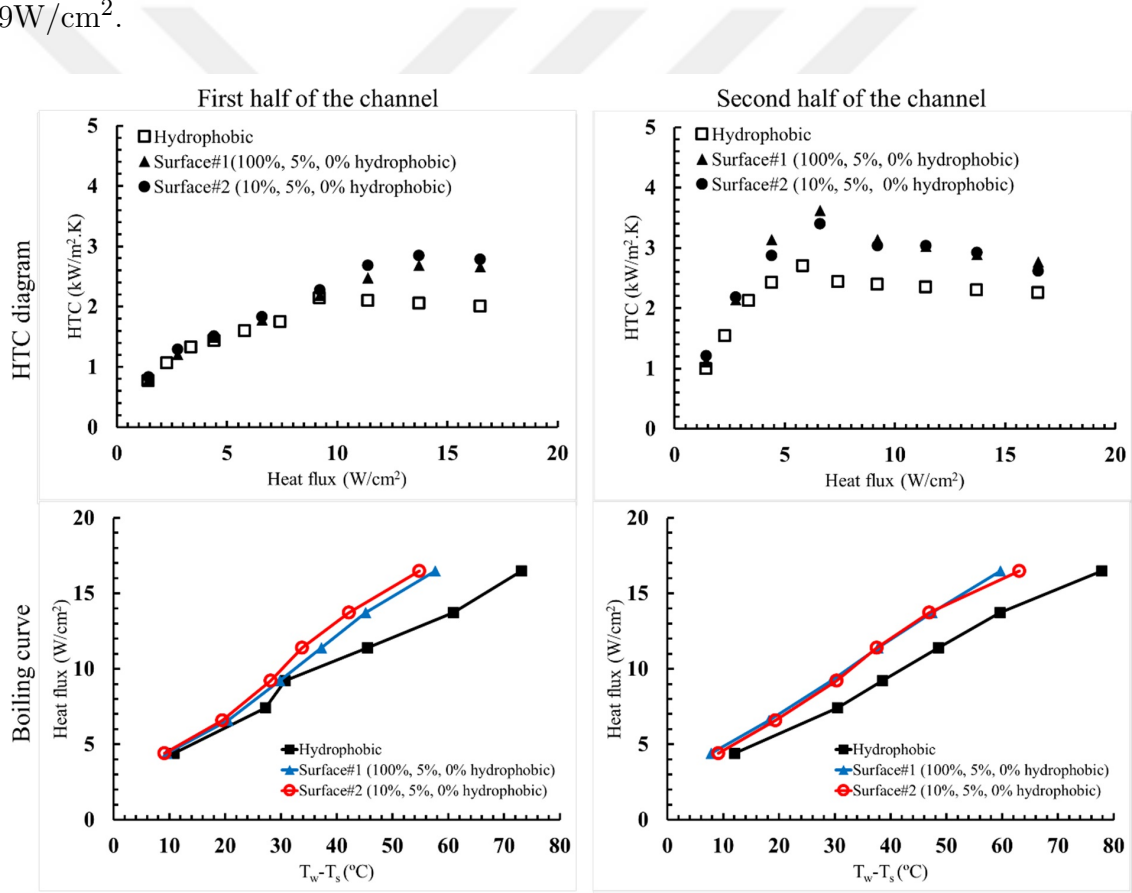


Figure 4.24 Heat transfer coefficients (HTCs) and boiling curves corresponding to the mass flux of $130\text{kg/m}^2\text{s}$

4.2.2 Bubble dynamics results

The results regarding the visualization are presented in Figure 4.25, for the mass flux of $90\text{kg/m}^2\text{s}$. As seen in Figure 4.25, the surface conditions strongly affect the bubble dynamics inside the channel. At the heat flux of 5W/cm^2 , at the first half of the channel, the hydrophobic surface and surface1 have almost single-phase flow conditions. However, the hydrophobic islands on the entrance region of surface2 result in the generation of bubbles, since the hydrophobic islands provide active nucleation sites. According to the heat transfer results in Figure 4.23, these nucleation points are not capable of increasing the HTC noticeably. At the second half of the channel, however, the generated bubbles strongly affect HTC. As seen in Figure 4.25, on the totally hydrophobic surface, the coalescence of the bubbles results in larger bubbles, and transition from bubbly flow regime to slug-flow (heat flux of 7W/cm^2). However, on both biphilic surfaces, slug flow cannot be observed.

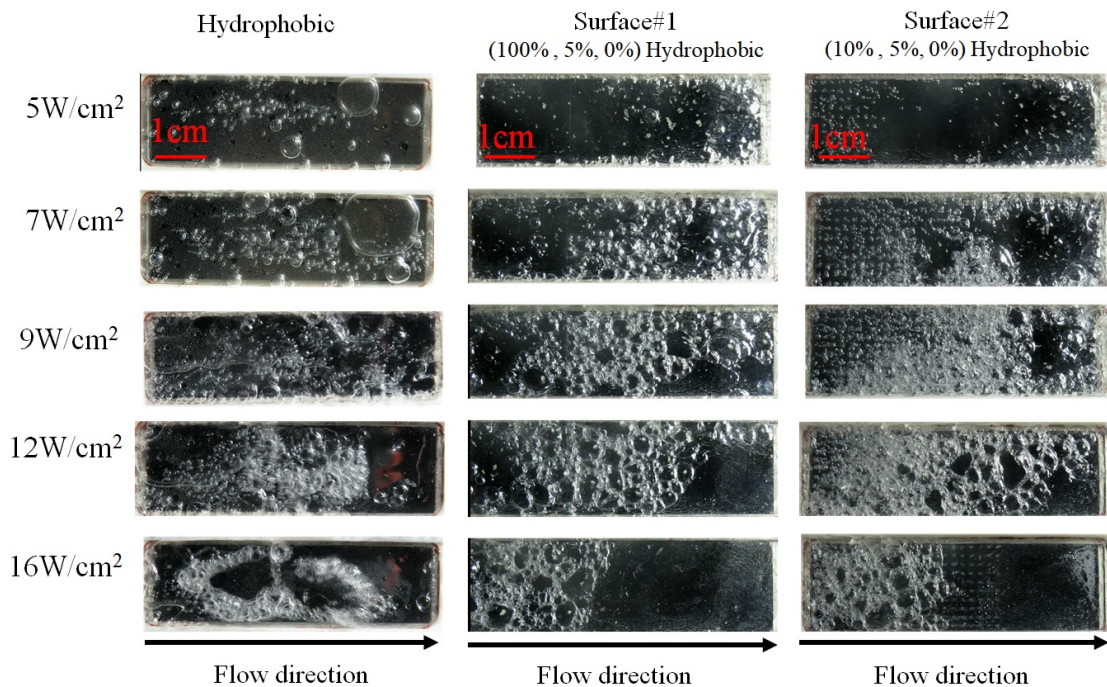


Figure 4.25 Visualization results regarding mass flux of $90\text{kg/m}^2\text{s}$

In our previous study [13], we reported that one of the reasons for HTC enhancement in the biphilic surfaces could be due to bubble break-up during the slug-flow regime, rather than their coalescence. The obtained results of this study are in agreement with the previous study. As shown in Figure 4.26, the coalescence of small bubbles on the hydrophobic surface results in an elongated bubble. However, on the biphilic surface, where the hydrophobic islands provide potential nucleation points, the generated bubbles are relatively close. Moreover, the bubbles are generated on previously designed islands and are well dispersed. These generated bubbles in turn block the effective cross-sectional area, and the velocity of the working fluid will

be higher at the remaining cross-section area (shown by red arrows in Figure 4.26) The higher velocity gradient results in a higher shear force applied to the bubbles. Considering that the bubbles remain intact as long as the shear force is smaller than its surface tensional counterpart, the higher shear force results in break-up of the bubbles on biphilic surfaces and prevents effective coalescence of the bubbles. It should be noted that in our previous study, water was used as the working fluid and the slug flow regime was observed on both hydrophobic and biphilic surfaces. However, since the surface tension of FC-72 fluid is much smaller than water and there exists a larger distance between nucleation sites, the bubbles tend to break up on biphilic surfaces easier than the bubbles in the case of water.

At higher heat fluxes ($q > 9W/cm^2$), both surface1 and surface2 provide larger number of nucleation sites than the totally hydrophobic surface. Compared to surface1, the larger amount of designated nucleation sites at the inlet part of surface2 increases the number of generated bubbles. As can be seen in Figure 4.23, this results in a slightly better performance of surface2 with respect to surface1.

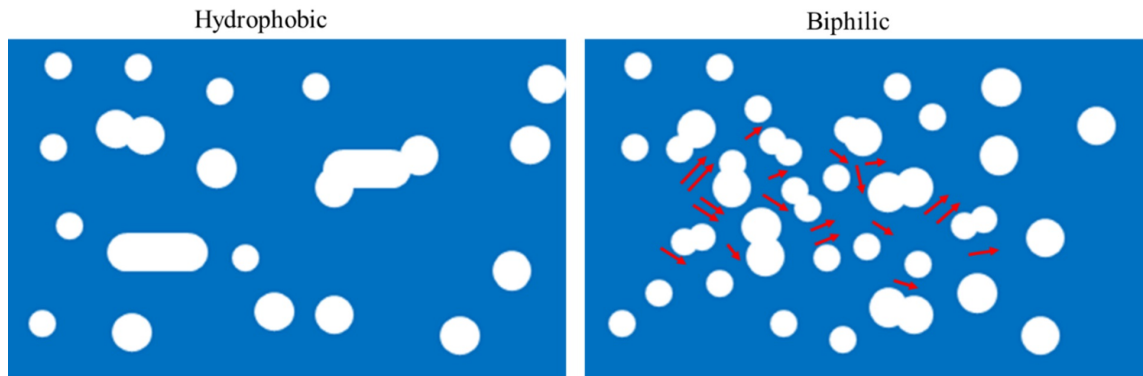


Figure 4.26 Comparison of bubble dynamics on the hydrophobic surface with a biphilic surface

Figure 4.27 shows the comparison of flow patterns of FC-72 with water. In both the present and previous studies [13], since the subcooled liquid is supplied to the channel, boiling does not incept at the first region (Region I). In region II, which is known as the bubbly flow region, the density of the generated bubbles is larger for FC-72 flow compared to water [13]. This is due to two main reasons. First, the contact angles on the islands fabricated in this study are larger than the previous one (110° vs 90°). Second, the latent heat of vaporization of FC-72 is smaller than water, and a larger amount of vapor is generated and observed at a fixed heat flux in the present study. Moreover, it should be noted that since FC-72 has a higher density and a smaller surface tension in comparison with water, a larger drag force and a smaller surface tension force are present. Therefore, the generated

bubbles in FC-72 detach within a shorter time with respect to water. In other words, the frequency of bubble generation in FC-72 is smaller than that in water. Regarding these differences, the duration of bubbly flow regime in FC-72 is extended in comparison with water.

Region III represents the slug flow regime. Considering that break-up of a bubble occurs whenever the applied shear force becomes larger than its surface tension counterpart, the size of elongated bubbles generated from FC-72 is relatively smaller than bubbles generated from water vapor, due to the smaller surface tension of FC-72 compared with water. Moreover, slug flow in water is the dominant flow pattern in water, while bubbly flow is the dominant flow regime in FC-72. In region IV (known as churn flow regime), generally, the middle of the channel is blocked by the vapor core. Similar to slug flow regime, the lower surface tension of FC-72 results in a smaller vapor core in comparison with water. It should be noted that in churn flow regime, the density of the liquid core in FC-72 is higher than water, since FC-72 is more wettable than water.

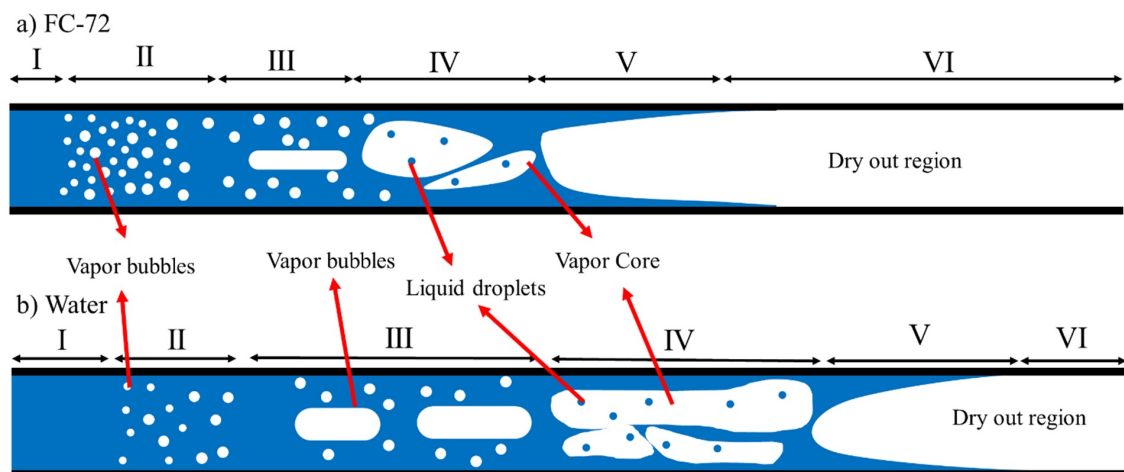


Figure 4.27 Different flow boiling patterns in a)FC-72 medium and b)water medium

5. CONCLUSION

This chapter is dedicated to main results obtained from the numerical and experimental studies. In this regard, first the main findings acquired for droplet evaporation are presented. Afterwards, the major conclusions of the flow boiling results are discussed. Finally, some

5.1 Droplet evaporation

In this thesis, an experimental study was performed on the effect of mixed wettability on evaporation dynamics of water droplet. The substrates consisted of SiO_2 and Al_2O_3 , where SiO_2 presents the hydrophilic islands, and the Al_2O_3 is the less hydrophilic area. The shape of the islands were square, rhombic, and circular. Moreover, the size of the tested samples were one time, one-fourth, and one-sixteenth times of the droplet diameter. The main results are as follows:

- Square shaped islands were not promising for heat transfer enhancement. However, circular and rhombic islands could result in an increase in the evaporation rate. Moreover, the circular shaped islands show better performance than rhombic islands.
- The size of the islands strongly affect the change in evaporation rate, as the smaller islands show better performance than their larger counterparts.
- Increase in evaporation rate occurs in two perspectives: evolution of TCL and split of droplet into smaller droplets.

Moreover, a combined numerical and experimental study was performed to study the dynamics of evaporating single and multiple cylindrical droplets and to investigate the effect of droplet adjacency on the evaporation of an array of cylindrical droplets.

After code validation, a systematic study was performed on the evaporation dynamics of arrays of the non-spherical droplets by taking the effects of droplet adjacency, droplet size, and wall superheat into account. Using the non-dimensional pitch number of L/D (droplet distance to diameter ratio), we present a detailed comparative study of droplet evaporation on the dual effect of gas-side natural convection and the droplet-side Marangoni/buoyancy-driven flow. The major conclusions are as follows:

- The elongated droplet evaporates while the contact length is almost fixed until the volume reaches to a receding contact angle. Later on, the droplet shrinks from one side and ends up to the other side. The numerical results shows that buoyant flow affects the temperature distribution at superheat temperature of 50° , but the uniformity of temperature distribution remains intact at superheat temperature of 15° .
- As the L/D ratio increases, both central and adjacent droplets tend to show a behavior similar to a single droplet. However, at high superheat temperature ($\Delta T > 30^\circ C$), only the central droplet behaves like a single droplet, while the side droplets possess strongly asymmetrical velocity and temperature fields.
- Even though the central droplet has two separate circulations at the absence of Marangoni flow, the side droplet may have a single circulation inside, based on the droplet Rayleigh number and L/D ratio. At $Ra=6\times 10^4$ the single circulation is observed at the $L/D \leq 1$, while at the $Ra=1.2\times 10^5$ the single circulation is observed at $L/D < 0.1$. The $Ra \geq 2\times 10^5$, regardless of the L/D ratio, two circulations are located.
- In the absence of Marangoni flow, the outermost droplet has a higher evaporation rate than the central one. However, in the presence of Marangoni flow, when the non-dimensional pitch size is larger than 5 ($L/D > 5$), there are two possible scenarios as:
 - at low superheat temperatures ($\Delta T < 30^\circ C$), the outer droplet has an evaporation rate higher than the central one
 - at high superheat temperatures ($\Delta T > 30^\circ C$ which corresponds to high droplet Rayleigh numbers), the evaporation rate of the outer droplet is lower than the central droplet.

5.2 Flow boiling

This study investigates the effect of surface mixed wettability on flow boiling of FC-72 in a rectangular minichannel. The surfaces, including two biphilic surfaces and one hydrophobic surface, were fabricated and tested at the mass fluxes of $90\text{kg/m}^2\text{s}$ and $130\text{kg/m}^2\text{s}$ and heat fluxes ranging from 1W/cm^2 to 16W/cm^2 . The main conclusions driven are as follows:

- Surface mixed wettability is an effective method for BHT enhancement especially effective for coolants with smaller surface tension and latent heat of vaporization. The effect of biphilicity on such coolants are more dominant at the second half of the channel.
- The main mechanisms in heat transfer enhancement with FC-72 are the uniform distribution of nucleation sites on the superheated surface and the bubble break-up in the channel. Biphilic surfaces could provide enhancements in flow boiling heat transfer up to 50% compared to the wholly hydrophobic surface.
- The surface with hydrophobic islands at the inlet region of the channel shows slightly better performance in terms of HTC compared to the surface with a hydrophobic entrance.
- The obtained results of this study prove that the biphilic surfaces are promising candidates of modified surfaces in high heat flux cooling with flow boiling.

6. FUTURE RESEARCH DIRECTION

This thesis provides insight to droplet evaporation and flow boiling on mixed wettability surfaces on heat transfer enhancement. However, some aspects of the obtained results could be more analysed, in order to obtain a better efficiency.

First, as mentioned before, TCL of the droplet evolves during the evaporation. In order to obtain better results, another study could be performed on the effect of biphilicity on TCL evolution.

Second, the experimental results showed that droplets could split on biphilic surfaces. A study could be performed on split dynamics of evaporating droplets, since the results in literature are quite rare. Moreover, a simulation could be also conducted in **Surface Evolver**.

Moreover, the obtained results of flow boiling showed that biphilic surface are potential of enhancing the HTCs. Moreover, surface roughness can also enhance the heat dissipation rate. A study could be performed which considers the both effects at the same time.

Finally, the proposed algorithm provides a quasi-steady state simulation. However, this algorithm can also be used for a time dependent simulation of droplet evaporation. In doing so, the proposed algorithm can be extended and after obtaining the convergence in the proposed part, new geometry should be drawn, where the shrinkage value could be calculated from the evaporative mass flux. Moreover, this method can also CCR and CCA modes of evaporation.

BIBLIOGRAPHY

- [1] Balaji Bakthavatchalam, Khairul Habib, R Saidur, Bidyut Baran Saha, and Kashif Irshad. Comprehensive study on nanofluid and ionanofluid for heat transfer enhancement: A review on current and future perspective. *Journal of Molecular Liquids*, 305:112787, 2020.
- [2] Muhammad Awais and Arafat A Bhuiyan. Heat transfer enhancement using different types of vortex generators (vgs): A review on experimental and numerical activities. *Thermal Science and Engineering Progress*, 5:524–545, 2018.
- [3] MS Krakov and IV Nikiforov. Influence of the shape of the inner boundary on thermomagnetic convection in the annulus between horizontal cylinders: Heat transfer enhancement. *International Journal of Thermal Sciences*, 153:106374, 2020.
- [4] Szu-Chi Huang, Chen-Chih Wang, and Yao-Hsien Liu. Heat transfer measurement in a rotating cooling channel with staggered and inline pin-fin arrays using liquid crystal and stroboscopy. *International Journal of Heat and Mass Transfer*, 115:364–376, 2017.
- [5] Mehrdad Karimzadehkhoei, Sinan Eren Yalcin, Kürşat Şendur, M Pınar Mengüç, and Ali Koşar. Pressure drop and heat transfer characteristics of nanofluids in horizontal microtubes under thermally developing flow conditions. *Experimental Thermal and Fluid Science*, 67:37–47, 2015.
- [6] José Carpio and Alvaro Valencia. Heat transfer enhancement through longitudinal vortex generators in compact heat exchangers with flat tubes. *International Communications in Heat and Mass Transfer*, 120:105035, 2021.
- [7] Mojtaba Bezaatpour and Mohammad Goharkhah. Convective heat transfer enhancement in a double pipe mini heat exchanger by magnetic field induced swirling flow. *Applied Thermal Engineering*, 167:114801, 2020.
- [8] Hasan Mousa, Jamil Naser, Ashish M Gujarathi, and Salsabeel Al-Sawafi. Experimental study and analysis of solar still desalination using phase change materials. *Journal of Energy Storage*, 26:100959, 2019.
- [9] Hongyu Wu, Dong Zhang, Biaobiao Yang, Chao Chen, Yunping Li, Kechao Zhou, Liang Jiang, and Ruiping Liu. Microstructural evolution and defect formation in a powder metallurgy nickel-based superalloy processed by selective laser melting. *Journal of Materials Science & Technology*, 36:7–17, 2020.
- [10] Margarita Monge-Morera, Marlies A Lambrecht, Lomme J Deleu, Rodrigo Gallardo, Nikolaos N Louros, Matthias De Vleeschouwer, Frederic Rousseau, Joost Schymkowitz, and Jan A Delcour. Processing induced changes in food proteins: Amyloid formation during boiling of hen egg white. *Biomacromolecules*, 21(6):2218–2228, 2020.

- [11] Yigit Akkus and Ali Beskok. Molecular diffusion replaces capillary pumping in phase-change-driven nanopumps. *Microfluidics and Nanofluidics*, 23(2):14, 2019.
- [12] Wang Yulu, Liu Fei, Yuemeng Yang, and Li-Ping Xu. Droplet evaporation induced analytes concentration toward sensitive biosensing. *Materials Chemistry Frontiers*, 2021.
- [13] Vahid Ebrahimpour Ahmadi, Akam Aboubakri, Abdolali Khalili Sadaghiani, Khellil Sefiane, and Ali Koşar. Effect of functional surfaces with gradient mixed wettability on flow boiling in a high aspect ratio microchannel. *Fluids*, 5(4):239, 2020.
- [14] Koji Enoki, Masaharu Ono, Tomio Okawa, Budi Kristiawan, and Agung Tri Wijayanta. Water flow boiling heat transfer in vertical minichannel. *Experimental thermal and fluid science*, 117:110147, 2020.
- [15] Stefano Bortolin, Andrea Francescon, Gherhardt Ribatski, and Davide Del Col. Flow boiling of r134a and hfe-7000 in a single silicon microchannel with microstructured sidewalls. *International Journal of Heat and Mass Transfer*, 179:121653, 2021.
- [16] Hadi Ahmadi Moghaddam, Alireza Sarmadian, Amirmasoud Asnaashari, Hossein Ahmadi Nejad Joushani, Mohammad Saidul Islam, Suvash C Saha, Golar Ghasemi, and Maziar Shafae. Condensation heat transfer and pressure drop characteristics of isobutane in horizontal channels with twisted tape inserts. *International Journal of Refrigeration*, 118:31–40, 2020.
- [17] Aixiang Ma, Jinjia Wei, Minzhe Yuan, and Jiabin Fang. Enhanced flow boiling heat transfer of fc-72 on micro-pin-finned surfaces. *International Journal of Heat and Mass Transfer*, 52(13-14):2925–2931, 2009.
- [18] Daniel Attinger, Christophe Frankiewicz, Amy R Betz, Thomas M Schutzius, Ranjan Ganguly, Arindam Das, Chang-Jin Kim, and Constantine M Megaridis. Surface engineering for phase change heat transfer: A review. *MRS Energy & Sustainability*, 1, 2014.
- [19] Mostafa Shojaeian and Ali Koşar. Pool boiling and flow boiling on micro-and nanostructured surfaces. *Experimental Thermal and Fluid Science*, 63:45–73, 2015.
- [20] Abdolali Khalili Sadaghiani, Nawzat S Saadi, Sorour Semsari Parapari, Tansel Karabacak, Mehmet Keskinöz, and Ali Koşar. Boiling heat transfer performance enhancement using micro and nano structured surfaces for high heat flux electronics cooling systems. *Applied Thermal Engineering*, 127:484–498, 2017.
- [21] Terry J Hendricks, Shankar Krishnan, Changho Choi, Chih-Hung Chang, and Brian Paul. Enhancement of pool-boiling heat transfer using nanostructured surfaces on aluminum and copper. *International Journal of Heat and Mass Transfer*, 53(15-16):3357–3365, 2010.

- [22] Soroush Niazi, Abdolali K Sadaghiani, Ghazaleh Gharib, Veysel Ogulcan Kaya, Süleyman Çelik, Özlem Kutlu, and Ali Koşar. Bio-coated surfaces with micro-roughness and micro-porosity: Next generation coatings for enhanced energy efficiency. *Energy*, 222:119959, 2021.
- [23] Abdolali Khalili Sadaghiani, Rana Altay, H Noh, HJ Kwak, Kürşat Şendur, B Mısırlıoğlu, HS Park, and A Koşar. Effects of bubble coalescence on pool boiling heat transfer and critical heat flux—a parametric study based on artificial cavity geometry and surface wettability. *International Journal of Heat and Mass Transfer*, 147:118952, 2020.
- [24] Nilanjana Basu, Gopinath R Warriar, and Vijay K Dhir. Onset of nucleate boiling and active nucleation site density during subcooled flow boiling. *J. Heat Transfer*, 124(4):717–728, 2002.
- [25] Abdolali Khalili Sadaghiani, Hossein Rajabnia, Süleyman Çelik, H Noh, HJ Kwak, Mona Nejatpour, Hyun Sun Park, HY Acar, B Mısırlıoğlu, MR Özdemir, et al. Pool boiling heat transfer of ferrofluids on structured hydrophilic and hydrophobic surfaces: The effect of magnetic field. *International Journal of Thermal Sciences*, 155:106420, 2020.
- [26] Ahmad Reza Motezakker, Abdolali Khalii Sadaghiani, Suleyman Celik, Tom Larsen, Luis Guillermo Villanueva, and Ali Koşar. Optimum ratio of hydrophobic to hydrophilic areas of biphilic surfaces in thermal fluid systems involving boiling. *International Journal of Heat and Mass Transfer*, 135:164–174, 2019.
- [27] Mirvahid Mohammadpour Chehrghani, Taher Abbasiasl, Abdolali Khalili Sadaghiani, and Ali Kosar. Copper-based superhydrophobic nanostructures for heat transfer in flow condensation. *ACS Applied Nano Materials*, 4(2): 1719–1732, 2021.
- [28] H Patrick Jansen, Harold JW Zandvliet, and E Stefan Kooij. Evaporation of elongated droplets on chemically stripe-patterned surfaces. *International journal of heat and mass transfer*, 82:537–544, 2015.
- [29] Chao Wang, Ruina Xu, Yu Song, and Peixue Jiang. Study on water droplet flash evaporation in vacuum spray cooling. *International Journal of Heat and Mass Transfer*, 112:279–288, 2017.
- [30] Soma Chakraborty, Marc A Rosen, and Brendan D MacDonald. Analysis and feasibility of an evaporative cooling system with diffusion-based sessile droplet evaporation for cooling microprocessors. *Applied Thermal Engineering*, 125: 104–110, 2017.
- [31] Sajag Poudel, An Zou, and Shalabh C Maroo. Droplet evaporation on porous nanochannels for high heat flux dissipation. *ACS applied materials & interfaces*, 13(1):1853–1860, 2020.
- [32] Detlef Lohse. Fundamental fluid dynamics challenges in inkjet printing. *Annual Review of Fluid Mechanics*, 54, 2022.

- [33] Karam Nashwan Al-Milaji, Ray Richard Secondo, Tse Nga Ng, Nathaniel Kinsey, and Hong Zhao. Interfacial self-assembly of colloidal nanoparticles in dual-droplet inkjet printing. *Advanced Materials Interfaces*, 5(10):1701561, 2018.
- [34] Jun Zhang, Josh Tuohey, Negin Amini, David AV Morton, and Karen P Hapgood. Liquid imbibition into 3d printed porous substrates. *Chemical Engineering Science*, 245:116967, 2021.
- [35] Vincent Dugas, Jérôme Broutin, and Eliane Souteyrand. Droplet evaporation study applied to dna chip manufacturing. *Langmuir*, 21(20):9130–9136, 2005.
- [36] David J You and Jeong-Yeol Yoon. Droplet centrifugation, droplet dna extraction, and rapid droplet thermocycling for simpler and faster pcr assay using wire-guided manipulations. *Journal of biological engineering*, 6(1):1–10, 2012.
- [37] Wenqian Feng, Erica Ueda, and Pavel A Levkin. Droplet microarrays: From surface patterning to high-throughput applications. *Advanced materials*, 30(20):1706111, 2018.
- [38] Apratim Sanyal and Saptarshi Basu. Evolution of internal flows in mechanically oscillating sessile droplets undergoing evaporation. *Chemical Engineering Science*, 163:179–188, 2017.
- [39] Mustafa A Kadhim, Nikil Kapur, Jonathan L Summers, and Harvey Thompson. Experimental and theoretical investigation of droplet evaporation on heated hydrophilic and hydrophobic surfaces. *Langmuir*, 35(19):6256–6266, 2019.
- [40] Oluwafemi Ayodele George, Jie Xiao, Carles Safont Rodrigo, Ruben Mercadé-Prieto, Julià Sempere, and Xiao Dong Chen. Detailed numerical analysis of evaporation of a micrometer water droplet suspended on a glass filament. *Chemical Engineering Science*, 165:33–47, 2017.
- [41] Eberhard Bänsch and Michael Götz. Numerical study of droplet evaporation in an acoustic levitator. *Physics of Fluids*, 30(3):037103, 2018.
- [42] RG Picknett and R Bexon. The evaporation of sessile or pendant drops in still air. *Journal of Colloid and Interface Science*, 61(2):336–350, 1977.
- [43] Daniel Orejon, Khellil Sefiane, and Martin ER Shanahan. Stick–slip of evaporating droplets: substrate hydrophobicity and nanoparticle concentration. *Langmuir*, 27(21):12834–12843, 2011.
- [44] Apratim Sanyal and Saptarshi Basu. Evaporation excites temporal sequence of resonant modes in a sessile droplet perturbed at constant frequency—insights into the universal dynamics of mode transitions. *Chemical Engineering Science*, 176:294–305, 2018.
- [45] Tuan AH Nguyen, Anh V Nguyen, Marc A Hampton, Zhi Ping Xu, Longbin Huang, and Victor Rudolph. Theoretical and experimental analysis of droplet evaporation on solid surfaces. *Chemical engineering science*, 69(1):522–529, 2012.

- [46] Dong Hwan Shin, Seong Hyuk Lee, Jung-Yeul Jung, and Jung Yul Yoo. Evaporating characteristics of sessile droplet on hydrophobic and hydrophilic surfaces. *Microelectronic Engineering*, 86(4-6):1350–1353, 2009.
- [47] Lu Liu, Xiujun Liang, Xilin Wang, Shuxian Kong, Kaiqi Zhang, and Menglong Mi. Evaporation of a sessile water droplet during depressurization. *International Journal of Thermal Sciences*, 159:106587, 2021.
- [48] Yiğit Akkuş, Hakan I Tarman, Barbaros Çetin, and Zafer Dursunkaya. Two-dimensional computational modeling of thin film evaporation. *International Journal of Thermal Sciences*, 121:237–248, 2017.
- [49] PJ Sáenz, AW Wray, Z Che, OK Matar, Prashant Valluri, Jungho Kim, and Khellil Sefiane. Dynamics and universal scaling law in geometrically-controlled sessile drop evaporation. *Nature communications*, 8(1):1–9, 2017.
- [50] Kidus Guye, Mun Mun Nahar, Quan Chau, and Damena Agonafer. Design and optimization array of micropillar structures for enhanced evaporative cooling of high-powered electronics. In *2021 37th Semiconductor Thermal Measurement, Modeling & Management Symposium (SEMI-THERM)*, pages 88–94. IEEE, 2021.
- [51] Gaurav Nath and Bahni Ray. Manipulating the three-phase contact line of an evaporating particle-laden droplet to get desirable microstructures: A lattice boltzmann study. *Physics of Fluids*, 33(8):083304, 2021.
- [52] Tuan AH Nguyen, Simon R Biggs, and Anh V Nguyen. Manipulating colloidal residue deposit from drying droplets: Air/liquid interface capture competes with coffee-ring effect. *Chemical Engineering Science*, 167:78–87, 2017.
- [53] Li Shan, Shuai Shuai, Binjian Ma, Zichen Du, Baris Dogruoz, and Damena Agonafer. Numerical investigation of shape effect on microdroplet evaporation. *Journal of Electronic Packaging*, 141(4):041008, 2019.
- [54] Li Shan, Binjian Ma, Junhui Li, Baris Dogruoz, and Damena Agonafer. Investigation of the evaporation heat transfer mechanism of a non-axisymmetric droplet confined on a heated micropillar structure. *International journal of heat and mass transfer*, 141:191–203, 2019.
- [55] Li Shan, Junhui Li, Binjian Ma, Xinyu Jiang, Baris Dogruoz, and Damena Agonafer. Experimental investigation of evaporation from asymmetric microdroplets confined on heated micropillar structures. *Experimental Thermal and Fluid Science*, 109:109889, 2019.
- [56] Ben-Xi Zhang, Shuo-Lin Wang, Yi-Bo Wang, Shu-Rong Gao, Yan-Ru Yang, and Xiao-Dong Wang. Spreading of a nanodroplet over isothermally heated smooth and nanostructured surfaces: A molecular dynamics study. *International Journal of Thermal Sciences*, 159:106649, 2021.
- [57] Xianming Dai, Fanghao Yang, Ronggui Yang, Xinyu Huang, William A Rigdon, Xiaodong Li, and Chen Li. Biphilic nanoporous surfaces enabled exceptional drag reduction and capillary evaporation enhancement. *Applied Physics Letters*, 105(19):191611, 2014.

- [58] Dorra Khilifi, Walid Foudhil, Souad Harmand, and Sadok Ben Jabrallah. Evaporation of a sessile oil drop in the wenzel-like regime. *International Journal of Thermal Sciences*, 151:106236, 2020.
- [59] Shuang Ye, Li Zhang, Chun-Mei Wu, You-Rong Li, and Qiu-Sheng Liu. Experimental investigation of evaporation dynamic of sessile droplets in pure vapor environment with low pressures. *International Journal of Thermal Sciences*, 149:106213, 2020.
- [60] Cosimo Buffone. Evaporating sessile drops subject to crosswind. *International Journal of Thermal Sciences*, 144:1–10, 2019.
- [61] Maximilian Hartmann and Steffen Hardt. Stability of evaporating droplets on chemically patterned surfaces. *Langmuir*, 35(14):4868–4875, 2019.
- [62] Jonathan B Boreyko, Georgios Polizos, Panos G Datskos, Stephen A Sarles, and C Patrick Collier. Air-stable droplet interface bilayers on oil-infused surfaces. *Proceedings of the National Academy of Sciences*, 111(21):7588–7593, 2014.
- [63] Tapan Kumar Pradhan and Pradipta Kumar Panigrahi. Influence of an adjacent droplet on fluid convection inside an evaporating droplet of binary mixture. *Colloids and Surfaces A: Physicochemical and Engineering Aspects*, 500:154–165, 2016.
- [64] Stephen Wilson, Alexander Wray, and Brian Duffy. Competitive evaporation of multiple sessile droplets. In *APS Division of Fluid Dynamics Meeting Abstracts*, pages P22–005, 2019.
- [65] Kai Leong Chong, Yanshen Li, Chong Shen Ng, Roberto Verzicco, and Detlef Lohse. Convection-dominated dissolution for single and multiple immersed sessile droplets. *Journal of fluid mechanics*, 892, 2020.
- [66] Angkur Jyoti Dipanka Shaikeea and Saptarshi Basu. Evaporating sessile droplet pair: Insights into contact line motion, flow transitions and emergence of universal vaporisation pattern. *Applied Physics Letters*, 108(24):244102, 2016.
- [67] Shilpi Chatterjee, Indradev Kumar, Kartik Chandra Ghanta, Abhiram Hens, and Gautam Biswas. Insight into molecular rearrangement of a sessile ionic nanodroplet with applied electric field. *Chemical Engineering Science*, 247:117083, 2022.
- [68] Shilpi Chatterjee, Abhiram Hens, Kartik Chandra Ghanta, and Gautam Biswas. Molecular dynamics study of sessile ionic nanodroplet under external electric field. *Chemical Engineering Science*, 229:116143, 2021.
- [69] Shaojun Dou and Liang Hao. Numerical study of droplet evaporation on heated flat and micro-pillared hydrophobic surfaces by using the lattice boltzmann method. *Chemical Engineering Science*, 229:116032, 2021.

- [70] Rodrigo Ledesma-Aguilar, Dominic Vella, and Julia M Yeomans. Lattice-boltzmann simulations of droplet evaporation. *Soft Matter*, 10(41):8267–8275, 2014.
- [71] Feargus GH Schofield, Alexander W Wray, David Pritchard, and Stephen K Wilson. The shielding effect extends the lifetimes of two-dimensional sessile droplets. *Journal of Engineering Mathematics*, 120(1):89–110, 2020.
- [72] Yigit Akkus, Barbaros Çetin, and Zafer Dursunkaya. A theoretical framework for comprehensive modeling of steadily fed evaporating droplets and the validity of common assumptions. *International Journal of Thermal Sciences*, 158:106529, 2020.
- [73] L Saraceno, GP Celata, M Furrer, A Mariani, and G Zummo. Flow boiling heat transfer of refrigerant fc-72 in microchannels. *International journal of thermal sciences*, 53:35–41, 2012.
- [74] Satish G Kandlikar. Scale effects on flow boiling heat transfer in microchannels: A fundamental perspective. *International Journal of Thermal Sciences*, 49(7):1073–1085, 2010.
- [75] Yue Ma and JN Chung. A study of bubble dynamics in reduced gravity forced-convection boiling. *International journal of heat and mass transfer*, 44(2):399–415, 2001.
- [76] CO Gersey and I Mudawar. Effects of orientation on critical heat flux from chip arrays during flow boiling. 1992.
- [77] TJ Heindel, FP Incropera, and S Ramadhyani. Liquid immersion cooling of a longitudinal array of discrete heat sources in protruding substrates: I—single-phase convection. 1992.
- [78] TJ Heindel, S Ramadhyani, and FP Incropera. Liquid immersion cooling of a longitudinal array of discrete heat sources in protruding substrates: II—forced convection boiling. 1992.
- [79] KR Samant and TW Simon. Heat transfer from a small heated region to r-113 and fc-72. 1989.
- [80] Claudi Martín-Callizo, Björn Palm, and Wahib Owhaib. Subcooled flow boiling of r-134a in vertical channels of small diameter. *International Journal of Multiphase Flow*, 33(8):822–832, 2007.
- [81] Chiwoong Choi, Jeong Seob Shin, Dong In Yu, and Moo Hwan Kim. Flow boiling behaviors in hydrophilic and hydrophobic microchannels. *Experimental Thermal and Fluid Science*, 35(5):816–824, 2011.
- [82] Jonghyun Kim and Joon Sang Lee. Numerical study on the effects of inertia and wettability on subcooled flow boiling in microchannels. *Applied Thermal Engineering*, 152:175–183, 2019.

- [83] Hai Trieu Phan, Nadia Caney, Philippe Marty, Stéphane Colasson, and Jérôme Gavillet. Flow boiling of water in a minichannel: The effects of surface wettability on two-phase pressure drop. *Applied Thermal Engineering*, 31(11-12): 1894–1905, 2011.
- [84] Qi Zhao, Juncheng Qiu, Jianhong Zhou, Mingxiang Lu, Qiang Li, and Xuemei Chen. Visualization study of flow boiling characteristics in open microchannels with different wettability. *International Journal of Heat and Mass Transfer*, 180:121808, 2021.
- [85] Kaiyu Tan, Yanwei Hu, and Yurong He. Effect of wettability on flow boiling heat transfer in a microtube. *Case Studies in Thermal Engineering*, 26:101018, 2021.
- [86] Hongzhao Wang, Yinchuang Yang, Minghao He, and Huihe Qiu. Subcooled flow boiling heat transfer in a microchannel with chemically patterned surfaces. *International Journal of Heat and Mass Transfer*, 140:587–597, 2019.
- [87] Jin Man Kim, TaeJoo Kim, Dong In Yu, Hyunwoo Noh, Moo Hwan Kim, Kiyofumi Moriyama, and Hyun Sun Park. Effect of heterogeneous wetting surface characteristics on flow boiling performance. *International Journal of Heat and Fluid Flow*, 70:141–151, 2018.
- [88] Jonghyun Kim, Jae Yong Cho, and Joon Sang Lee. Flow boiling enhancement by bubble mobility on heterogeneous wetting surface in microchannel. *International Journal of Heat and Mass Transfer*, 153:119631, 2020.
- [89] H Honda, H Takamastu, and JJ Wei. Enhanced boiling of fc-72 on silicon chips with micro-pin-fins and submicron-scale roughness. *J. Heat Transfer*, 124(2):383–390, 2002.
- [90] H Honda and JJ Wei. Enhanced boiling heat transfer from electronic components by use of surface microstructures. *Experimental Thermal and Fluid Science*, 28(2-3):159–169, 2004.
- [91] Chih-Ping Yin, Yi-Yie Yan, Tsing-Fa Lin, and Bing-Chwen Yang. Subcooled flow boiling heat transfer of r-134a and bubble characteristics in a horizontal annular duct. *International journal of heat and mass transfer*, 43(11):1885–1896, 2000.
- [92] R Maurus, V Ilchenko, and T Sattelmayer. Study of the bubble characteristics and the local void fraction in subcooled flow boiling using digital imaging and analysing techniques. *Experimental Thermal and Fluid Science*, 26(2-4):147–155, 2002.
- [93] Muzammil Iqbal, Duy Khoe Dinh, Qasim Abbas, Muhammad Imran, Harse Sattar, and Aqrab Ul Ahmad. Controlled surface wettability by plasma polymer surface modification. *Surfaces*, 2(2):349–371, 2019.
- [94] Eric J Falde, Stefan T Yohe, Yolonda L Colson, and Mark W Grinstaff. Superhydrophobic materials for biomedical applications. *Biomaterials*, 104:87–103, 2016.

- [95] Kim S Siow, Sunil Kumar, and Hans J Griesser. Low-pressure plasma methods for generating non-reactive hydrophilic and hydrogel-like bio-interface coatings—a review. *Plasma Processes and Polymers*, 12(1):8–24, 2015.
- [96] Choon-Sang Park, Eun Young Jung, Dong Ha Kim, Do Yeob Kim, Hyung-Kun Lee, Bhum Jae Shin, Dong Ho Lee, Heung-Sik Tae, et al. Atmospheric pressure plasma polymerization synthesis and characterization of polyaniline films doped with and without iodine. *Materials*, 10(11):1272, 2017.
- [97] Lin Feng, Shuhong Li, Yingshun Li, Huanjun Li, Lingjuan Zhang, Jin Zhai, Yanlin Song, Biqian Liu, Lei Jiang, and Daoben Zhu. Super-hydrophobic surfaces: from natural to artificial. *Advanced materials*, 14(24):1857–1860, 2002.
- [98] Rémi Bertossi, Nadia Caney, Jean Antoine Gruss, and Olivier Poncelet. Pool boiling enhancement using switchable polymers coating. *Applied Thermal Engineering*, 77:121–126, 2015.
- [99] Taha Çıkım, Efe Armağan, Gozde Ozaydin Ince, and Ali Koşar. Flow boiling enhancement in microtubes with crosslinked phema coatings and the effect of coating thickness. *Journal of heat transfer*, 136(8):081504, 2014.
- [100] Ahmed Elkholy and Roger Kempers. Enhancement of pool boiling heat transfer using 3d-printed polymer fixtures. *Experimental Thermal and Fluid Science*, 114:110056, 2020.
- [101] Han Zhang, Qiuping Yan, Qingyu Xu, Changshi Xiao, and Xuelei Liang. A sacrificial layer strategy for photolithography on highly hydrophobic surface and its application for electrowetting devices. *Scientific reports*, 7(1):1–7, 2017.
- [102] Lining Dong, Xiaojun Quan, and Ping Cheng. An experimental investigation of enhanced pool boiling heat transfer from surfaces with micro/nano-structures. *International Journal of Heat and Mass Transfer*, 71:189–196, 2014.
- [103] Hugh W Coleman and W Glenn Steele. *Experimentation, validation, and uncertainty analysis for engineers*. John Wiley & Sons, 2018.
- [104] Ramesh K Shah and Alexander Louis London. *Laminar flow forced convection in ducts: a source book for compact heat exchanger analytical data*. Academic press, 2014.
- [105] Manuel Janocha and Evangelos Tsotsas. In silico investigation of the evaporation flux distribution along sessile droplet surfaces during convective drying. *Chemical Engineering Science*, 238:116590, 2021.
- [106] RT van Gaalen, C Diddens, HMA Wijshoff, and JGM Kuerten. Marangoni circulation in evaporating droplets in the presence of soluble surfactants. *Journal of colloid and interface science*, 584:622–633, 2021.
- [107] Md Almostasim Mahmud and Brendan D MacDonald. Experimental investigation of interfacial energy transport in an evaporating sessile droplet for evaporative cooling applications. *Physical Review E*, 95(1):012609, 2017.

- [108] Ray E Bolz and George L Tuve. *CRC handbook of tables for applied engineering science*. CRC press, 2019.
- [109] PJ Robinson and JA Davies. Laboratory determinations of water surface emissivity. *Journal of Applied Meteorology*, 11(8):1391–1393, 1972.
- [110] Hua Hu and Ronald G Larson. Analysis of the effects of marangoni stresses on the microflow in an evaporating sessile droplet. *Langmuir*, 21(9):3972–3980, 2005.
- [111] Zhenhai Pan, Susmita Dash, Justin A Weibel, and Suresh V Garimella. Assessment of water droplet evaporation mechanisms on hydrophobic and superhydrophobic substrates. *Langmuir*, 29(51):15831–15841, 2013.
- [112] Ha V Tran, Tuan AH Nguyen, Simon R Biggs, and Anh V Nguyen. On the predictions for diffusion-driven evaporation of sessile droplets with interface cooling. *Chemical Engineering Science*, 177:417–421, 2018.
- [113] Meysam R Barmi and Carl D Meinhart. Convective flows in evaporating sessile droplets. *The Journal of Physical Chemistry B*, 118(9):2414–2421, 2014.
- [114] Kwan Hyoungh Kang, Hee Chang Lim, Hee Woong Lee, and Sang Joon Lee. Evaporation-induced saline rayleigh convection inside a colloidal droplet. *Physics of Fluids*, 25(4):042001, 2013.
- [115] Anna-Lena Ljung and T Staffan Lundström. Heat and mass transfer boundary conditions at the surface of a heated sessile droplet. *Heat and Mass Transfer*, 53(12):3581–3591, 2017.
- [116] Deepak Kumar Mandal and Shamit Bakshi. Internal circulation in a single droplet evaporating in a closed chamber. *International journal of multiphase flow*, 42:42–51, 2012.
- [117] Vivek Jaiswal, AR Harikrishnan, Gargi Khurana, and Purbarun Dhar. Ionic solubility and solutal advection governed augmented evaporation kinetics of salt solution pendant droplets. *Physics of Fluids*, 30(1):012113, 2018.
- [118] Yiğit Akkuş, Barbaros Çetin, and Zafer Dursunkaya. Modeling of evaporation from a sessile constant shape droplet. In *International Conference on Nanochannels, Microchannels, and Minichannels*, volume 58301, page V001T04A004. American Society of Mechanical Engineers, 2017.
- [119] Shyamashis Das, Atreya Dey, Govardhan Reddy, and DD Sarma. Suppression of the coffee-ring effect and evaporation-driven disorder to order transition in colloidal droplets. *The journal of physical chemistry letters*, 8(19):4704–4709, 2017.
- [120] Nagesh D Patil, Prathamesh G Bange, Rajneesh Bhardwaj, and Atul Sharma. Effects of substrate heating and wettability on evaporation dynamics and deposition patterns for a sessile water droplet containing colloidal particles. *Langmuir*, 32(45):11958–11972, 2016.

- [121] Jonghyeok Park, Junil Ryu, Hyung Jin Sung, and Hyoungsoo Kim. Control of solutal marangoni-driven vortical flows and enhancement of mixing efficiency. *Journal of colloid and interface science*, 561:408–415, 2020.
- [122] Kai Yang, Fangjun Hong, and Ping Cheng. A fully coupled numerical simulation of sessile droplet evaporation using arbitrary lagrangian–eulerian formulation. *International Journal of Heat and Mass Transfer*, 70:409–420, 2014.
- [123] Gianluca Laghezza, Erik Dietrich, Julia M Yeomans, Rodrigo Ledesma-Aguilar, E Stefan Kooij, Harold JW Zandvliet, and Detlef Lohse. Collective and convective effects compete in patterns of dissolving surface droplets. *Soft matter*, 12(26):5787–5796, 2016.
- [124] Yağmur Şişman, Abdolali Khalili Sadaghiani, Khedir R Khedir, Matthew Brozak, Tansel Karabacak, and Ali Koşar. Subcooled flow boiling over microstructured plates in rectangular minichannels. *Nanoscale and Microscale Thermophysical Engineering*, 20(3-4):173–190, 2016.
- [125] YM Lie, JH Ke, WR Chang, TC Cheng, and TF Lin. Saturated flow boiling heat transfer and associated bubble characteristics of fc-72 on a heated micro-pin-finned silicon chip. *International Journal of Heat and Mass Transfer*, 50(19-20):3862–3876, 2007.